THE UNIVERSITY OF
WARWICK

AUTHOR: **Paul A. O'Brien** DEGREE: **Ph.D.**

TITLE: **Simulation and Theory of Liquid Crystals**

DATE OF DEPOSIT: .....

I agree that this thesis shall be available in accordance with the regulations governing the University of Warwick theses.

I agree that the summary of this thesis may be submitted for publication.

I **agree** that the thesis may be photocopied (single copies for study purposes only).

Theses with no restriction on photocopying will also be made available to the British Library for microfilming. The British Library may supply copies to individuals or libraries. subject to a statement from them that the copy is supplied for non-publishing purposes. All copies supplied by the British Library will carry the following statement:

> "Attention is drawn to the fact that the copyright of this thesis rests with its author. This copy of the thesis has been supplied on the condition that anyone who consults it is understood to recognise that its copyright rests with its author and that no quotation from the thesis and no information derived from it may be published without the author's written consent."

AUTHOR'S SIGNATURE: .....

USER'S DECLARATION

1. I undertake not to quote or make use of any information from this thesis without making acknowledgement to the author.
2. I further undertake to allow no-one else to use this thesis while it is in my care.

DATE SIGNATURE ADDRESS

.....

.....

.....

.....

.....

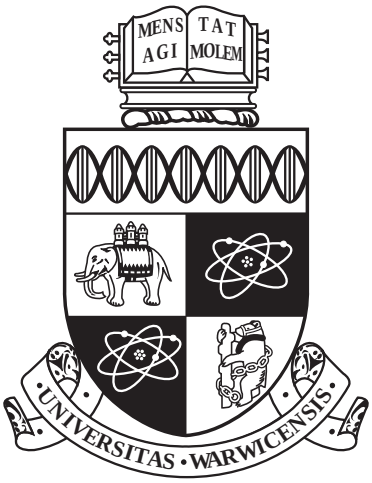

Simulation and Theory of Liquid Crystals

by

Paul A. O'Brien

Thesis

Submitted to the University of Warwick

for the degree of

Doctor of Philosophy

Department of Physics

March 2010

THE UNIVERSITY OF
WARWICK

Contents

Acknowledgments

I would like to thank my academic supervisor, Professor Michael P. Allen, for all of his teaching, effort, insight and understanding during the course of this project. I would also like to thank Dr. David L. Cheung for standing in to supervise some aspects of the project while Mike was on sabbatical during the first year.

Computational resources were provided by the Centre for Scientific Computing, University of Warwick. I would like to thank all of the members and visitors of the Department of Physics and the Centre for Scientific Computing for technical support, advice and social interaction. A number of fellow academics encountered at conferences were also useful and deserve credit, particularly our collaborators, who provided their results to be contained in this very thesis. Funding was provided by the Engineering and Physical Sciences Research Council. All molecular graphics were produced using the QMGA package [Gabriel et al., 2008]. On a more personal note, I would like thank all of my family, friends and housemates for their help, support, entertainment and cohabitation.

Declarations

I declare that no part of this thesis has been submitted for a higher degree in this, or any other, university. The research reported herein is the result of my own investigation except where reference is made to the work of others. All research was carried out under the supervision of Professor M. P. Allen at the University of Warwick, between October 2005 and March 2010.

– Paul Andrew O'Brien, March 2010

Once you have eliminated the impossible, whatever remains, however improbable, must be the truth.

– Lieutenant Commander Data, USS Enterprise (2367)

Abstract

We present a study of the theory and simulation of Liquid Crystals. A general introduction to the field is given, then the essential features of the Monte Carlo (MC) sampling algorithm are described and explained, along with some of the practical considerations in the implementation of MC. Several quantitative measures used to describe liquid crystalline systems are outlined, including the second rank order tensor, in addition to some of those from elastic theory and density functional theory. Monte Carlo Simulations were performed in bulk geometry in the canonical ensemble in order to calculate the Frank elastic constants of hard spherocylinders, hard platelets and hard cut-spheres at three thicknesses. Onsager's density functional theory was also performed to yield the elastic constants for hard platelets, and this amounts to using a virial expansion in the free energy, truncated at second order. Our collaborators for O'Brien et al. [2008] provided results for the elastic constants from a calculation of the higher order virial coefficients. All of the results from theory are compared to simulation, with some experimental determinations available. All three elastic constants compared well with the high-order virial theory, there is quantitative agreement with the experimental values, and the effect of increasing thickness of discs was found to improve the agreement of the ratio of K_1/K_3. Aspects of translationally ordered phases are studied in the context of constrained non-equilibrium systems. Monte Carlo was also performed for platelets confined in wedge geometry, with several choices for the types of wall. A local approximation is utilised to yield the depletion force and potential as a function of the wall separation,

as well as the adsorption between the walls. The adsorption for large separations exhibited general qualitative agreement with theory and Gibbs Ensemble simulations. The two different wall boundary conditions produced different orientational structural features, with repulsive and attractive depletion potentials measured, and a planar surface phase that does not appear in the bulk is categorised.

Chapter 1

Introduction

The study of liquid crystals is a well established field of interdisciplinary research, drawing together the work of academics and industrialists in Mathematics to Chemical Engineering. They are widely studied due to the complicated behaviour observed for various systems of liquid crystals, and the field was given much publicity in the 1960s following applications devised in the optical industries, particularly for display [Vicari, 2003], and at present there are a significant number of non-visual applications [Collings, 2002; Cheung et al., 2008]. But what is a liquid crystal?

The three phases of matter; solid, liquid and gas; only give a general classification of the state in which systems of particles behave under particular conditions. The transition between solid and liquid, for example, is not so abrupt for many systems of large, complex molecules, and takes place gradually via transitions between new phases. The crystalline solid is specified by long-range translational and orientational order, with liquids exhibiting only short-range order, allowing the consituent particles to flow [Chandrasekhar, 1992]. Hence the name for these intermediate phases; states that are categorised as possessing some degree of order between that of the liquid and the crystal.

Liquid crystalline phases tend to exhibit long-range orientational order, with many of the phases also possessing some degree of long-range translational order. The extent of this ordering can be illustrated by examining the latent heat of the transitions from solid to liquid states, which tend to be orders of magnitude larger than those for transitions from the liquid crystalline phases to the isotropic liquid [Collings and Hird, 1997]. This illustrates that the vast majority of the order of a crystalline solid is lost upon transition to a liquid crystal. The phase behaviour, in

addition to other material properties, of a liquid crystalline system depends upon the details on the microscopic particles that make up the system.

The ability of such systems to assume macroscopic characteristics due to specific microscopic particle traits prompts the particles to be known as mesogens. Liquid crystalline mesogens tend to be highly anisotropic, a trait that allows systems of such particles to adopt one or more preferred directions of alignment, termed *directors*, and thus exhibit orientational order. This ordering in turn leads to anisotropy in the macroscopic properties of the material, with an example being the dependence of the refractive index within a liquid crystal on the direction of propagation of incident light [Hamley, 2000]. The extent of the orientational order can vary dramatically, and a number of order parameters have been defined to provide a quantitative measure. These order parameters may influence a number of properties that can be measured experimentally, such as optical birefringence, light scattering, diamagnetism and magnetic resonance [de Gennes and Prost, 1995].

Of the mesogens that form liquid crystalline phases, many are rod-like (calamitic) or disc-like (discotic) molecules, and are usually fairly rigid so as to maintain preferential alignment. As densities become large enough to force particles to interact closely, an interesting trade-off is the reduction in orientational freedom (increase in orientational order) in order to maximise the positional mobility, hence increasing entropy overall. Calamitic and discotic liquid crystalline phases tend to be stable for certain temperature ranges, and are referred to as thermotropic liquid crystals. Other mesogens can form liquid crystals when mixed with certain solvents, with the concentration of the solvent sometimes influence the stability of such phases more than the temperature, and these are termed lyotropic liquid crystals. These mesogens tend to be amphiphilic, forming ordered structures via segregation of hydrophobic and hydrophilic groups on the molecules. Certain polymers can also form liquid crystals, within temperature ranges, and are often composed of rigid structural units separated by flexible hydrocarbon chains [Collings, 2002].

The applications of liquid crystals amount to manipulating the phase exhibited by a liquid crystalline system by adjustment of external fields and boundaries, state variables (temperature, pressure etc.) or composition. The phase of the system will determine material properties, and the surrounding component geometry may be constructed so as to exploit the anisotropy of these properties. Some chiral phases are able to reflect light with a wavelength dependent on the helical pitch, which can be highly sensitive to temperature, providing a basic temperature sensor.

Some twisted nematics are able to rotate the polarisation of incident light, and may be placed in between two plates with perpendicular polarisation. The polarisation angle of incident light will change as it travels through the liquid crystal, and, under the right conditions, will be observed once passing through the other plate. Should the particles exhibit positive dielectric anisotropy, an electric field applied will cause the director profile to homogeneously align toward the field direction, removing the rotation of light polarisation, thus causing the device to appear dark. This is the basis of many liquid crystal display cells. There are numerous other applications outlined in the literature, including spatial light modulators and various optical switches [Collings and Hird, 1997; Hamley, 2000].

Having observed complex behaviour for liquid crystals experimentally, advances in understanding of the fundamental underlying physical principles must be judged by the accuracy of experimentally-measurable properties that they predict. Various theories exist for the treatment of liquid crystalline systems [Cleaver and Allen, 1991]. Much theory is based on the macroscopic thermodynamics and microscopic statistical mechanics of the system, using the virial expansion truncated usually at the second-order term. Simulations specify microscopic characteristics (interactions between particles) and use this to produce representations of systems from which macroscopic properties can be measured.

The computer as a tool not only allows simulations to be run (allowing a gap between theory and simulation to be bridged), but allows theory to be used beyond the constraints of analytical evaluation. Not only have more elaborate numerical methods been used to allow theorists to apply the principles to more complicated systems, but the Monte Carlo (MC) simulation algorithm using importance sampling allows observables to be estimated from the multi-dimensional integrals required for systems of particles in which all of the interactions are significant. Continuing improvements in the elegance of Molecular Dynamics techniques have allowed the increase in computer power to be fully utilised [Deuflhard et al., 1998], and dynamical properties can even be extracted from Kinetic Monte Carlo.

Under certain external conditions, systems of liquid crystals can exibit long-range order to minimise their free energy, depending upon the parameters used (pressure, temperature etc). When different degrees of order are present, macroscopic behaviour classified by experiment can be observed to be considerably different, denoting the existence of the various phases of liquid crystals.

The phases of liquid crystals exist somewhere between the states of the crys-

talline solid and the isotropic liquid. These states tend to exhibit orientational ordering, observable from experiment mainly using optical processes, and phases in which the order is purely orientational are known as nematic. Positional order can also be present to varying extents, with systems exhibiting more subtle extents being known as smectic (as well as columnar phases for systems of discs) [de Gennes and Prost, 1995], and systems that are completely ordered are considered to have entered the solid phase.

The transitions between these phases can have a number of features, with multiple coexistence regions, regions of stability in phase diagrams showing system dependence on all of external variables [Smit, 1990]. In theory and simulation, systems can enter coexistence and exhibit considerable hysteresis, providing information on energy landscapes, and there are numerous techniques for free energy calculations in general [Clark et al., 1997].

It is not possible for all types of mesogen to form each of the phases. Only systems of achiral molecules, or mixtures of equal concentration of chiral pairs [Chandrasekhar, 1992], can form the nematic phase. Also, any particle geometry that has a degree of symmetry approaching that of a sphere cannot form a smectic phase. Hence the symmetry of the molecule can determine the phase behaviour for a system of such particles. Just a small amount of perturbation in the existing molecular models can predict new phases, an example being a slight bend in hard rod models, amounting to the "banana"-shaped molecule, giving rise to the nine "B-Phases". Many asymmetric mesogens exhibit more symmetrical phases, and bent-core molecules are an example of an achiral mesogen that forms chiral phases [Luckhurst and Romano, 1997]. It is, however, believed that many of the phase restrictions present for purely hard-core particles may become lucid with the addition of other types of interaction [Martín del Río and de Miguel, 2005], thus employing such models could yield more extensive phase behaviour.

The liquid crystalline nematic phase, characterized by long-range orientational order and translational disorder of the molecules, is typically found in systems of rod-like and plate-like molecules [de Gennes and Prost, 1995]. Indeed, since the theoretical work of Onsager [Onsager, 1949] and the simulations of Frenkel and co-workers [Frenkel and Eppenga, 1982; Eppenga and Frenkel, 1984; Frenkel et al., 1984; Frenkel and Mulder, 1985] it has been known that entropic effects alone, which result from the excluded volumes of sufficiently aspherical particles, are sufficient to drive the isotropic-nematic transition. Therefore, hard-particle models capture some

of the essential physics, and have been used extensively in computer simulations. The results of such simulations may be compared, quantitatively, with experimental studies of colloidal suspensions of rod-like and plate-like solid particles [Fraden, 1995; Bates and Frenkel, 1999; van der Kooij et al., 2001].

Within the nematic phase, molecular orientations are distributed about a preferred direction: the so-called *director* $\boldsymbol{n}$. Spatial deformations of the director are well-described, in the limit of large wavelength, by the Oseen-Frank [Oseen, 1933; Frank, 1958] orientational elastic theory, which contains three phenomenological parameters, the Frank elastic constants. Experimentally, knowledge of these constants, together with a few other parameters (such as surface anchoring strengths), is sufficient to describe many of the interesting large-scale and meso-scale structures formed in liquid crystals.

For rod-like particles, computer simulations were used long ago to relate Frank elastic constants to molecular shape [Allen and Frenkel, 1988, 1990; Tjipto-Margo et al., 1992; Allen et al., 1996]. Onsager's theory, which amounts to a classical density-functional description of the distortion free energy at the second virial coefficient level (neglecting higher-than-pairwise interactions) gives an accurate description of both the thermodynamics and orientational elastic properties of sufficiently elongated rods [Evans and Smith, 1991], and can be empirically modified to give reasonable accuracy at moderate elongations [Tjipto-Margo and Evans, 1990; Tjipto-Margo et al., 1992; Camp et al., 1996]. The reason for this is well understood: the higher virial coefficients are known to vanish as the molecular elongation tends to infinity [Frenkel, 1987, 1988]. Calculations of elastic constants from Molecular Dynamics simulation have also been performed for Gay-Berne discs [Stelzer et al., 1997], and recent experiments examining the effects of external fields and interfaces on the nematic phase of plate-like colloids [van der Beek et al., 2006b, 2008] also shed light on the values of the Frank constants, and invite comparison with computer simulations and theory. However, for oblate molecules (even infinitesimally thin plates), it is known that the higher virial coefficients do not vanish, and Onsager theory gives a poor description of the phase behaviour [Frenkel and Eppenga, 1982; Eppenga and Frenkel, 1984].

In addition to the bulk, the virial coefficients can be used to describe inhomogeneous systems, and considerable improvements on elastic theory have been made, due to elastic theory being valid for director gradients that vary slowly many over particle lengths [Allen, 2000b]. However, even the higher virials have been known

to diverge for several mesogens, and computer simulation can capture more of the behaviour. Simulation studies have been performed for many of the mesogens in various geometries, with a pair of hard parallel walls providing a starting point for each. Surfaces can induce phases in mesogens that are not exhibited in bulk, and in fact it has been measured that any spacially varying director pattern may be a source of biaxiality [Biscari et al., 2006]. One difficulty in studying liquid crystalline systems is the range of behaviour over intervals in the state variables (pressure, chemical potential etc.). However, there are many examples of studies in which a large system has been taken, with a slowly varying quantity over molecular length scales in one dimension, such as chemical potential, and the properties of local regions have been close to the corresponding bulk values. These local approximations have been proved satisfactory in studies of the sedimentation equilibrium, with a range of phase-behaviour observed in the same simulation[Biben et al., 1993]. Using the local approximations to yield a single system with a range of sub-regions that can be related to other single systems saves considerable effort in constructing the simulation study, and allows a continuous range in the state variable to be studied.

We have been interested in having a range of wall separations in a single system, and the "wedge" geometry, a thin triangular slit, is ideal due to roughly parallel walls that can contain a fluid. One may perform a single simulation and simply inspect up the wedge to find quantities of interest as a function of wall separation [Gotzelmann et al., 1998]. Multiple phases have been observed experimentally together in small wedge-shaped slits, prompting simulation studies. Depletion forces are such a wall-induced interaction and have been well-studied [Mao et al., 1995; Biben et al., 1996; Gotzelmann et al., 1998; Cheung and Allen, 2006]. These arise when large surfaces are found in vicinity of one another in a suspension of smaller molecules (depletants), with the exclusion of the depletants causing them to move into or out of the regions between the surfaces. Depletion forces are entropy-driven, and have been measured to be attractive, repulsive and a combination of both [Roth et al., 1999]. A number of assumptions have been tested using depletion forces, e.g. the Derjaguin approximation [Henderson, 2002a].

Following the experiments of van der Beek et al. [2008]; Verhoeff et al. [2009], there has been interest in the elastic constants of disc-like particles, with something of a gap in the literature relating to simulation studies and results from any theory that generally describes discs well [Reich and Schmidt, 2007]. There have been other experiments performed for hard discs in bulk [van der Beek et al., 2006a] and more

confined geometries [van der Beek et al., 2006b], as well as when mixed with hard spheres [Piech and Walz, 2000]. Only a few simulators have examined discs in confined geometry [Bellier-Castella et al., 2004; Piñeiro et al., 2007; Reich et al., 2007], see section 5.1) for details. Some studies have applied the Fundamental Measure density functional theory (FMT) to platelets [Harnau and Dietrich, 2002; Reich and Schmidt, 2007], which give a drastic improvement over a second order virial expansion. The results from all of these studies (experiment, theory, and simulation of slightly different discs) invite comparison and extension with simulation of bulk and confined platelets and cut-spheres.

Our main aim is to contribute to filling the aforementioned gaps in the literature relating to disc-like particles. We aim to calculate the orientational elastic constants of hard platelets and cutspheres of three thicknesses, as well as one elongation of spherocylinders, in the nematic phase from Monte Carlo simulation and Onsager theory. We aim to check the phases present in each simulation, and appreciate some properties of the translationally ordered phases in the context of a system with fixed both lengths and constrained director. We seek quantitative agreement with theory [O'Brien et al., 2008] and experiment van der Beek et al. [2008]; Verhoeff et al. [2009]. We aim to use confined geometry to investigate the depletion force due to platelets in between flat, hard walls. We aim to utilise the local approximation, validating the approximation of the wedge geometry as a set of systems with a range of separations. We aim to calculate the adsorbed particle density between the walls, investigate the effects of different wall boundary conditions, and to categorise any observed surface phases in terms of the orientational order.

This thesis presents Monte Carlo calculations of the Frank elastic constants for systems composed of a number of hard mesogens over their full nematic range. These different mesogens are spherocylinders, thin platelets and cut-spheres of varying thickness. The results for platelets are compared with theoretical estimates which incorporate virial terms up to sixth order, as presented in O'Brien et al. [2008]. We have also performed MC simulations on hard platelets in wedge geometry, observing wall-induced planar phases as well as the isotropic and nematic found in the bulk. Profiles of the depletion forces and adsorption between the walls against the wall separation were also calculated. The thesis is arranged as follows. Chapter 2 outlines the Monte Carlo importance sampling method, and explains some of the practical considerations of application to molecular simulation. Chapter 3 gives details of determining and analysing some of the key quantities used to describe liquid

crystals in bulk and confined systems, including the order tensor, the Oseen-Frank elastic theory and the virial expansion. Chapter 4 gives the simulation details and the results of the simulations in bulk, with our Onsager second-order virial expansion results for platelets, along with as those of our collaborators for the higher virials. Chapter 5 gives details of the simulations performed in wedge geometry, for the different choices of boundary conditions, along with the results. The results for the individual topics are discussed initially in the results sections, then all of the results are discussed together and a general evaluation is found in chapter 6.

Chapter 2

The Monte Carlo Method

The Monte Carlo Method as applies to molecular simulation has been well described in the literature, and hence a concise account will be provided here.

In statistical mechanics, when investigating the properties exhibited by a themodynamic system, it is common to examine observables that may characterise the behaviour of the system. Observables may depend on any aspect of the system, and in molecular modelling are typically functions of the conformations, $\{\boldsymbol{r}_i\}^N$, and momenta, $\{\boldsymbol{p}_i\}^N$, of the N constituent partlicles that make up the system. The procedure of calculating an ensemble average of such an observable, $\mathcal{A}\left(\{\boldsymbol{r}_i, \boldsymbol{p}_i\}^N\right)$, in a system reduces to [Binder, 1979]

$$\langle \mathcal{A} \rangle = \frac{\int_{\mathcal{S}} \mathcal{A}\left(\{\boldsymbol{r}_i, \boldsymbol{p}_i\}^N\right) \exp\left(-\beta \mathcal{H}\left(\{\boldsymbol{r}_i, \boldsymbol{p}_i\}^N\right)\right) \mathrm{d}\{\boldsymbol{r}_i\}^N \mathrm{d}\{\boldsymbol{p}_i\}^N}{\int_{\mathcal{S}} \exp\left(-\beta \mathcal{H}\left(\{\boldsymbol{r}_i, \boldsymbol{p}_i\}^N\right)\right) \mathrm{d}\{\boldsymbol{r}_i\}^N \mathrm{d}\{\boldsymbol{p}_i\}^N} \tag{2.1}$$

where the integration is performed over all possible conformations and momenta (or states) of the system, $\mathcal{S}$, and $\mathcal{H}$ is the Hamiltonian of the system, giving the total energy at each state. The energy term appears in the Boltzmann factor, and acts as a weight to the integrals, ensuring that most of the contribution to the integral comes from energetically feasible states, not too far from equilibrium.

Many of the observables typically studied are static properties, depending on only the conformations, $\{\boldsymbol{r}_i\}^N$. For such quantities, the kinetic parts of the integrals in eqn (2.1) may be performed and will cancel out, leaving us with a quantity that may be found from consideration of the static system configurations alone, with the Bolzmann factor containing simply the potential, $\mathcal{E}$, for each state.

However, even after such a simplification, attempting to evaluate such an

integral can be problematic at best, mostly due to the dimensionality of the integration variables. Using a numerical quadrature that samples over regions of $\mathcal{S}$, even for small systems and a small number of evaluation points, can still involve an inpractical number of computations, of the order L^{DN}, where L is the number of different values each coordinate takes for the evaluation and D is the dimensionality of the coordinate system. For example, performing the integral for a system of $N = 100$ atoms in three dimensions over a lattice with ten points in each coordinate will involve 10^{300} computations. The "brute force" method of Monte Carlo integration merely selects states within $\mathcal{S}$ at random, and thus encounters similar problems. Another irritating consequence of using standard numerical techniques to evaluate the integrals is that the vast majority of these computations will be performed for states of the system that take unphysically high energies, at which the Boltzmann factor is vanishingly small, and thus will not even provide a significant contribution to the integral. This is before even mentioning the fact that the accuracy of numerical integrals depends on the smoothness of the integrand, and the Boltzmann factor will be be anything but smooth as the system is varied between states with drastically different energies [Frenkel and Smit, 1996].

Given these drawbacks encountered by standard numerical integration, the concept of importance sampling was first applied to this problem in the work of Metropolis et al. [1953]. The idea is that we can find the significant contributions to these integrals by simply performing the calculation for each state, i, in $\mathcal{S}$ randomly according to some probability distribution, p_i. This leads eqn (2.1) to reduce to;

$$\langle \mathcal{A} \rangle = \frac{\sum_{i \epsilon \mathcal{S}_c} \mathcal{A}_i / p_i \exp\left(-\beta \mathcal{E}_i\right)}{\sum_{i \epsilon \mathcal{S}_c} 1 / p_i \exp\left(-\beta \mathcal{E}_i\right)} \tag{2.2}$$

where $\mathcal{S}_c$ is the subset of $\mathcal{S}$ containing all of our sample states, i. p_i should be chosen such that the integrand will have suitably non-zero values, thus providing a significant contribution to the integral. There may be arbitrarily optimal ways of ensuring this, depending on the potential distribution of the system and the observable of choice, i.e. both $\mathcal{A}_i \exp\left(-\beta \mathcal{E}_i\right)$ and $\exp\left(-\beta \mathcal{E}_i\right)$ should be large for a significant number of the states sampled. However, the general method used by the authors is now a standard choice, which is to choose states with a probability distribution that is proportional to the Boltzmann factor, $\exp\left(-\beta \mathcal{E}_i\right)$. This choice reduces eqn (2.2) to an arithmetic mean of the value of the observable at the sample

points, i.e.

$$\langle \mathcal{A} \rangle = \frac{1}{I} \sum_{i \epsilon \mathcal{S}_c} \mathcal{A}_i \tag{2.3}$$

where I is the number of states of the system that were sampled. This method cannot be used to perform the multi-dimensional integrals and sums for the system, required for finding quantities such as the partition function, but these ensemble averages, involving a ratio of the integrals, are easily calculable once we sample states of the system according to the Boltzmann distribution.

Unfortunately, sampling states according to the Boltzmann distribution may not be as straightforward as it sounds, as for any system that is reasonably complicated, we will not know what the distribution $\exp(-\beta \mathcal{E}_i)$ is. Therefore, a method is required to sample the states with a probability distribution that converges to the Boltzmann factor in the limit of a large number of samples.

There are a number of ways of doing this, and a method justifying the choices of Metropolis et al. [1953] will be described here. The procedure needs to describe stochastically transitioning between states, whilst the probability of occupying state i, equal to p_i, is a stationary distribution, i.e. the change from one state to another is performed with a set procedure, and the distribution of states generated is always the same in the limit of many samples. The path through state space will take the form of a Markov Chain, for which the the probability of the system changing to a particular state is dependent on only the current state of the system, thus is independent of the previous states sampled[Hastings, 1970].

Let us define a transition matrix, $\pi_{i \to j}$, which gives the probability of the system changing from the state i into the state j. We do not know the density of states, p_i, so we will begin this treatment with some arbitrary starting distribution, $p_i^{(0)}$ We can then begin the generation of a Markov chain of states by performing changes in the density of states via

$$p_i^{(1)} = \sum_j \pi_{i \to j} p_j^{(0)} \tag{2.4a}$$

$$\text{or } \underline{p}^{(1)} = \underline{\underline{\pi}} \cdot \underline{p}^{(0)} \tag{2.4b}$$

where $p_i^{(t)}$ denotes the density distribution after t steps. According to Feller's theorem, subject to certain conditions, taking the limit as $t \to \infty$ will cause the distribution to converge to some limiting stationary distribution of states [Feller, 1957].

This will be equal to the equilibrium density of states, and will depend on our choice of the $\pi_{i\to j}$. This leaves us with the equation

$$\underline{p} = \underline{\underline{\pi}} \cdot \underline{p} \tag{2.5}$$

i.e. an eigenvector equation with eigenvalue 1. The flux of probablility going from i to j is $\pi_{i\to j}p_i$, and the flux from j to i is $\pi_{j\to i}p_j$. For our stationary distribution of states, summing either over j will yield the same result: the probability of finding the system in the state i.

$$\sum_j \pi_{i\to j}p_i = \sum_j \pi_{j\to i}p_j \tag{2.6}$$

i.e. the total density of states departing from i is equal to the density of states arriving at i. The condition expressed in eqn (2.6) is known as "macroscopic reversibility" or "balance", and is sufficient to ensure a static distribution of states [Hammersley and Handscomb, 1964]. A stronger condition often applied is known as "microscopic reversibility" or "detailed balance", and states that

$$\pi_{i\to j}p_i = \pi_{j\to i}p_j \tag{2.7}$$

i.e. the flux from i to j is equal to the flux from j to i. Provided that the transition matrix $\pi_{i\to j}$ and its conjugate limiting distribution satisfy balance, then a self-consistent sampling scheme is obtained. We now need to devise a choice of $\pi_{i\to j}$ that is conjugate to a p_j proportional to the Boltzmann distribution, then a valid Monte Carlo sampling scheme will have been be obtained.

One such way to find the transition matrix with this property is to begin from the condition for detailed balance, eqn (2.7), and rearrange to find that any choice for which the ratio $\pi_{i\to j}/\pi_{j\to i}$ is equal to p_i/p_j will be suitable [Valleau and Whittington, 1977]. The choice of Metropolis et al. [1953] is given by

$$\begin{aligned}
\pi_{i\to j} &= \alpha_{i\to j} \quad \text{if } p_j \geq p_i \\
\pi_{i\to j} &= \alpha_{i\to j}\frac{p_j}{p_i} \quad \text{if } p_j < p_i \\
\pi_{i\to j} &= 1 - \sum_{j\neq i} \pi_{i\to j}
\end{aligned} \tag{2.8}$$

where α is an underlying matrix dictating the probability of attempting a particular transition between states, and the other factors give the probability of accepting

the change, $r_{i\to j}$. α is symmetric, hence $\alpha_{i\to j} = \alpha_{j\to i}$, and must be chosen to attempt forward and reverse moves with equal probability. The acceptance ratio, $r_{i\to j} = \pi_{i\to j}/\alpha_{i\to j}$, is thus given by

$$\begin{aligned} r_{i\to j} &= \min\left[1, p_j/p_i\right] \\ &= \min\left[1, \exp\bigl(-\beta(\mathcal{E}_j - \mathcal{E}_i)\bigr)\right] \ . \end{aligned} \tag{2.9}$$

Defined in this manner, the general procedure for the Metropolis prescription in deciding to accept or reject a transition, from state i to j with change in energy $\delta\mathcal{E} = \mathcal{E}_j - \mathcal{E}_i$, is as follows. If $\delta\mathcal{E} \leq 0$ the move is "downhill" with respect to the free energy of the system and should be accepted unconditionally. If $\delta\mathcal{E} > 0$ the move is "uphill", and should only be accepted with probability $\exp(-\beta\delta\mathcal{E})$. The most straightforward way to do this would be to randomly generate a number between 0 and 1, and accept the move if the Boltzmann factor is greater than this number, rejecting it otherwise [Perram et al., 1984].

There is a great deal of freedom for the way in which we choose our move attempts, $\alpha_{i\to j}$. In molecular simulation, we may wish to sample the system at different configurations of the positions and orientations of the molecules. To select another state for the system to attempt a transition, each molecule in turn can be considered, and a random vector generated to change their position and orientation. The energy of the new configuration can then be calculated and inserted in (eqn 2.9), and the transition is accepted with probability $r_{i\to j}$. Attempting a single transition of the system from state i to j is often termed one MC "sweep", and the failure of the transition to be accepted means that the value of the observable for the state i would contribute more than once to the average in eqn (2.3). For a system specified by N particles, one MC sweep would ordinarily consist of one attempted move in each of the particle coordinates, i.e. N attempted moves per sweep [Yao et al., 1982].

It is also worth noting which of the balance conditions are obeyed by a MC move algorithm. For a set of N molecules, one MC sweep may be performed by assigning an order to the molecules, and then attempting a move for each particle in turn. This does obey the balance condition, but not detailed balance, as a particular molecule may not be able to assume its conformation that it left during the previous sweep without overlapping with a molecule that had moved to encroach upon it later in the sweep. In order to obey detailed balance, molecules may be selected at random

and then a move attempt performed, with N such move attempts constituting a MC sweep [Allen and Tildesley, 1987].

For our simulations of platelets, cut-spheres and cylinders, we attempted one move per particle in a particular order each MC sweep. We would choose a new position to attempt a move by randomly generating a position within a cube centred at the old position. The size of the cube will determine how often such moves are accepted, and the side length of the cube is specified at the beginning of the simulation run. To select a new orientation for the MC move, a random vector from the surface of the unit sphere was generated uniformly, then multipled by a size parameter and added to the old orientation vector. This vector was then normalised to yield a the new unit orientation for the move. As for the position change, the parameter specifying the size of the change of orientation vector influences the acceptance probability, and is input at the beginning of the simulation run. The move size parameters are conventionally chosen to yield accepance ratios somewhere in the region of 30–40%. Performing MC moves in such a manner is fairly standard practice, and is described in more detail elsewhere [Allen, 1996].

The method of sampling may not always be chosen for its uniformity according to the Boltzmann factor. For example, in the constant $[\mu, V, T]$ ensemble, one may wish to bias the attempted insertion of new molecules into the system, in order to have a greater chance of generating a new configuration without an overlap. If we choose new states in such a way that is not reversible, $\alpha_{i\to j}$ is not symmetric and the acceptance ratio will need to include an additional factor, a biasing ratio, in order for the procedure to obey whatever balance condition we would like to impose. The Wang-Landau method actually seeks out states of the system that are away from equilibrium by biasing the system away from the states it has already visited, in order to build a good estimate of the density of states. Technically, this means that the selection algorithm does not generate a Markov chain, and hence does not obey the balance conditions, until the simulation has been performed over sufficiently many MC sweeps for the biasing function to no longer be updated. For systems that involve large changes in density, in order to obtain consistent move acceptance ratios, the size of MC move attempts may depend on its location in the system, meaning that forward moves can be accepted for which the reverse move is not even attempted, due to a smaller cutoff in MC moves at the point at which the reverse move is attempted. Merely inserting a biasing ratio is not sufficient to allow this procedure to obey balance, and the functions that generate move attempts

only within some cutoff distance must be replaced with continuous functions that can attempt a move to anywhere in the system, and an appropriate biasing ratio determined according to the form of the function [Binder, 1979].

Another important consideration in constructing a method to simulate a thermodynamic system is in the choice of the ensemble to employ. The canonical (constant $[N, V, T]$) ensemble is often used for analytical evaluation with straightforward expressions for key quantities, and the constant volume condition allows the pressure to be calculated at various points in the system. However, fixing both the number of particles in the system as well as the dimensions of the system means that, if a bulk density exists for the system, then it will remain at the same value. Different regions of the system may be able to contain different densities of particles in order to minimise the free energy of the system, but finite size affects can make this impossible for constant volume simulations[Allen, 2000a].

It is rare for MC simulations to be performed in the microcanonical (constant $[N, V, E]$) ensemble. They consist of attempts to vary the state of the system whilst keeping the total energy constant, and simply accepting changes immediately that reduce the potential energy of the system [Frenkel and Smit, 1996]. As with the canonical, the potential use for simulation in the microcanonical ensemble is limited by the fixed volume condition. However, simulations may be performed in the constant $[\mu, V, T]$ ensemble, which does not suffer from the constrictions of density as particles are allowed to enter the system at fixed chemical potential μ. But keeping the same volume for the system throughout a simulation can mean that finite-size effects are not balanced out by offsetting affects from other volumes during the run, suggesting that the limitations presented by constant-volume simulations in general are too severe for them to be useful when one can employ an ensemble allowing for volume fluctuations [Frenkel and Smit, 1996].

The isothermal-isobaric (constant $[N, P, T]$) ensemble has an initial advantage due to the fact that most experiments are performed at controlled temperature and pressure. The bulk density of the system can be allowed to vary and certain finite-size effects can prove insignificant as the system would not exist at that volume for a sufficient duration of the simulation to for it to prove problematic. The equations valid for the canonical ensemble need only slight modification, which rarely causes problems. However, when spatial variations in the density and order parameters are under study, the statistical fluctuation in the size of the system can cause larger fluctuations in the profiles, as can be the case with the $[\mu, V, T]$ ensemble.

Some quantities, such as those defined in Fourier space, depend directly on the size of the system. For larger system sizes, the relative stability of these spatial profiles lead many to employ the canonical ensemble [Allen, 1996].

Chapter 3

Description of Liquid Crystals

3.1 Measuring Orientational Order

The second-rank orientational order tensor is defined in terms of molecular orientations, $\boldsymbol{u}$, as [Zannoni, 1979]

$$Q_{\alpha\beta} = \frac{3}{2}\left\langle u_\alpha u_\beta - \frac{1}{3}\delta_{\alpha\beta}\right\rangle_{\boldsymbol{u}} \tag{3.1}$$

for $\alpha, \beta = x, y, z$, where $\delta_{\alpha\beta}$ is the Kronecker Delta [Abramowitz and Stegun, 1965] and $\langle ... \rangle_{\boldsymbol{u}}$ denotes an ensemble average over a set of $N_{\boldsymbol{u}}$ particle orientations. $Q_{\alpha\beta}$ is one of the extensively used quantities in the study of liquid crystals [Allen, 2000a], therefore a number of related quantities will be defined and discussed in this section.

In this form, $Q_{\alpha\beta}$ provides information about the ordering along each of the coordinate axes, as well as within the planes whose bases are composed of two of the three axial unit vectors (coordinate planes). The function $\langle P_2(\boldsymbol{u}\cdot\boldsymbol{v})\rangle$, where $P_2(x) = \frac{1}{2}(3x^2 - 1)$ is the second Legendre polynomial and $\boldsymbol{v}$ is some unit vector, is given for $\boldsymbol{v}$ along the coordinate axes by the diagonal components of $Q_{\alpha\beta}$. These values for $\langle P_2\rangle$ are useful indicators of phases present in systems that exhibit orientational order along the coordinate axes or within the coordinate planes, such as those with director-perturbing boundary conditions (e.g. the wedge system, see Chapter 5 for details) or due to exotic phases such as the cubatic phase (constrained along any of the coordinate axes).

For an orientational distribution that is uniform (corresponding to the isotropic phase), $Q_{\alpha\beta} \equiv 0$ and $\langle P_2(\boldsymbol{u}\cdot\boldsymbol{v})\rangle \equiv 0$. Otherwise, there will be some values for $\boldsymbol{v}$

that will maximise $\langle P_2 \rangle$, and this maximum value will be equal to the nematic order parameter, $S = \langle P_2(\boldsymbol{u} \cdot \boldsymbol{n}) \rangle$, where $\boldsymbol{n}$ is the nematic director. The order tensor can be diagonalised, yielding eigenvalues, $\lambda^{[\gamma]}$, with corresponding eigenvectors, $\boldsymbol{v}^{[\gamma]}$, given by

$$\sum_{\alpha} Q_{\alpha\beta} v_{\alpha}^{[\gamma]} = \lambda v_{\beta}^{[\gamma]} \tag{3.2}$$

where $\alpha, \beta = x, y, z$ and the three $\boldsymbol{v}^{[\gamma]}$ are mutually orthogonal unit vectors.

Each eigenvalue relates to its conjugate eigenvector via $\lambda^{[\gamma]} = \left\langle P_2(\boldsymbol{u} \cdot \boldsymbol{v}^{[\gamma]}) \right\rangle$. $\boldsymbol{v}^{+}$ is the vector that maximises $\langle P_2 \rangle$, hence it corresponds to the largest eigenvalue and one obtains the familiar descriptors of nematic order via $\boldsymbol{n} = \boldsymbol{v}^{+}$ and $S = \lambda^{+}$.

Within the plane perpendicular to $\boldsymbol{n}$, $\langle P_2(\boldsymbol{u} \cdot \boldsymbol{v}) \rangle$ will assume a maximum value with $\boldsymbol{v} = \boldsymbol{v}^{0}$, corresponding to the middle eigenvalue, λ^{0}. The smallest eigenvalue, λ^{-}, corresponds to the vector that minimises $\langle P_2 \rangle$, equal to $\boldsymbol{v}^{-}$.

The idealised models for liquid crystalline mesogens are usually chosen to exhibit certain symmetries, i.e. the interaction potential between molecules is invariant to certain transformations. Any system of particles that are each symmetrical under orientational inversion. $\boldsymbol{u}_i \rightarrow -\boldsymbol{u}_i$, will exhibit phases that are invariant to director inversion. It is important to note that such particle symmetry is not a prerequisite for invariance to director inversion, as the nematic phase is defined as possessing this quality, and many liquid crystalline phases are experimentally observed with this as the case, even for "real" mesogens that are sufficiently asymmetric to exhibit ferroelectricity. Cylindrically symmetrical mesogens can produce phases with such symmetry, but this is not always true, as structure may develop normal to the director (e.g. in chiral phases). This property also allows one to analyse the orientational order of the system with even-ranked order tensors, with all odd-ranked tensors averaging out to zero.

The order tensor is defined such that the trace, $Tr\{Q_{\alpha\beta}\} = \sum_{\alpha} Q_{\alpha\alpha}$, is always 0, independent of the orientational distribution. As the trace is invariant with respect to similarity transformations, such as diagonalisation, $\sum_{\gamma} \lambda^{[\gamma]}$ is also $\equiv 0$. Thus only two of the three eigenvalues, along with their eigenvectors, are required to describe the ordering [Lubensky, 1970].

In the isotropic phase, each eigenvalue $\lambda^{[\gamma]}$ is close to 0, and the director is undefined. However, the general limits on the possible eigenvalues are $0 < \lambda^{+} < 1$, $-\frac{1}{2} < \lambda^{-} < 0$ and $\lambda^{-} < \lambda^{0} < \lambda^{+}$ (note that, whilst bounded by the other eigenval-

ues, the range of possible values of λ^0 is $-\frac{1}{2}$ to $\frac{1}{4}$). This means that, when taking the average of the $\lambda^{[\gamma]}$ from different order tensors (e.g. obtained from different simulation blocks), λ^+ and λ^- will always be statistically distinguishable from zero. Hence an arbitrary decision must be made as to what range the eigenvalues (or the $Q_{\alpha\beta}$) must lie in order for the system to be considered to exhibit the isotropic phase.

In practice, due to finite size effects, simulation values calculated from the isotropic phase for the $\lambda^{[\gamma]}$ may often be considerably different from 0, with the director varying throughout a configuration, as well as from configuration to configuration of the same simulated system. Thus it is essential to build up the order tensor as the average over orientations in many configurations, and then subsequently extract the eigenvalues, in order for the contribution from these noisy, ill-defined directors to cancel and yield all $Q_{\alpha\beta}$ and all $\lambda^{[\gamma]}$ as close to zero as possible. A useful result from the analysis of finite-size effects is the dependence of the eigenvalues of the order tensor on the number of orientations, $N_{\boldsymbol{u}}$, over which $Q_{\alpha\beta}$ is averaged [Eppenga and Frenkel, 1984], given by

$$(\lambda^+, \lambda^0, \lambda^-) \approx \left[\frac{1}{\sqrt{N_{\boldsymbol{u}}}} \left(\frac{\sqrt{3}}{2} + \frac{1}{6\sqrt{N_{\boldsymbol{u}}}} \right), -\frac{1}{3N_{\boldsymbol{u}}}, \frac{1}{\sqrt{N_{\boldsymbol{u}}}} \left(-\frac{\sqrt{3}}{2} + \frac{1}{6\sqrt{N_{\boldsymbol{u}}}} \right) \right] \tag{3.3a}$$

$$= \left[\mathcal{O}(1/\sqrt{N_{\boldsymbol{u}}}), \mathcal{O}(1/N_{\boldsymbol{u}}), \mathcal{O}(1/\sqrt{N_{\boldsymbol{u}}}) \right] , \tag{3.3b}$$

These results not only provide initial values for the arbitrary confidence limits on the eigenvalues mentioned above, but also reveal that the middle eigenvalue is the least susceptible to small system-size effects.

The result (3.3b), coupled with the fact that λ^0 is the only eigenvalue that may reach 0 within statistical error, supports the convention to use the middle eigenvalue to describe orientational order in general, with another order parameter defined as $S' = -2\lambda^0$. In a well-defined uniaxial nematic phase, the eigenvectors in the plane normal to the director become degenerate, thus $\lambda^0 - \lambda^- \to 0$, $-\frac{1}{2} < \lambda^{0,-} < 0$, $S' \to S$ and $0 < S < 1$.

As biaxiality is introduced, the preferential alignment toward some vector normal to and in addition to $\boldsymbol{n}$ causes λ^0 to increase and become distinct from λ^-, with λ^+ decreasing accordingly. A common measure of biaxiality is based upon the difference between these eigenvalues, with $\xi = \frac{2}{3}(\lambda^0 - \lambda^-)$ being a popular choice for the biaxial order parameter. If the tendency to align with $\boldsymbol{v}^0$ were to increase sufficiently to become comparable to the tendency toward $\boldsymbol{n}$ (i.e. as $\left\langle P_2(\boldsymbol{u} \cdot \boldsymbol{v}^0) \right\rangle \to$

$\langle P_2(\boldsymbol{u}\cdot\boldsymbol{n})\rangle$), then one would observe $\lambda^+ - \lambda^0 \to 0$ and degeneracy is approached between $\boldsymbol{v}^+$ and $\boldsymbol{v}^0$ for the director, with a value of $-\lambda^-/2$ acting as a lower bound for λ^+ and an upper bound for λ^0. This behaviour of the middle eigenvalue for the intermediate angular distributions between the uniaxial and biaxial phases has an unfortunate consequence on using λ^0 to determine the phase present; for some degree of biaxiality, $\lambda^0 \to 0$, which is similar to its behaviour in the isotropic phase. Hence, for phases where the middle eigenvalue ≈ 0, it is necessary to examine the other order parameters to determine whether the system is exhibiting the isotropic phase, or some intermediate between the uniaxial nematic and a biaxial phase.

Having calculated these order parameters, one may reconstruct the order tensor in terms of the $\lambda^{[\gamma]}$ and $\boldsymbol{v}^{[\gamma]}$ via [Lubensky, 1970]

$$Q_{\alpha\beta} = \frac{3}{2}\lambda^+\left(v_\alpha{}^+ v_\beta{}^+ - \frac{1}{3}\delta_{\alpha\beta}\right) + \frac{1}{3}(\lambda^0 - \lambda^-)\left(v_\alpha{}^0 v_\beta{}^0 - v_\alpha{}^- v_\beta{}^-\right) \tag{3.4}$$

where biaxiality is accounted for by a factor of $\lambda^0 - \lambda^-$ in the second term, which converges to 0 for uniaxial phases.

As has been discussed, the second-rank order tensor can give indications of the orientational distribution of a system. There are, however, examples of distribution functions that, whilst containing different distinguishing features, will yield the same order tensor. For example, all of the $Q_{\alpha\beta} \to 0$ in the cubatic phase, in a similar manner to the isotropic phase, despite the presence of three equivalent, yet mutually orthogonal, directors. In order to distinguish between the isotropic and cubatic phases, a fourth-rank order tensor may be used, with higher-rank tensors providing more detailed information on the orientational distribution.

When measuring several order tensors, providing averages over different configurations or regions of a system, any significant variation of the director between measurements can be informative. For phases in which the director is poorly defined, some of the eigenvectors of the order tensor are degenerate, and the measured value for $\boldsymbol{n}$ will vary considerably between all of these possible vectors. In the isotropic phase, the director will vary uniformly about all orientations. Similarly, for planar phases exhibiting tendency to align within a plane, $\boldsymbol{n}$ varies uniformly within the plane. For more structured phases, such as the cubatic, the director will vary between vectors approximately parallel to one of the three characteristic mutually perpendicular directors. So, although the cubatic and isotropic phases might each exhibit an identical order tensor, in practice the distribution of $Q_{\alpha\beta}$ will be noti-

cably different. This can provide a practical method for determining the phase of a system, without need for the calculation of higher-rank order tensors. Although not using a quantitative measure of the difference between the phases, this may be appropriate when the system under consideration is sufficiently well-studied to exclude the exhibition of one phase.

3.2 Elastic Theory

For bulk systems in the nematic phase, slowly-varying spatial inhomogeneities in the director field $\boldsymbol{n}$ give rise to the following free energy penalty [Frank, 1958]:

$$\Delta\mathcal{F} = \frac{1}{2}\int \mathrm{d}\boldsymbol{r}\left\{K_1\Big[\nabla\cdot\boldsymbol{n}(\boldsymbol{r})\Big]^2 + K_2\Big[\boldsymbol{n}(\boldsymbol{r})\cdot\big(\nabla\wedge\boldsymbol{n}(\boldsymbol{r})\big)\Big]^2 + K_3\Big|\boldsymbol{n}(\boldsymbol{r})\wedge\big(\nabla\wedge\boldsymbol{n}(\boldsymbol{r})\big)\Big|^2\right\} \tag{3.5}$$

where K_1, K_2 and K_3 are the splay, twist and bend Frank elastic constants respectively.

The rotational invariance of bulk geometry means that the average director $\boldsymbol{n}$ can vary with time throughout simulations, leading to complications in describing system quantities in reciprocal space. Such complications are removed by ensuring a roughly constant director, which will remain constrained along a preferred direction ($\hat{\boldsymbol{z}}$) within some tolerance throughout the simulation. Hence we consider also the effect of a small orienting field, $f_{\mathrm{ext}}(\boldsymbol{r})$, giving the free energy contribution per molecule due to the external field. f_{ext} will depend on features of the orientational distribution, specified by the order parameter, S, and director, $\boldsymbol{n}$, as well as the precise form of the field applied in simulation.

The external field will contribute the following term to the free energy:

$$\int \mathrm{d}\boldsymbol{r}\rho(\boldsymbol{r}) f_{\mathrm{ext}}\left(S(\boldsymbol{r}),\boldsymbol{n}(\boldsymbol{r})\right)\ , \tag{3.6}$$

and the external potential applied in our simulations (see Chapter 4) provides a free energy per molecule at point $\boldsymbol{r}$ given by

$$f_{\mathrm{ext}}(S,\boldsymbol{n}) = SU\left(1-(\boldsymbol{n}\cdot\hat{\boldsymbol{z}})^2\right)\ . \tag{3.7}$$

The value of the field parameter U can be chosen to be reasonably small while

preventing $\boldsymbol{n}$ from wandering far from $\hat{\boldsymbol{z}}$.

The thermal fluctuations of the director are best described by a spectrum of modes. Decomposing the director with the Fourier transform pair

$$\boldsymbol{n}(\boldsymbol{r}) = \frac{1}{V}\sum_{\boldsymbol{k}} \tilde{\boldsymbol{n}}(\boldsymbol{k}) \exp(-\mathrm{i}\boldsymbol{k}\cdot\boldsymbol{r}_i) \tag{3.8}$$

$$\tilde{\boldsymbol{n}}(\boldsymbol{k}) = \int \boldsymbol{n}(\boldsymbol{r}) \exp(\mathrm{i}\boldsymbol{k}\cdot\boldsymbol{r}_i)\mathrm{d}\boldsymbol{r} \tag{3.9}$$

allows one to work in reciprocal space with the Fourier components of the director, $\tilde{\boldsymbol{n}}(\boldsymbol{k})$. A consistent manner of describing such spectra involves a change of coordinate system from the fixed $\boldsymbol{xyz}$-frame to a $\boldsymbol{k}$-dependent **123**-frame, where **3** is fixed along the desired director (the z-axis), **1** is defined perpendicular to **3** such that the wavevector $\boldsymbol{k}$ is in the **13**-plane and **2** is perpendicular to both $\boldsymbol{n}$ and $\boldsymbol{k}$. Hence the wavevector coordinates reduce to $\boldsymbol{k} = (k_1, 0, k_3)$.

For small variations of $\boldsymbol{n}$ away from the 3-direction, $n_3(\boldsymbol{r}) \approx 1$ and the distortion free energy, perturbed by the external field, can be written in terms of the Fourier transforms $\tilde{n}_1(\boldsymbol{k})$, $\tilde{n}_2(\boldsymbol{k})$, of the remaining components:

$$\mathcal{F} = \frac{1}{2V}\sum_{\boldsymbol{k}} K_1 k_1^2 \left|\tilde{n}_1(\boldsymbol{k})\right|^2 + K_2 k_1^2 \left|\tilde{n}_2(\boldsymbol{k})\right|^2 + \left(K_3 k_3^2 + 2\rho SU\right)\left(\left|\tilde{n}_1(\boldsymbol{k})\right|^2 + \left|\tilde{n}_2(\boldsymbol{k})\right|^2\right) , \tag{3.10}$$

According to equipartition of energy each mode is assigned an energy of $k_B T/2$ and hence

$$\left\langle \left|\tilde{n}_\alpha(\boldsymbol{k})\right|^2 \right\rangle = \frac{V k_B T}{K_\alpha k_1^2 + K_3 k_3^2 + 2\rho SU} \ , \ \alpha = 1, 2 \ . \tag{3.11}$$

This is valid in the limit of low k. There will be terms above second order that will begin to dominate as k increases, until the function reaches its limiting value.

The use of the above expressions to calculate elastic constants from molecular simulations is well established [Allen and Frenkel, 1988, 1990; Tjipto-Margo et al., 1992; Allen et al., 1996], and so only a brief description will be given here. It is convenient to work with the order tensor, $Q_{\alpha\beta}$, for the representation of orientational correlations in the nematic phase. For molecular orientations represented by unit vectors $\boldsymbol{u}_i = (u_{ix}, u_{iy}, u_{iz})$,

$$Q_{\alpha\beta}(\boldsymbol{r}) = \frac{V}{N}\sum_{i=1}^{N} \frac{3}{2}\left(u_{i\alpha}u_{i\beta} - \tfrac{1}{3}\delta_{\alpha\beta}\right)\delta(\boldsymbol{r} - \boldsymbol{r}_i) \ . \tag{3.12}$$

where $\alpha, \beta = x, y, z$, $\delta_{\alpha\beta}$ is the Kronecker delta and $\delta(\cdots)$ is the Dirac delta function. The order parameter S, a measure of the degree of mutual alignment, is found from the highest eigenvalue of the volume-averaged order tensor, with the director $\boldsymbol{n}$ given by the corresponding eigenvector. It is easy to show that $S = \langle P_2(\boldsymbol{u}_i \cdot \boldsymbol{n})\rangle$ where P_2 is the second Legendre polynomial. The Fourier components of the order tensor,

$$\tilde{Q}_{\alpha\beta}(\boldsymbol{k}) = \frac{V}{N}\sum_{i=1}^{N}\frac{3}{2}\left(u_{i\alpha}u_{i\beta} - \tfrac{1}{3}\delta_{\alpha\beta}\right)\exp(\mathrm{i}\boldsymbol{k}\cdot\boldsymbol{r}_i) \tag{3.13}$$

can be related, at low k, to those of the director via

$$\left\langle \left|\tilde{Q}_{\alpha 3}(\boldsymbol{k})\right|^2 \right\rangle \equiv \tfrac{9}{4}S^2\left\langle \left|\tilde{n}_{\alpha}(\boldsymbol{k})\right|^2 \right\rangle \tag{3.14}$$

as $n \approx 1$. Thus we obtain for the order tensor spectrum [Forster, 1975]:

$$\left\langle \left|\tilde{Q}_{\alpha 3}(\boldsymbol{k})\right|^2 \right\rangle = \frac{\frac{9}{4}S^2 V k_B T}{K_\alpha k_\alpha^2 + K_3 k_3^2 + 2\rho S U}\,. \tag{3.15}$$

The elastic constants can then be obtained from the function

$$\mathcal{W}_{\alpha 3}(\boldsymbol{k}) \equiv \frac{\frac{9}{4}S^2 V k_B T}{\langle|\tilde{Q}_{\alpha 3}(\boldsymbol{k})|^2\rangle} \longrightarrow K_\alpha k_\alpha^2 + K_3 k_3^2 + 2\rho S U \qquad \text{as } k \to 0 \tag{3.16}$$

fitted to the simulation data.

This expression for the fluctuation modes follows directly from the Frank-Oseen distortion free energy of eqn (3.5), thus is valid only for long wavelength modes. As k increases, the deviation of $\mathcal{W}_{\alpha 3}$ from this relationship illustrates the length scales over which the elastic theory provides a good description. In the case of high k the function will converge to a limiting value [Forster, 1975]

$$\mathcal{W}_{\alpha 3}(\boldsymbol{k}) \longrightarrow \frac{\overline{P_2^2}\rho k_B T}{\frac{1}{21}\overline{P_2} - \frac{4}{35}\overline{P_4} + \frac{1}{15}} \qquad \text{as } k \to \infty\,, \tag{3.17}$$

involving both average second- and fourth-order polynomials of $\boldsymbol{u}_i \cdot \boldsymbol{n}$.

3.3 Density Functional Theory

Density functional theory (DFT) involves expressing the free energy of the system as some functional of the single particle density distribution function of the coordinates

of the system, and then finding the precise density function that minimises this free energy, hence obtaining the equilibrium distribution of states. For example, the Grand Potential of a system of liquid crystal molecules would have the following form [Camp and Allen, 1996];

$$\Omega[\rho(\mathbf{r},\omega)] = F_{\text{id}}[\rho(\mathbf{r},\omega)] + F_{\text{ex}}[\rho(\mathbf{r},\omega)] + F_U[\rho(\mathbf{r},\omega)] + F_\mu[\rho(\mathbf{r},\omega)] \tag{3.18}$$

where F_{id} is the ideal gas contribution to the free energy, consisting of individual single-body energy terms (i.e. no interaction between particles), F_{ex} is the excess contribution considering multi-particle interactions, F_U the contribution from some external potential field $U(\mathbf{r},\omega)$ and F_μ is the contribution from the interchange of particles to and from the system at fixed chemical potential μ.

This is a classical theory, and the ideal gas term can be expressed as follows;

$$\beta F_{\text{id}}[\rho(\mathbf{r},\omega)] = \int d^3\mathbf{r} \int d^2\omega\ \rho(\mathbf{r},\omega)\left(\log(\rho(\mathbf{r},\omega)\Lambda^3) - 1\right) \tag{3.19}$$

This term is the kinetic contribution to the free energy, with Λ being the de Broglie mean thermal wavelength, an arbitrary length that provides a normalising volume for the chemical potential.

The term arising from the fixed chemical potential (μ) of the system ensures that the distribution functions considered do not have the normalisation constriction

$$\int d^3\mathbf{r} \int d^2\omega\ \rho(\mathbf{r},\omega) = N = \text{constant} \tag{3.20}$$

where N is the number of particles in the system whilst the particular functional distribution $\rho(\mathbf{r},\omega)$ exists. In other words, by fixing the chemical potential and not the number of particles, we are allowing the distribution function more freedom in variation to give the minimum free energy of the system. Its contribution to the free energy is given by

$$\beta F_\mu[\rho(\mathbf{r},\omega)] = \int d^3\mathbf{r} \int d^2\omega\ \beta\mu\ \rho(\mathbf{r},\omega) \tag{3.21}$$

The contribution to the free energy from single-body interactions with "external" parameters, like under consideration of an energy incentive for the molecules

supplied by an external field $U(\mathbf{r}, \omega)$, can be written as

$$\beta F_{\mathrm{U}}(\rho) = \int d^3\mathbf{r} \int d^2\omega \; \rho(\mathbf{r}, \omega)\beta U(\mathbf{r}, \omega) \; . \tag{3.22}$$

These contributions thus far are sufficient to generate a first-order approximation for the depletion forces of a liquid crystalline system between walls, and for relatively simple particle-wall interaction potentials, $U(\mathbf{r}, \omega)$, the solutions can often be expressed analytically.

The precise form of F_{ex} is not generally known. What is known is that it incorporates interactions between particles, from two-particle effects upwards, and is equal to a sum over all such multiple-body interactions. There are numerous approximations [Chen and Noolandi, 1992], and we can use the Onsager approximation for pairs of molecules to obtain

$$\beta F_{\mathrm{ex}} = -\frac{1}{2} \int d^3\mathbf{r}_1 \int d^3\mathbf{r}_2 \int d^2\omega_1 \int d^2\omega_2 \; \rho(\mathbf{r}_1, \omega_1)\rho(\mathbf{r}_2, \omega_2) \, f(\mathbf{r}_1, \omega_1, \mathbf{r}_2, \omega_2) \tag{3.23}$$

where $f(\mathbf{r}_1, \mathbf{r}_2, \omega_1, \omega_2)$ is known as the Mayer f-function, given by

$$f(\mathbf{r}_1, \mathbf{r}_2, \omega_1, \omega_2) = f(\mathbf{r}_{12}, \omega_1, \omega_2) = \mathrm{e}^{-V_{12}(\mathbf{r}_1, \omega_1, \mathbf{r}_2, \omega_2)/kT} - 1 \tag{3.24}$$

where $V_{12}(\mathbf{r}_1, \omega_1, \mathbf{r}_2, \omega_2)$ is the interaction potential between particle pairs. The Onsager approximation holds for any pair interaction potential V_{12}, and, particularly for liquid crystals, it is common to use the hard-core interaction potential based on abrupt steric repulsion between particles. For hard-core interactions, V_{12} will be infinity as particles 1 and 2 overlap, and equal to zero in the case of no overlap. Hence the Mayer f-function takes the value 0 when there is no overlap between the molecules, and -1 when they do overlap.

The steric repulsion between pairs results in an alternative representation of (3.23) due to the exclusion of particles from the space occupied by their neighbours. For the bulk case (no $\mathbf{r}$-dependence in ρ), this is given by

$$\beta F_{\mathrm{ex}}/V = \frac{1}{2} \int d^2\omega_1 \int d^2\omega_2 \; \rho(\omega_1) \; \rho(\omega_2) \; \mathcal{V}(\omega_1, \omega_2) \tag{3.25}$$

where V is the volume of the system and $\mathcal{V}$ is the orientation-dependent excluded

volume for the pair of particles with orientations ω_1 and ω_2, defined by

$$\mathcal{V}(\omega_1, \omega_2) = -\int d^3\mathbf{r}_{12}\ f(\mathbf{r}_{12}, \omega_1, \omega_2) \tag{3.26}$$

i.e. for any volume elements in which the particles do overlap, f is -1, and is 0 otherwise, meaning that the amount of volume from which particles with orientations ω_1 and ω_2 will be excluded is $\mathcal{V}$.

When considering other multiple-particle interactions, one could add a term to the interaction potential in (3.24), which would model the precise interaction using the Onsager approximation. However, it is more convenient to represent its contribution to the free energy as a direct perturbation as follows (for each general n-body interaction);

$$\beta F_{\mathrm{n}} = \frac{1}{n!}\int d^3\mathbf{r}_1 ... \int d^3\mathbf{r}_{\mathrm{n}} \int d^2\omega_1 ... \int d^2\omega_{\mathrm{n}}\ \rho(\mathbf{r}_1, \omega_1)...\rho(\mathbf{r}_{\mathrm{n}}, \omega_{\mathrm{n}})\ V_{\mathrm{n}}(\mathbf{r}_1, \omega_1, ..., \mathbf{r}_{\mathrm{n}}, \omega_{\mathrm{n}}) \tag{3.27}$$

where V_{n} is the interaction potential between the n particles. The positive sign ensures that preparation of the system under an attractive potential will lower the free energy and preparation under a repulsive potential will increase the free energy. The $1/n!$ factor ensures that each phase space volume element $d^3\mathbf{r}_1 d^2\omega_1 ... d^3\mathbf{r}_{\mathrm{n}} d^2\omega_{\mathrm{n}}$ contributes to the free energy only once as the n integrations cover it. The perturbation terms are usually truncated at order two, giving the two-body interaction contribution which give contribution

$$\beta F_2 = \int d^3\mathbf{r}_1 \int d^3\mathbf{r}_2 \int d^2\omega_1 \int d^2\omega_2\ \rho(\mathbf{r}_1, \omega_1)\rho(\mathbf{r}_2, \omega_2)\, V_2(\mathbf{r}_1, \omega_1, \mathbf{r}_2, \omega_2) \tag{3.28}$$

Common two-body interactions used in molecular simulation include the familiar Lennard-Jones and electrostatic potentials, as well as idealised approximations such as square wells. The Lennard-Jones potential is used to describe systems of atoms, and the electrostatic used for systems with charged constituents (e.g. for conduction theory), hence these are only usually utilised in the theory of liquid crystals for realistic atomic detail [Wu et al., 1998].

Onsager [Onsager, 1949] was the first to deal with such a functional as equation (3.18), and used a variational method to estimate the equilibrium distribution of the system. With his trial functional substituted into the functional, the resulting free energy was then a function of the parameter α. Hence the grand potential can

be minimised with respect to α to find the equilibrium distribution. This treatment can give analytical predictions of such liquid crystal behaviour as phase coexistence densities, although the restriction on the model by the assumptions that must be made to have such an analytical approach can limit the range of application of the method as well as its accuracy.

DFT has also been performed extensively using numerical methods. It is common practice to reduce the integrals given by equations (3.18)-(3.28) to sums over spherical harmonic coefficients. An initial distribution function may be specified, the necessary coefficients computed, and these are used as a starting point in iterating the free energy of the system down toward the global minimum using the conjugate gradient method [Osipov and Hess, 1993].

Higher order terms in the virial expansion will take the place of integrals over more than sets of two coordinates, and the evaluation of these integrals is significantly more complicated. They often need to be estimated directly by some numerical method, such as Monte Carlo integration. All observables in DFT have expansions in a sequence of terms for the order of interaction, expressed as as integrals. Expressions for the elastic constants exist, and the second order approximation utilises the spherical harmonic coefficients of the Mayer function, allowing us to modify our procedure for Onsager theory and yield the elastic constants at this virial level. Of course, second order virial theory is very limited for DFT, and we rely on the work with the higher virials for a better theoretical description of the elastic constants.

Chapter 4

Elastic constants by Monte Carlo simulation

4.1 Simulation Details

The orienting field of eqn (3.6) is applied in the simulation as the following potential energy term:

$$\mathcal{U}_{\text{ext}} = U \sum_{i=1}^{N} \left(1 - (\boldsymbol{u}_i \cdot \hat{\boldsymbol{z}})^2\right) , \tag{4.1}$$

where $\boldsymbol{u}_i$ denotes the orientation of molecule i. We must perform some operations to convert this potential into the form of eqn (3.6). Consider a region of nematic consisting of $N_{\boldsymbol{u}}$ molecules, with director $\boldsymbol{n}$ and order parameter S. One may rewrite eqn (4.1) as

$$\begin{aligned} \mathcal{U}_{\text{ext}} &= U \sum_{i=1}^{N_{\boldsymbol{u}}} \left(u_{ix}^2 + u_{iy}^2\right) \\ &= N_{\boldsymbol{u}} U \left(\langle u_x^2 \rangle_{\boldsymbol{u}} + \langle u_y^2 \rangle_{\boldsymbol{u}}\right) . \end{aligned} \tag{4.2}$$

According to eqn (3.4), for a uniaxial nematic, the order tensor may be written as

$$Q_{\alpha\beta} = \frac{3}{2} S \left(n_\alpha n_\beta - \frac{1}{3} \delta_{\alpha\beta} \right) . \tag{4.3}$$

and, when combined with the definition of $Q_{\alpha\beta}$ (see eqn (3.1)) we yield the following expression for the averages of second order multiples of orienation components

$$\langle u_\alpha u_\beta \rangle_{\boldsymbol{u}} = S n_\alpha n_\beta \; . \tag{4.4}$$

Hence we obtain an expression for the external contribution to the potential per particle for this region,

$$\begin{aligned} \mathcal{U}_{\rm ext}/N_{\boldsymbol{u}} &= SU\big(n_x^2 + n_y^2\big) \\ &= SU\big(1 - [\boldsymbol{n}\cdot\hat{\boldsymbol{z}}]^2\big) \; . \end{aligned} \tag{4.5}$$

This justifies our selection of $f(\boldsymbol{r})$, the external field contribution per unit molecule, as $SU\big(1-[\boldsymbol{n}(r)\cdot\hat{\boldsymbol{z}}]^2\big)$. A value of the field strength parameter $U/k_{\rm B}T = 0.1$ was found to ensure that the z-component of $\boldsymbol{n}$ remained within 0.1% of 1.

In the simulation, the wavevectors of orientational distortions are determined by the size of the system via

$$\boldsymbol{k} = 2\pi(\frac{\kappa_x}{\mathcal{L}_x}, \frac{\kappa_y}{\mathcal{L}_y}, \frac{\kappa_z}{\mathcal{L}_z}) = k_0(\kappa_x, \kappa_y, \gamma\kappa_z) \; , \tag{4.6}$$

where $k_0 = 2\pi/\mathcal{L}$, $\mathcal{L}_{x,y} = \mathcal{L}$ and $\mathcal{L}_z$ are the lengths of the simulation box, $\gamma = \mathcal{L}/\mathcal{L}_z$ accounts for a non-cubic system and the κ_α are integers chosen to range from 0 to some upper bound large enough to observe convergence of $\mathcal{W}_{\alpha 3}$ to the high-k limit.

The calculation of director fluctuation spectra is quite expensive, and the low-k fluctuations are quite slow, in practice taking the time equivalent to several MC sweeps: therefore contributions to $\mathcal{W}_{\alpha 3}$ may be computed more frequently for low values of k, saving time by skipping some calculations for the higher-k modes, which are less critical in estimating the elastic constants. Hence the distinction between high- and low- k modes is an arbitrary choice, representing a trade-off between accuracy of middle-k data and efficient use of computer resources, which must be made from inspection of the spectra. In order to obtain the director fluctuations in a convenient form, the molecular orientations must first be transformed from the fixed $\boldsymbol{xyz}$-frame into the director-defined **123** coordinate system. The aim of the orienting field is to simplify this transformation. The functions $|\tilde{Q}_{\alpha 3}(\boldsymbol{k})|^2$ can then be calculated for the desired wavevector spectrum from eqn (3.13), saved at regular intervals and statistical uncertainties estimated from the variation over several blocks of MC sweeps.

After obtaining the spectra, the functions $\mathcal{W}_{\alpha 3}(\boldsymbol{k})$ were found from eqn (3.16) and were fitted to a ratio of multivariate polynomials in k_1^2 and k_3^2. The polynomials were chosen so as to ensure that the leading coefficients in the numerator provided estimates for the elastic constants and the trial function converged to the limit of eqn (3.17) for high k.

In the least-squares fitting of the trial function to fluctuation data, the estimates for the elastic constants are sensitive to several details of the fitting procedure. The range of the $\boldsymbol{k}$-spectrum used in the fit largely determines the extent to which the fitting function describes the behaviour at high k, whereas an accurate description of the low-k modes will give the most accurate values for the elastic constants. Hence changing the limiting values of k_1 and k_3 will change the relative weighting of the low-k data in the fit.

Also to be considered when choosing these limiting values for the k_α is the effect of the onset of translational order on the fluctuation spectra. As we study state points close to the phase transtitions in which positional order is approached in the α-direction, the spectra for values of k_α close to $2\pi/\lambda_\alpha$, where λ_α is a characteristic correlation length for positions in the α-direction, become distorted away from those that can be easily fitted with a smooth, gradually varying, simple function. In numerical minimisation routines, as utilized in the least squares fitting, more complicated functions can induce pathological behaviour and may also affect the extrapolated initial gradients in subtle ways. Since the emphasis for the fitting is firmly on extracting leading coefficients from the low-k data, we chose to select limiting values so as not to intrude on the regions in which this distortion takes place. As one measures fluctuations from state points within the translationally ordered states, the spectra become subject to significant statistical noise around the wavevector associated with λ_α, hence the director fluctuations serve as an abrupt indicator that the nematic phase is no longer under observation.

Another feature of the fitting is the number of parameters in the fitting function, determining the freedom of the function to match the simulation data. Increasing the number of parameters can allow the function to follow the high-k data more closely, at a cost of reducing the accuracy for lower k. Several choices for the number of parameters and range of $\boldsymbol{k}$-spectrum were used, and the leading coefficients averaged over these choices to provide estimates for the elastic constants with associated fitting error. These limits imposed by the fitting turned out to be larger than the statistical errors for the runs conducted here.

In order to analyse the translationally ordered phases, the structure factor is calculated

$$\tilde{g}(\boldsymbol{k}) = \frac{1}{N}\sum_{i=1}^{N}\sum_{j=1}^{N}\exp(\mathrm{i}\boldsymbol{k}\cdot(\boldsymbol{r}_i - \boldsymbol{r}_j)) \;, \tag{4.7}$$

and it is straightforward to show that eqn (4.7) reduces to

$$\tilde{g}(\boldsymbol{k}) = \frac{1}{N}\Big|\sum_{i=1}^{N}\exp(\mathrm{i}\boldsymbol{k}\cdot\boldsymbol{r}_i)\Big|^2 \;. \tag{4.8}$$

This calculation can be computationally expensive, even more so than the calculation of director fluctuations, each one taking more than the equivalent CPU time for 100 MC sweeps. Therefore it is convenient to save configurations to be processed after the simulation, and the choice of how many occurrences to record will be some tradeoff between quality of structure factor spectra, and memory issues combined with the CPU time taken to analyse a particular number of configurations. Another benefit of analysing the configurations afterwards is that, if the wavevector spectrum studied during any first analysis were found to be insufficient to observe all of the interesting structure, the procedure could simply be repeated over a different range of spectrum without the need for more MC simulation runs.

The structure factor can be expressed as Fourier components of the pair distribution function, $g(\boldsymbol{r})$, for a system with uniform density ρ, as follows;

$$\tilde{g}(\boldsymbol{k}) = 1 + \rho\int_V g(\boldsymbol{r})\exp(\mathrm{i}\boldsymbol{k}\cdot\boldsymbol{r})\mathrm{d}\boldsymbol{r} \tag{4.9a}$$

$$g(\boldsymbol{r}) = \frac{1}{V}\sum_{\boldsymbol{k}}\frac{\tilde{g}(\boldsymbol{k})-1}{\rho}\exp(\mathrm{i}\boldsymbol{k}\cdot\boldsymbol{r}) \;. \tag{4.9b}$$

This suggests that it is not entirely physically irrelevant to follow the cumulative behaviour of $\tilde{g}(\boldsymbol{k})$, which converges to 1 for high k. In practice, the structure factor will contain peaks corresponding to types of positional order, the intensity distribution of which will determine what phase is present in the simulation. The area under each peak provides a more accurate measure of the degree of ordering than merely the peak height, hence the cumulative function

$$G(k_z) = \frac{k_0}{N}\sum_{0<k_z'\leq k_z}\tilde{g}(k_{x,y}=0,k_z') - 1 \tag{4.10}$$

is an informative quantity. The factor k_0 appearing in eqn (4.10) arbitrarily normalises the function to be similar in magnitude to the integral of a continuous function fitted to $\tilde{g}(\boldsymbol{k})$. Upon inspection of $G(k_z)$, the integrated intensity of each peak will be noticeable in relation to the others.

4.2 Spherocylinders

4.2.1 System Details

The simulated system consists of a fluid of hard spherocylinders (interaction potential between a pair of molecules $V_{ij} = \infty$ if the molecules overlap, and zero otherwise), with diameter D, distance L between the centres of the spherical end caps, and $L/D = 5$. The overlap criterion is described elsewhere [Allen et al., 1993]. For this system, due to the absence of any finite interaction potentials, the temperature is irrelevant, except as a scaling factor for energies and free energies. Reduced units of energy in these simulations are obtained by taking $k_{\mathrm{B}}T = 1$ and reduced units of distance by setting the platelet diameter $D = 1$.

Monte Carlo simulations were performed for systems of 8000 particles with cuboidal periodic boundary conditions in the canonical ensemble. Equilibration runs consisted of at least 10^5 sweeps, and simulation averages were taken during production runs of 2×10^6 sweeps (1 sweep = 1 attempted MC move, combined translation and rotation, per particle). Displacement parameters were chosen to give a move acceptance rate in the range 30–40%.

It is conventional to express density relative to the density of a close-packed system containing molecules arranged on a hexagonal close-packed or face-centred cubic lattice, which is given by

$$\rho_{\mathrm{cp}} D^3 = \frac{2}{\sqrt{2} + (L/D)\sqrt{3}} \,. \tag{4.11}$$

Of the state points chosen, the densities ranging $\rho/\rho_{\mathrm{cp}} = 0.453$ – 0.504, lie in the nematic region for $L/D = 5$ spherocylinders; the isotropic-nematic transition occurs at $\rho/\rho_{\mathrm{cp}} \approx 0.450$; the nematic–smectic-A transition begins at $\rho/\rho_{\mathrm{cp}} \approx 0.51$ [Bolhuis and Frenkel, 1997]. Average values of order parameter for each density are reported in Table 4.1.

The way in which the initial configurations are set up can be important. For our simulations, it was desirable to run for the many systems concurrently, so a

ρ/ρ_{cp}	S	$K_1 D/k_{\mathrm{B}}T$	$K_2 D/k_{\mathrm{B}}T$	$K_3 D/k_{\mathrm{B}}T$
0.453	0.446(4)	0.201(5)	0.109(2)	0.33(1)
0.458	0.509(3)	0.27(1)	0.144(3)	0.45(6)
0.463	0.561(3)	0.356(6)	0.174(3)	0.60(7)
0.469	0.603(2)	0.444(7)	0.234(3)	0.65(6)
0.474	0.639(2)	0.51(2)	0.245(5)	0.91(8)
0.479	0.669(1)	0.62(2)	0.26(2)	1.5(1)
0.484	0.692(1)	0.68(2)	0.298(5)	1.3(1)
0.489	0.715(1)	0.78(2)	0.35(1)	1.3(1)
0.494	0.737(1)	0.90(2)	0.37(1)	1.7(1)
0.499	0.758(1)	1.00(3)	0.39(1)	2.0(1)
0.503	0.7753(9)	1.18(1)	0.456(8)	2.08(5)

Table 4.1: Density ρ/ρ_{cp} of each simulation, with simulation averages of order parameter S, and elastic constants $K_\alpha D/k_{\mathrm{B}}T$. Figures in parentheses represent estimated errors in the last quoted digit.

highly dense configuaration of spherocylinders on a cuboidal crystalline lattice was created, and this configuration was expanded to form an initial arrangement for the system at each density. Upon equilibration runs, for any densities that lie in the nematic region, the crystal would "melt", with the positional order dissipating, allowing a nematic to form. It can be difficult, however, to achieve equilibration of a smectic phase in the cananical ensemble, with nonequilibrium states being misrepresented as equilibrium states. Anisotropic values for the pressure tensor have been calculated to confirm this assertion, with constant $\{NPT\}$ ensemble incorporating independently varying box lengths being required to relieve anisotropic stress. Even once the anisotropy is relaxed out, the smectic layering can still depend on the initial configuration, independent of the simulation method [Dominguez et al., 2002].

The phases exhibited by molecular systems can also be modified by the application of external fields, the extent of which is aptly illustrated by fully aligned spherocylinders exhibiting a columnar phase [Veerman and Frenkel, 1991]. Even small values for the aligning field strength may perturb the orientational distribution, modifying the phase behaviour [Martín del Río and de Miguel, 2006], hence the phases present in any system with an aligning field must be checked. Positionally ordered phases in the $\{NVT\}$ ensemble may relieve stress anisotropy by packing with orientations along the diagonal of the box, which is prevented by our gentle aligning field along a specific axis ($= \hat{\boldsymbol{z}}$). This restriction, along with the fixed box lengths for the calculation of reciprocal space quantities, means that our simulations

are unlikely to yield true equilibrium states. Our primary focus is on the elastic constants in the nematic phase, so we examine phase behaviour in order to be certain of nematic state points, but our results yielding translational order must be viewed in the context of frustrated systems.

The calculation of director fluctuation spectra was performed every 10^2 MC sweeps, with configurations for the structure factor recorded every 10^3 sweeps. In the calculation of director fluctuation spectra, it was desirable for the limiting values on the wavevector spectrum to be large enough to observe the high-k behaviour of the functions $W_{\alpha 3}(\boldsymbol{k})$, and hence the maximum values were chosen to be $\kappa_{x,y,z} = 30$.

The onset of smectic order causes structure to develop along the **3**-direction in the region of $k_3(L+D)/2\pi = 1$, with $(L+D)$ being the length of a molecule and thus a reasonable first approximation for an interlayer spacing. Hence, in the fitting of $W_{\alpha 3}$, only data points for k_3 up to some maximum value below $2\pi/(L+D)$ are included in each fitting procedure. Initially, simulations were performed for a cubic system, but the fluctuation structure in the 3-direction causing a necessary fitting cutoff after only a few data points prompted a change to a cuboidal simulation box, with $\mathcal{L}_z/\mathcal{L}_{x,y} = 2^{3/2}$. This was performed using an adjusting procedure that included one attempted change in box aspect ratio per MC sweep, therefore maintaining system volume and thus overall density.

The three different limiting values in the fitting process for $k_3(L+D)/2\pi$ were 3/5, 2/3 and 3/4. With the onset of crystalline order, a correlation distance in the **1**-direction of the order of D will induce structure in the $W_{\alpha 3}$. This, however, is not approached whilst still in the nematic phase, meaning that it was sufficient to set the upper bounds in the fitting for $k_1 D/2\pi$ to 1/3, 5/12 and 1/2. Another consequence of translational ordering is the twist and bend elastic constants being predicted to diverge at the nematic-smectic transition [Oswald and Pieranski, 2006], which can be understood on geometrical grounds as the correlation length for smectic order grows. For the positionally ordered phases, there will also be non-zero values for compression moduli, or translational elastic constants, in the direction of ordering (the interlayer vector in this case).

4.2.2 Phase Behaviour

Figure 4.1 shows the sixteen state points examined here, expected to be spread across three distinct phases, outside of the coexistence regions, due to the work of Bolhuis and Frenkel [1997]. In a first effort to ensure this, one can examine

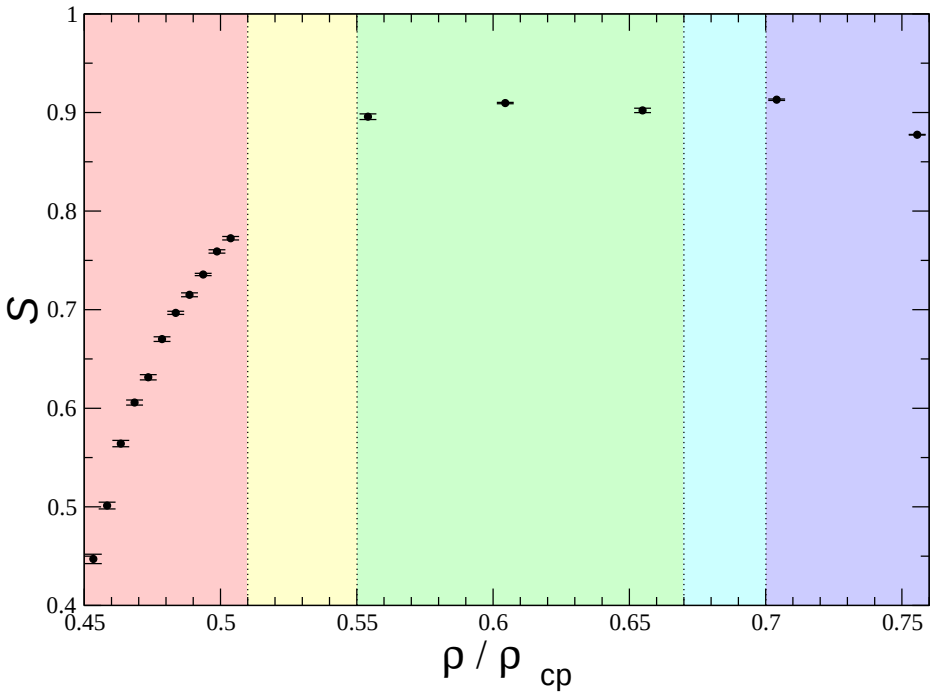

Figure 4.1: The nematic order parameter against density as observed in our systems of spherocylinders. According to Bolhuis and Frenkel [1997], the state points observed should be situated across three (sometimes coexisting) phases, shown by colour coded regions; Nematic (red); Nematic–Smectic-A coexistence (yellow); Smectic-A (green); Smectic-A–Solid coexistence (cyan); Solid (blue).

the plot of order parameter against density, noting no remarkable deviation from a monotonic relationship in the nematic region.

Figure 4.2 shows the structure factor for wavevectors along the director. It can be seen that for the nematic state points, $\tilde{g}(k_z)$ contains relatively broad peaks, visibly containing considerable statistical noise. As we move into the smectic phase, the initial peak value increases by an order of magnitude for the first smectic-A state point, with an increase of another order of magnitude as we make any further change to a higher density system. This signifies, beyond any reasonable doubt, translational order along the director for state points studied with ρ/ρ_{cp} above 0.504. Another noteworthy feature is the presence of larger peak-values for the higher order peaks as the density increases, illustrating a greater degree of short-range order.

The transition from the nematic phase is even more apparent when viewing the function $G(k_3)$ in figure 4.2. Once again, the cumulative function is more than an order of magnitude larger once the nematic state point is surpassed, with further increase of at least an order for any higher density.

As the smectic-A–solid transition is approached, it is informative to view the structure factor for wavevectors normal to the director, $\tilde{g}(k_1)$, as in figure 4.3. For densities below the transition, the spectrum will contain isotropic ringed peaks corresponding to liquid-like order of varying extent. As we enter the solid phase, the low-k ring breaks symmetry into sharper peaks arranged in an approximately hexagonal pattern, the locations of which provide us with lattice vectors. The outer rings also spread out to form peaks, corresponding to shorter range order.

Individual configurations of a system may also be examined, in order to gain insight into the instantaneous ordering of the systems, and some system conformation snapshots are shown in Figures 4.4 and 4.5. In both the nematic and smectic-A phases, when plotting the molecules as spherocylinders, it can be clearly seen that orientational order is present, but it is not obvious from the image as to the extent of any positional order. It can be useful to plot partial regions of the molecules in order to see evidence of phases present [Veerman and Frenkel, 1992]. A cross section at the centre of each spherocylinder can be plotted as a platelet of diameter D, and the screenshot in Figure 4.5 clearly shows layering of the vast majority of molecules, in stark contrast to the nematic configuration in Figure 4.4.

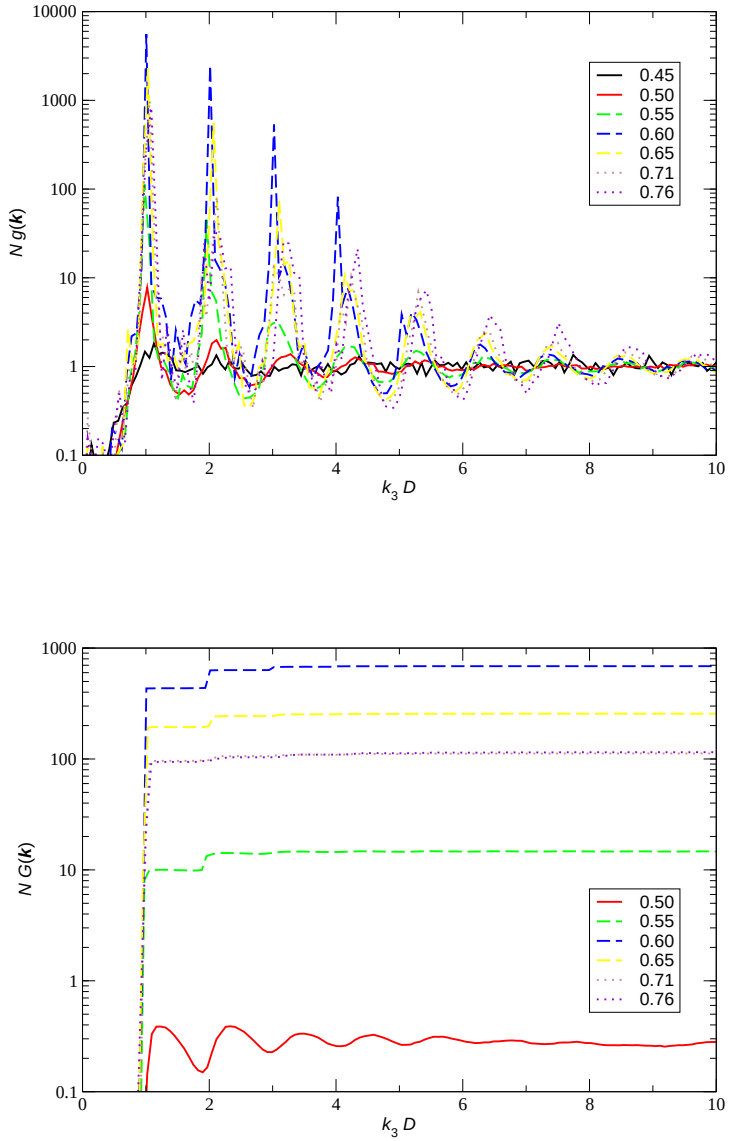

Figure 4.2: The structure factor and its cumulation against wavevector along the director (k_3) for a range of state points. The colour coding gives reduced density $\rho/\rho_{\rm cp}$ for each data set, with the line pattern showing which phase should be exhibited according to [Bolhuis and Frenkel, 1997]. Nematic (solid); Smectic-A (dashed); Solid (dotted).

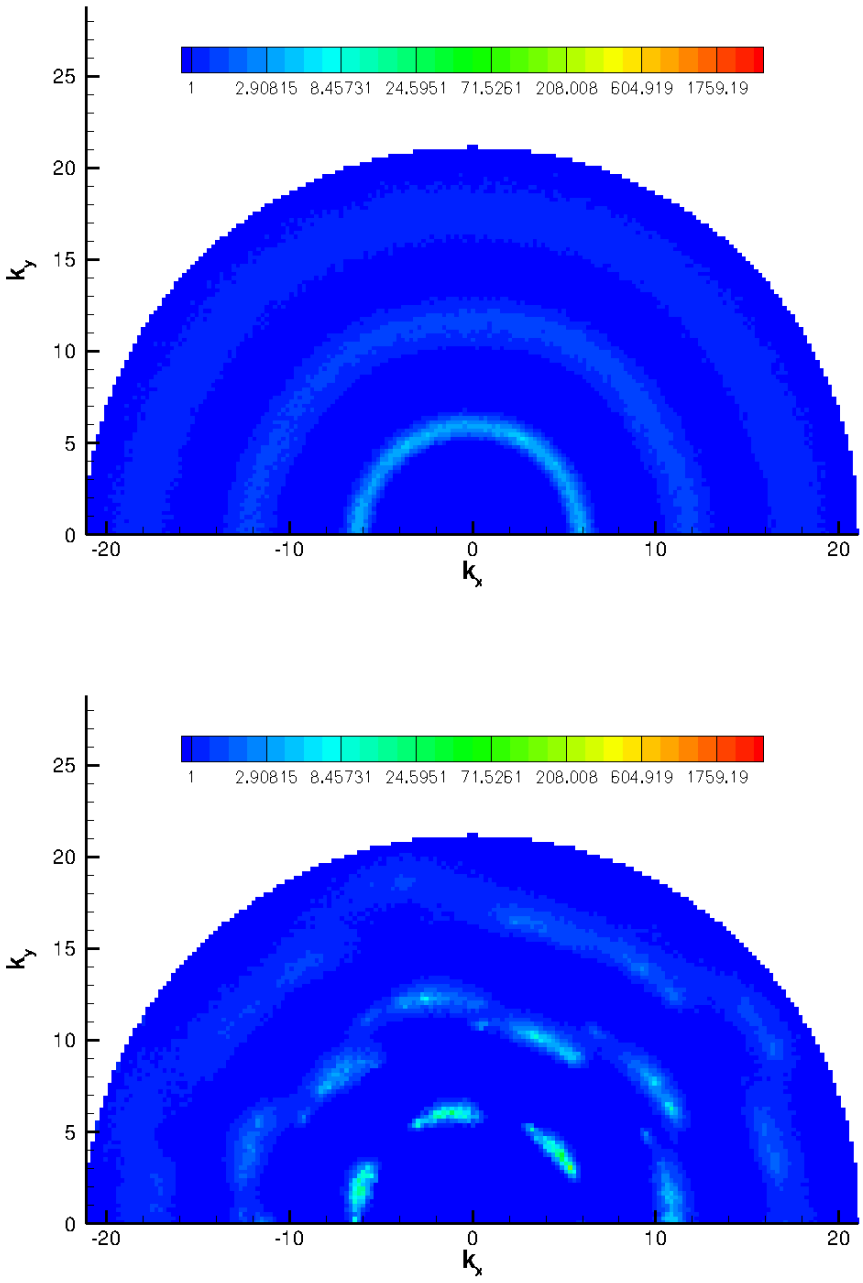

Figure 4.3: The structure factor against wavevector normal to the director (k_1) for $\rho/\rho_{\mathrm{cp}} = 0.65$ (above) and 0.71 (below).

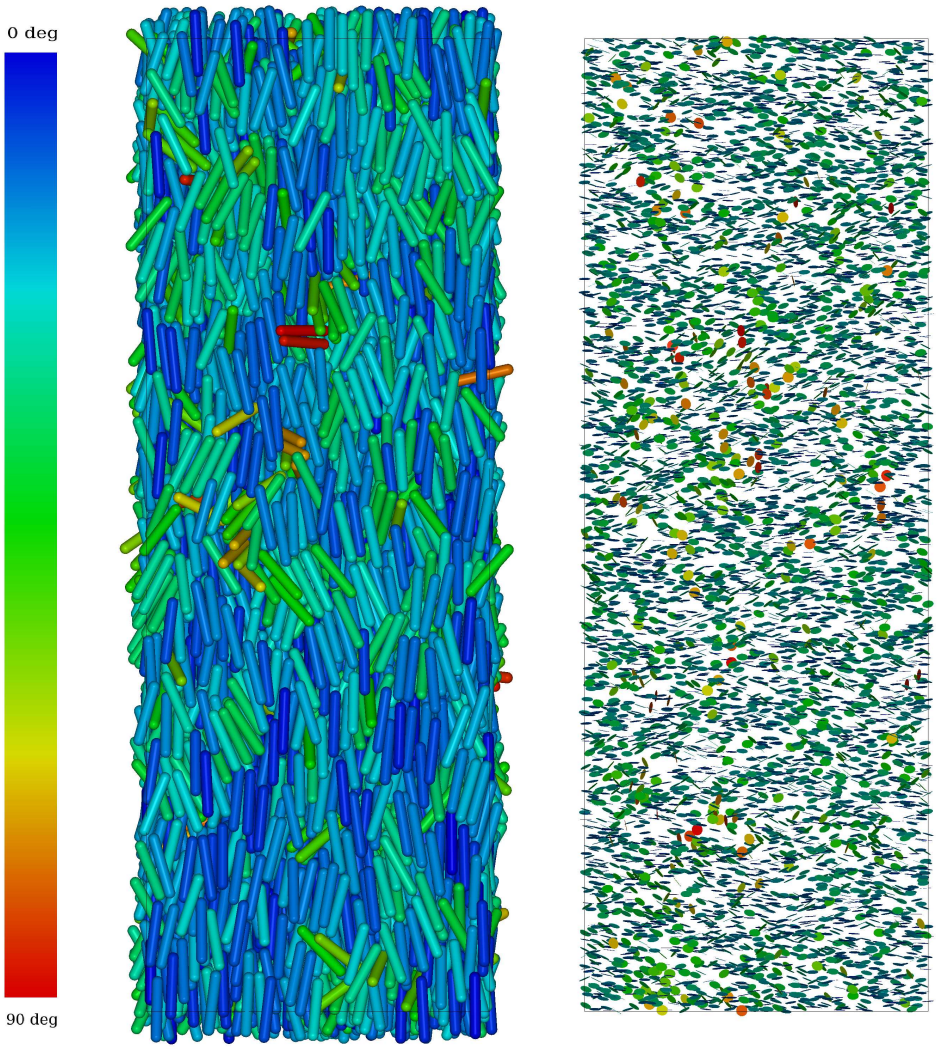

Figure 4.4: Instantaneous configuration of a system of hard spherocylinders for $\rho/\rho_{\mathrm{cp}} = 0.504$. The colour coding colours molecules according to their angle relative to the vertical axis: blue along the axis, red normal to the axis. The molecules are plotted as spherocylinders with length L and diameter D (left image) and platelets of diameter D (right).

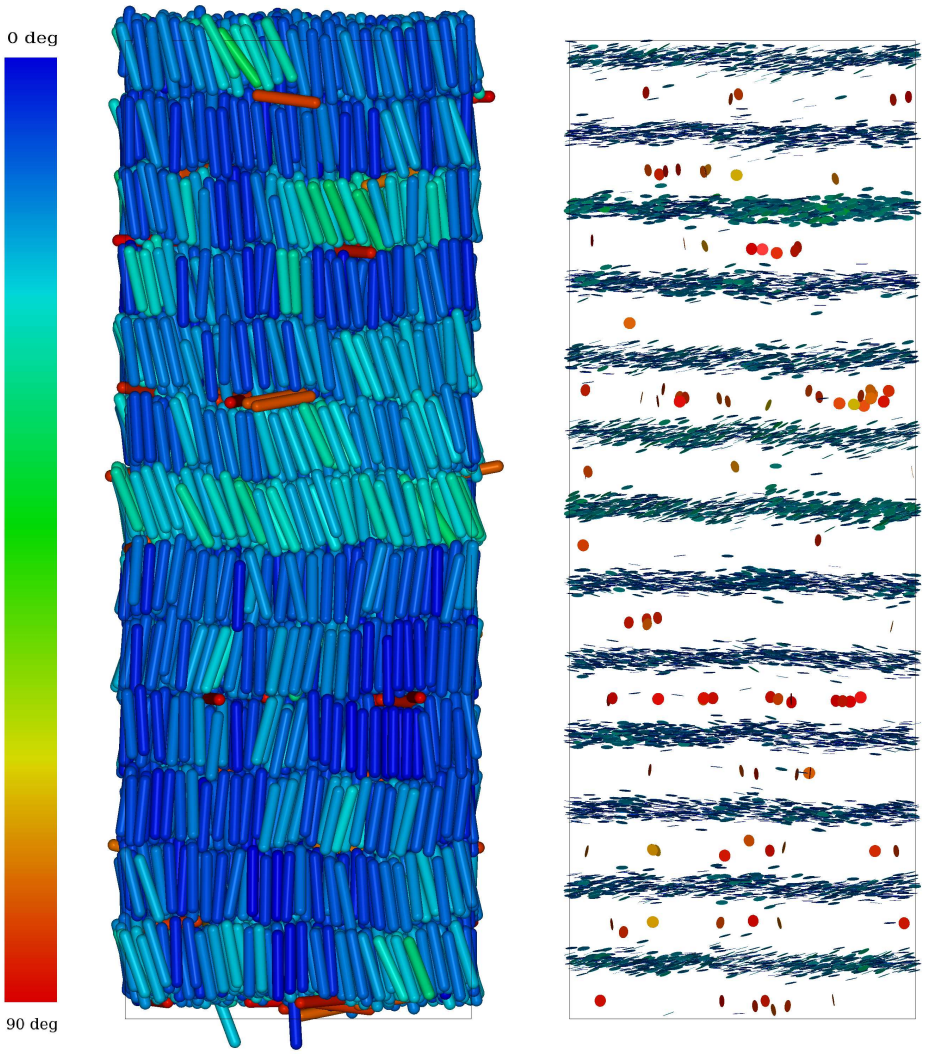

Figure 4.5: Instantaneous configuration of a system of hard spherocylinders for $\rho/\rho_{\mathrm{cp}} = 0.60$. The colour coding colours molecules according to their angle relative to the vertical axis: blue along the axis, red normal to the axis. The molecules are plotted as spherocylinders with length L and diameter D (left image) and platelets of diameter D (right). Note the well defined smectic layers, and a small fraction of transverse interlayer particles.

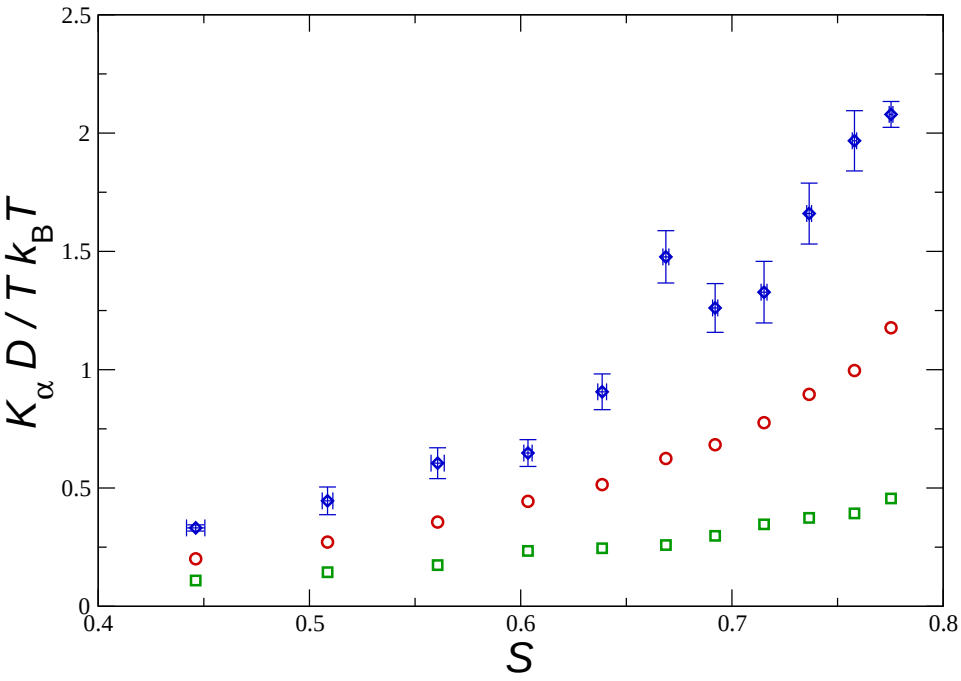

Figure 4.6: The splay, twist and bend elastic constants as a function of order parameter. Splay, K_1, circles (red); twist, K_2, squares (green); bend, K_3, diamonds (blue). The error bars are shown for K_3, whereas, for K_1 and K_2, the errors are smaller than the plotting symbols.

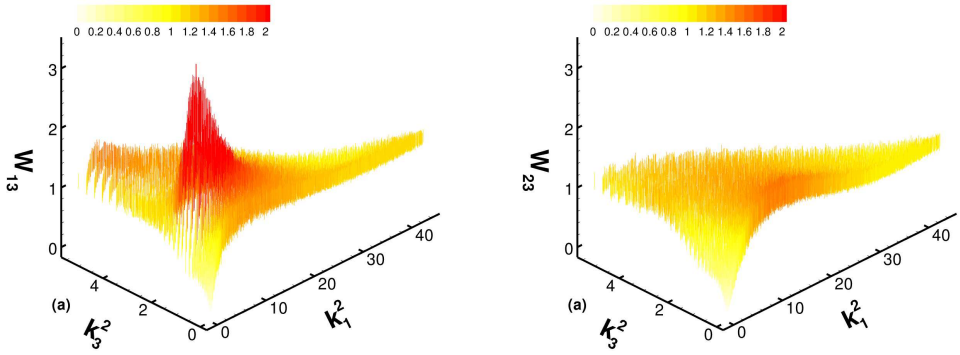

Figure 4.7: The functions $\mathcal{W}_{\alpha 3}$ as a function of wavevector components (k_1^2, k_3^2) at the $\rho/\rho_{\text{cp}} = 0.504$ state point. The simulation data with statistical error is given as a set of vertical lines, with the dotted surface representing the fitting function. The legends show the contour colour coding, with all units such that $L = 5$, $D = 1$ and $k_B T = 1$.

4.2.3 Elastic Constants

Figure 4.7 shows the functions $\mathcal{W}_{\alpha 3}(\boldsymbol{k})$, defined by eqn (3.16). As desired, the fitting functions describe the linear, low-k regime well, mostly passing through the data points within statistical error. The $\mathcal{W}_{\alpha 3}$ are significantly distorted by statistical noise, with some potential structural detail concealed due to the large error bars. $\mathcal{W}_{13}$ follows the structure over a maximum as k_1 and k_3 increase together and $\mathcal{W}_{23}$ describes the smoothing out of a subtly peaked profile in k_1 as k_3 increases.

This behaviour is also illustrated in Figure 4.8, showing various slices of the data sets for $\mathcal{W}_{\alpha 3}(\boldsymbol{k})$. The structure for varying k_3 is more evident here, with the functions developing "kinks" or rising rapidly in the region of $(k_3 D)^2 \approx 1$, corresponding to a correlation distance $\lambda_3 \approx 6.3D$, which is close to the molecular length. It is apparent that the lower splay and twist elastic constants, causing only gradually increasing fluctuations, couple with a lack of structure developing normal to the director (compared to parallel fluctuations) to allow more points to be included in the low-k treatment perpendicular to $\boldsymbol{n}$.

Although the estimates for the elastic constants are sensitive to the range of wavevector spectrum and number of fitting parameters included, there is negligible visible effect on the low-k regions of each graph. Hence, we have plotted the fitting

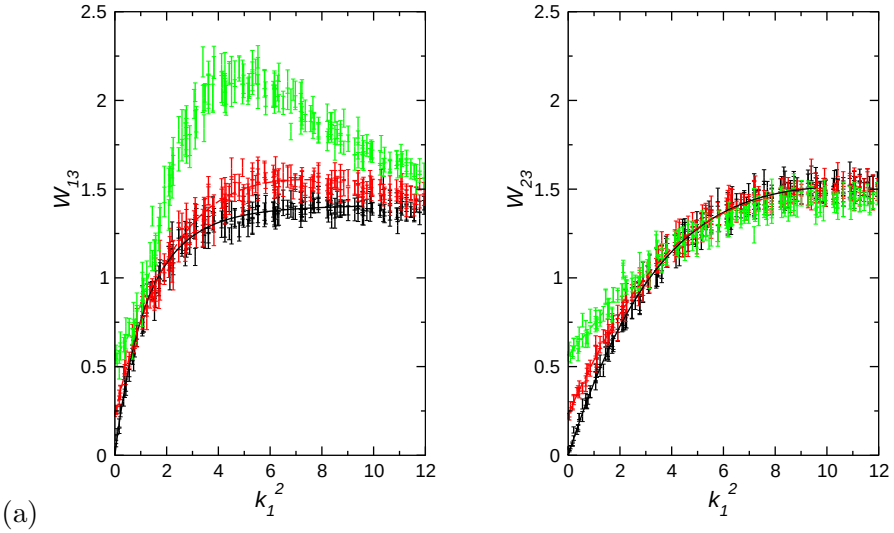

(a)

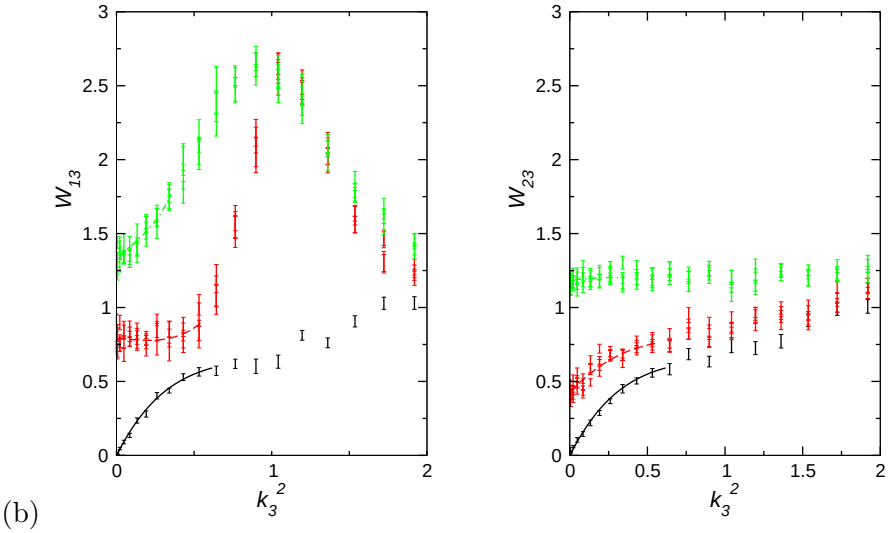

(b)

Figure 4.8: Slices through the $\mathcal{W}_{13}$ (left) and $\mathcal{W}_{23}$ (right) surfaces, from simulations at the $\rho/\rho_{\rm cp} = 0.504$ state point, for **(a)** fixed k_3 as a function of k_1^2, showing respectively splay and twist fluctuations; and **(b)** fixed k_1 as a function of k_3^2, showing bend fluctuations. The error bars give the data points with statistical error and the lines correspond to the fitting function for the highest cutoff in each case. **(a)** $k_3 = 0$, full line (black); $k_3 = 5k_0$, dashed line (red); $k_3 = 10k_0$, dot-dashed line (green). **(b)** $k_1 = 0$, full line (black); $k_1 = 5k_0$, dashed line (red); $k_1 = 10k_0$, dot-dashed line (green). Recall $k_0 = 2\pi/\mathcal{L}$.

function as fitted up to the highest cutoff values of k chosen with the largest number of parameters used, in order to guide the eye over as much of the observed data as possible.

The elastic constants obtained from this fitting procedure are summarized in table 4.1, with figure 4.6 showing the elastic constants as a function of order parameter. The qualitative features of the results are as expected for rod-like particles [Kroger and Ilg, 2007]: $K_2 < K_1 < K_3$. The effect of the significant noise recorded in the fluctuation spectra, along with uncertainty arising from the fitting procedure, can be seen on the elastic constants in the form of minor fluctuation in K_1 and K_2 as order parameter increases, as well as considerably larger error values, fluctuation and an anomalous result (for $\rho/\rho_{\mathrm{cp}} = 0.479$) for K_3.

Figure 4.6 shows bend fluctuations for the state point giving the anomalous value for K_3, as well as the next state point above in density. Upon examination of the spectra, it is apparent that the magnitude of the fluctuations is generally larger in the higher density system; the peaks of $\mathcal{W}_{13}(\boldsymbol{k})$ for $k_1 > 0$ being higher and slightly shifted, and $\mathcal{W}_{23}(\boldsymbol{k})$ being noticably levelling off at greater values. For the higher density, the fitted functions (for $k_1 = 0$) appear roughly linear against k_3 up until around $(k_3 D)^2 = 0.3$, then becoming a curve to fit the data as the higher order terms in k_3^2 become significant. Whereas for the lower density system, the linear relationship dissolves earlier in k_3 as the higher order terms dominate, reducing the function value to fit the rest of the data. This corresponds to a higher value for the leading coefficient, as well as higher values for the higher order coefficients. Hence, despite the higher density data exhibiting generally larger $\mathcal{W}_{\alpha 3}(\boldsymbol{k})$, the leading coefficient (and hence elastic constant) are estimated to be higher for the lower density due to the minimisation procedure yielding a more curved fitting function. This is an unfortunate consequence of fitting to director fluctuation spectra that are heavily affected by statistical noise, as well as structure along k_3, leading to an ability to include only a relatively small number of datapoints in the low-k fitting treatment.

4.3 Platelets

4.3.1 System Details

The simulated system consists of a fluid of infinitely thin hard discs (interaction potential between a pair of molecules $V_{ij} = \infty$ if the molecules overlap, and zero

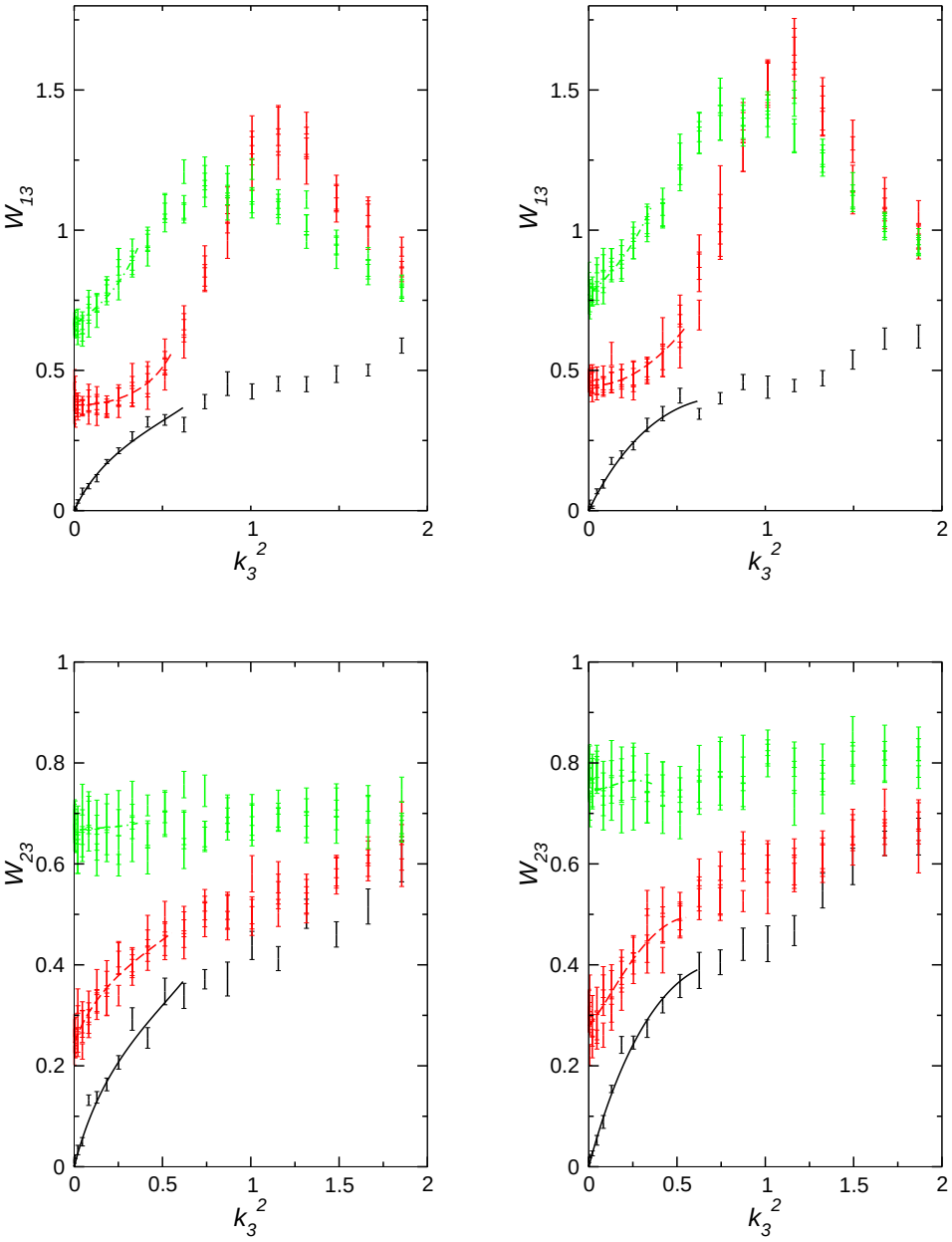

Figure 4.9: Slices through the $\mathcal{W}_{\alpha 3}$ surfaces for fixed k_1 as a function of k_3^2 from simulations at the $\rho/\rho_{\rm cp} = 0.479$ (left) and 0.484 (right) state points, showing bend fluctuations. The error bars give the data points with statistical error and the lines correspond to the fitting function for the highest cutoff in each case. $k_1 = 0$, full line (black); $k_1 = 5k_0$, dashed line (red); $k_1 = 10k_0$, dot-dashed line (green).

ρD^3	S	$K_1 D/k_\mathrm{B}T$	$K_2 D/k_\mathrm{B}T$	$K_3 D/k_\mathrm{B}T$
4.50	0.6694(8)	2.85(4)	4.75(7)	0.86(1)
5.00	0.7620(4)	4.3(3)	7.6(1)	0.98(4)
6.00	0.8490(2)	9.80(5)	15.2(1)	1.31(3)
6.25	0.8618(3)	11.4(1)	17.4(1)	1.43(4)
6.50	0.8738(3)	13.4(1)	20.6(3)	1.63(4)
6.75	0.8827(3)	14.9(1)	22.8(1)	1.56(9)
7.00	0.8922(2)	17.4(3)	26.2(4)	1.59(1)
7.25	0.9003(3)	19.3(2)	28.9(2)	1.75(6)
7.50	0.9065(2)	21.5(1)	32.8(3)	1.76(4)
7.75	0.9130(2)	24.2(1)	36.1(5)	1.80(3)
8.00	0.9180(3)	26.7(3)	40.5(2)	1.89(5)

Table 4.2: Density ρD^3 of each simulation, with simulation averages of order parameter S, and elastic constants $K_\alpha D/k_\mathrm{B}T$. Figures in parentheses represent estimated errors in the last quoted digit.

otherwise). The overlap criterion is described elsewhere [Eppenga and Frenkel, 1984; Allen et al., 1993]. For this system, due to the absence of any finite interaction potentials, the temperature is irrelevant, except as a scaling factor for energies and free energies. Reduced units of energy in these simulations are obtained by taking $k_\mathrm{B}T = 1$ and reduced units of distance by setting the platelet diameter $D = 1$.

Monte Carlo simulations were performed for systems of 8000 particles with cubic periodic boundary conditions in the canonical ensemble. Equilibration runs consisted of at least 10^5 sweeps, and simulation averages were taken during production runs of 1 or 2×10^6 sweeps, depending on density (1 sweep = 1 attempted MC move, combined translation and rotation, per particle). Displacement parameters were chosen to give a move acceptance rate in the range 30–40%.

As the limit of infinitely thin platelets is approached, the volume occupied by each molecule, and hence the packing fraction η, are vanishingly small, with the close-packed density becoming divergently large. Therefore it is conventional to express densities in terms of the only nonvanishing unit of distance, the platelet diameter D, as ρD^3. All of the state points chosen, densities ranging $\rho D^3 = 4.5$ – 8, lie in the nematic region for platelets; the isotropic-nematic transition occurs at $\rho D^3 \approx 3.78$ [Eppenga and Frenkel, 1984; Bates, 1999]. Average values of order parameter for each density are reported in Table 4.2.

The calculation of director fluctuation spectra was performed every 10^2 MC sweeps. In the calculation of director fluctuation spectra, it was desirable for the

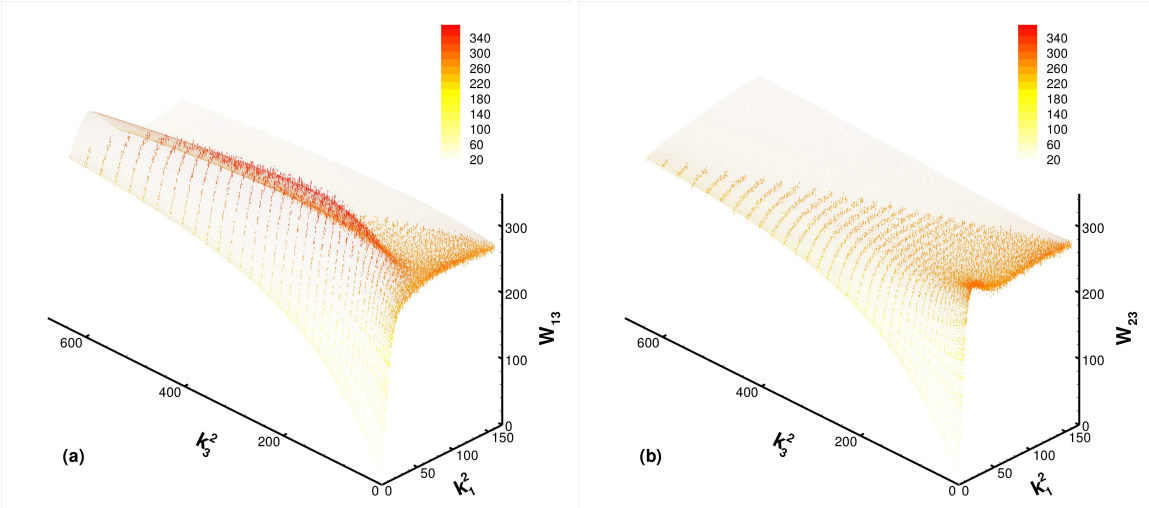

Figure 4.10: The functions $\mathcal{W}_{\alpha 3}$ as a function of wavevector components (k_1^2, k_3^2) for platelets at the $\rho D^3 = 8$ state point. The simulation data with statistical error is given as a set of vertical lines, with the dotted surface representing the fitting function. The legends show the contour colour coding, with all units such that $D = 1$ and $k_B T = 1$.

limiting values on the wavevector spectrum to be large enough to observe the high-k behaviour of the functions $W_{\alpha 3}(\boldsymbol{k})$, and hence the maximum values were chosen to be $0 \leq \kappa_{x,y} \leq 20$ and $0 \leq \kappa_z \leq 40$. Due to a lack of positional ordering, the structure in the spectra for platelets is relatively featureless, allowing one to choose higher cutoffs in the fitting. Hence we were able to set the upper bounds for $k_1 \mathcal{L}/2\pi$ to 6, 8 and 10, and for $k_1 \mathcal{L}/2\pi$ we chose 12, 16 and 20.

4.3.2 Phase Behaviour

Platelets exhibit two phases, isotropic at low densities, with a transition to nematic (at $\rho D^3 \approx 4$) upon increasing density. They are unable to crystallise due to their lack of particle volume, and thus no translationally ordered phases are formed [Frenkel and Eppenga, 1982]. In the asymptotic limit of high orientational order parameter, the angle-averaged second virial coefficient (and higher virial coefficients) vanish as no overlaps may occur [Eppenga and Frenkel, 1984], reducing the positional order to that of the ideal gas.

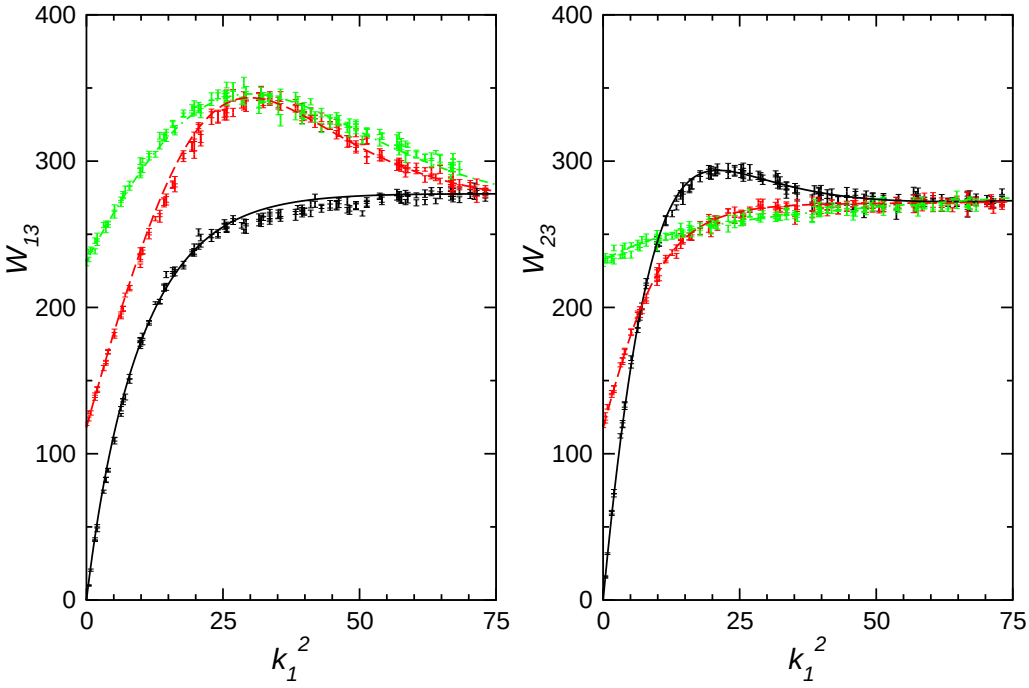

Figure 4.11: Slices through the $\mathcal{W}_{13}$ (left) and $\mathcal{W}_{23}$ (right) surfaces for platelets at fixed k_3 as a function of k_1^2, showing respectively splay and twist fluctuations, from simulations at the $\rho D^3 = 8$ state point. The error bars give the data points with statistical error and the lines correspond to the fitting function for the entire surface in each case. $k_3 = 0$, full line (black); $k_3 = 15k_0$, dashed line (red); $k_3 = 30k_0$, dot-dashed line (green).

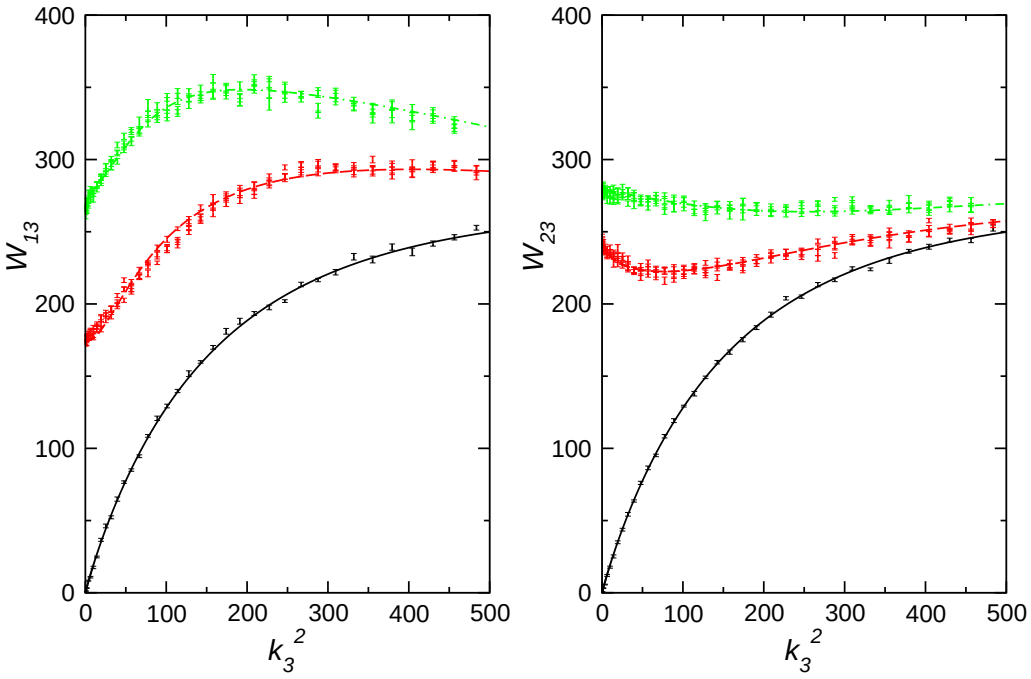

Figure 4.12: Slices through the $\mathcal{W}_{13}$ (upper) and $\mathcal{W}_{23}$ (lower) surfaces for platelets at fixed k_1 as a function of k_3^2, showing bend fluctuations, from simulations at the $\rho D^3 = 8$ state point. The error bars give the data points with statistical error and the lines correspond to the fitting function for the entire surface in each case. $k_1 = 0$, full line (black); $k_1 = 5k_0$, dashed line (red); $k_1 = 10k_0$, dot-dashed line (green).

4.3.3 Elastic Constants

Figure 4.10 shows the functions $\mathcal{W}_{\alpha 3}(\boldsymbol{k})$, defined by eqn (3.16). As desired, the fitting functions describe the linear, low-k regime well, and even pass through most of the data points for higher-k. $\mathcal{W}_{13}$ follows the structure over a maximum as k_1 and k_3 increase together and $\mathcal{W}_{23}$ describes the smoothing out of a sharply peaked profile in k_1 as k_3 increases. It is apparent that the low bend elastic constant, causing only gradually increasing fluctuations, couples with a lack of structure developing along the director (compared to normal fluctuations) to allow more points to be included in the low-k treatment along $\boldsymbol{n}$.

This behaviour is also illustrated in Figures 4.11,4.12, showing various slices of the data sets for $\mathcal{W}_{\alpha 3}(\boldsymbol{k})$. Although the estimates for the elastic constants are sensitive to the range of wavevector spectrum and number of fitting parameters included, there is no visible effect on the low-k regions of each graph. Hence, we have plotted the fitting function as fitted across the entire spectrum with the largest number of parameters used, in order to guide the eye over the observed data.

The elastic constants obtained from this fitting procedure are summarized in Table 4.2. Figure 4.13 shows the elastic constants as a function of order parameter as obtained from the simulation and theory. The qualitative features of the results are as expected for disc-like particles [Kroger and Ilg, 2007]: director twist induces the largest free energy penalty, bend is the least expensive and splay lies between the others. A striking result is that the bend elastic constant K_3 is very small compared with the others (by more than an order of magnitude for the more ordered state points); this highlights the anisotropy of the infinitely thin platelets.

It is of interest to compare these results with experimental determinations of the elastic constants for colloidal suspensions of gibbsite particles [van der Beek et al., 2008; Verhoeff et al., 2009]: $K_1 = 0.6$–2.6×10^{-13} N and $K_3 = 6$–8×10^{-14} N for an order parameter in the range $S \approx 0.80$–0.85. If one inserts estimates for $D \approx 220$nm and $k_{\mathrm{B}}T \approx 4\times10^{-21}$, the corresponding simulation results for $S \approx 0.85$ are $K_1 \approx 1.8\times10^{-13}$ N and $K_3 \approx 2.4\times10^{-14}$ N. This is quite reasonable agreement, bearing in mind that the experimental platelets are not of vanishing thickness.

Figure 4.13 compares results from virial expansion theory [O'Brien et al., 2008] with simulation data, showing reasonable agreement. Figure 4.14 shows the convergence of the virial series for the splay constant K_1. As can be seen, truncating at the second-order virial level drastically underestimates the elastic constant.

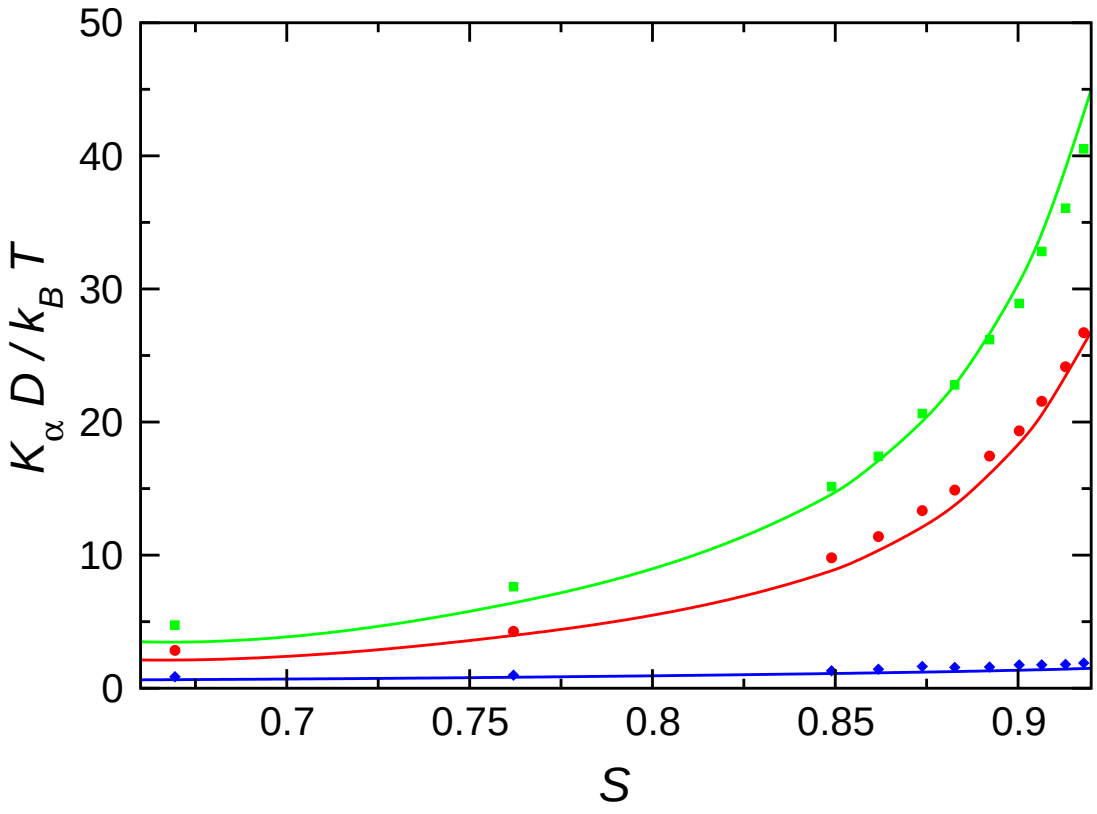

Figure 4.13: The splay, twist and bend elastic constants for hard platelets as a function of order parameter. The lines represent data from a sixth order virial expansion, and the points are simulation results. Splay, K_1, circles (red); twist, K_2, squares (green); bend, K_3, diamonds (blue). In all cases the errors are smaller than the plotting symbols.

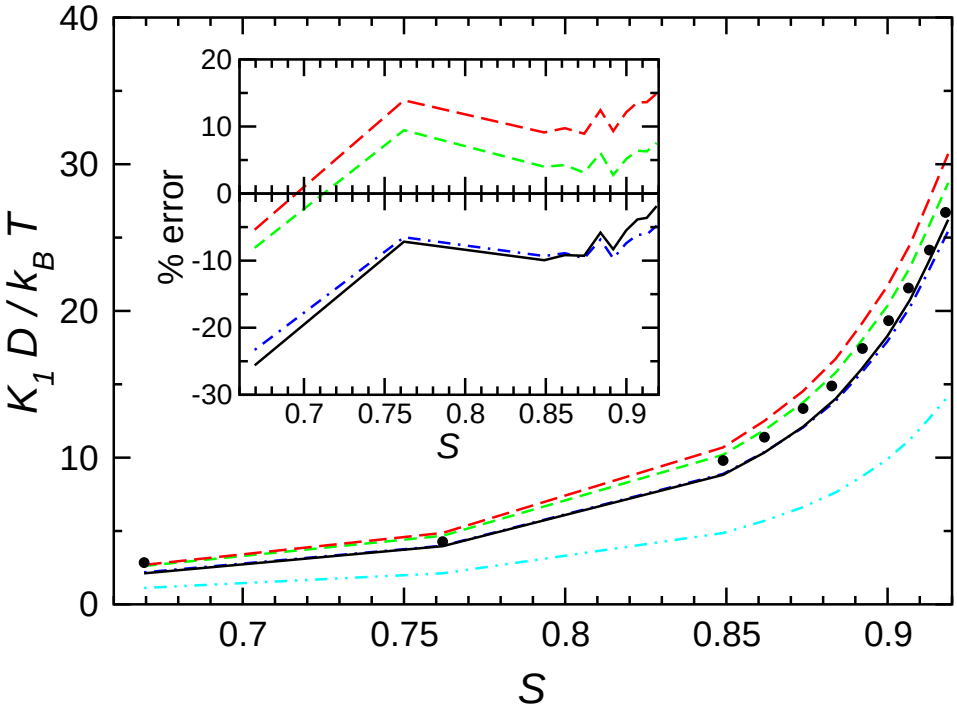

Figure 4.14: Splay elastic constant K_1 for hard platelets as a function of order parameter S. The black circles give results from Monte Carlo simulation, the lines give data from various orders of virial expansion. 6^{th}-order, continuous (black); 5^{th}-order, long dashed (red); 4^{th}-order, short dashed (green); 3^{rd}-order, dot-dashed (blue); 2^{nd}-order, double-dot-dashed (cyan). Inset: percentage error in the 3^{rd}–6^{th}-order theories, using the same notation

However, at third-order, the agreement with simulation is much better, although it is still an underestimate. Apart from the lowest density, which is not far from the isotropic-nematic transition region, these higher-order virial theories all agree with the simulation results to within ±10%. However, as the order of the virial expansion goes up, the results begin to oscillate around the correct value. The third-order results are underestimates; the fourth-order results are slight overestimates, fifth-order is a greater overestimate, while the sixth-order results are underestimates, barely distinguishable from the results obtained at third-order. This is due to the appearance of negative coefficients in the theory at this order. Similar convergence properties are seen for K_2 and K_3, with second-order virial theory significantly underestimating the elastic constant, and subsequent orders getting closer to the true value, until the change in sign of the virial coefficients causes fluctuation around the simulation result.

4.4 Cut-Spheres

4.4.1 System Details

The simulated systems consist of a fluid of identical hard cut-spheres (interaction potential between a pair of molecules $V_{ij} = \infty$ if the molecules overlap, and zero otherwise), with diameter D, varying thickness (distance between the circular end faces) L, and L/D taking the value 1/20, 1/15 or 1/10. The overlap criterion is described elsewhere [Allen et al., 1993]. For this system, due to the absence of any finite interaction potentials, the temperature is irrelevant, except as a scaling factor for energies and free energies. Reduced units of energy in these simulations are obtained by taking $k_{\mathrm{B}}T = 1$ and reduced units of distance by setting the platelet diameter $D = 1$.

Monte Carlo simulations were performed for systems of 8000 particles with cubic periodic boundary conditions in the canonical ensemble. Equilibration runs consisted of at least 10^5 sweeps, and simulation averages were taken during production runs of 3×10^6 sweeps (1 sweep = 1 attempted MC move, combined translation and rotation, per particle). Displacement parameters were chosen to give a move acceptance rate in the range 30–40%.

The close-packed density of a system of cut-spheres is given by

$$\rho_{\mathrm{cp}} D^3 = \frac{2(D/L)}{[3-(L/D)^2]^{1/2}} \ . \tag{4.12}$$

As well as relative to the close-packed case, it is also convenient to express densities in terms of the molecular diameter, as ρD^3, for comparison with systems of infinitely thin platelets.

While the complete phase behaviour of cut-spheres at thicknesses between zero and $D/10$ has not been thoroughly categorised in the published literature, the isotropic–nematic transition has been found to begin at $\rho D^3 \approx 3.9$ and end at 4.1 [Fartaria and Sweatman, 2009] for cut-spheres with $L/D = 1/20$ and $1/15$. This corresponds to $\rho/\rho_{\mathrm{cp}} = 0.22 - 0.23$ and $0.17 - 0.18$ for $L/D = 1/15$ and $1/20$ respectively. According to Duncan et al. [2009], for $L/D = 1/10$, the isotropic-nematic transition occurs in the range $\rho/\rho_{\mathrm{cp}} \approx 0.351$ to 0.371, or $\rho D^3 \approx 4.1$ to 4.3; the nematic–columnar transition begins at $\rho/\rho_{\mathrm{cp}} \approx 0.44$ or $\rho D^3 \approx 5.1$.

The external field may induce subtle changes in the phase behaviour of the systems of cut-spheres, hence the system at each state point must be analysed carefully to determine whether the observed phase agrees with the literature. Perfectly aligned cut-spheres exhibit a smectic phase [Azzouz et al., 1992], which illustrates the susceptibility to perturbation of the phase behaviour of cut-spheres under the influence of an orienting field. Average values of order parameter for each density are reported in Tables 4.3, 4.4, 4.5. Of the state points chosen, those ranging $\rho D^3 = 4$ – 8 were found to lie in the nematic region for $L/D = 1/20$; as do those with $\rho D^3 = 4$ – 7.5 for $L/D = 1/15$; and $\rho D^3 = 4$ – 5.2 for $L/D = 1/10$.

As for our systems of hard spherocylinders (see section 4.2.1), the initial configurations were set up on a cuboidal lattice, and the box lengths scaled to yield the desired density under study, before equilibration runs were performed. As for our systems of hard spherocylinders, the fixed simulation box lengths, along with the fixed director close to $\hat{\boldsymbol{z}}$, mean that our results for the columnar phase will have to be viewed in the context of a frustrated, unrepresentative system.

The calculation of director fluctuation spectra was performed every 10^2 MC sweeps, with configurations for the structure factor recorded every 10^3 sweeps. In the calculation of director fluctuation spectra, it was desirable for the limiting values on the wavevector spectrum to be large enough to observe the high-k behaviour of the functions $W_{\alpha 3}(\boldsymbol{k})$, and hence the maximum values were chosen to be $0 \leq \kappa_{x,y} \leq 20$

and $0 \leq \kappa_z \leq 40$.

The onset of columnar order causes structure to develop along the **1**-direction in the region of $k_1 D/2\pi = 1$, with the diameter of a molecule D being a reasonable first approximation for an intercolumn spacing. Due to these pre-transitional effects, in the fitting of $W_{\alpha 3}$, only data points for k_1 up to some maximum value below $2\pi/D$ are included in each fitting procedure. The three different limiting values in the fitting process for $2\pi/k_1 D$ were 1.5, 1.65 and 1.8. With the onset of crystalline order, a correlation distance in the **3**-direction of the order of L will induce structure in the $W_{\alpha 3}$. This, however, is not approached whilst still in the nematic phase, meaning that it was sufficient to set the bounds in the fitting for $2\pi/k_3 D$ to 0.6, 0.52 and 0.45.

Another consequence of translational ordering is the splay and twist elastic constants being predicted to diverge at the nematic-columnar transition [Swift and Andereck, 1982], which can be understood on geometrical grounds as the correlation length for columnar order grows. As for any positionally ordered phases, there will also be non-zero values for compression moduli, or translational elastic constants, in the directions of the ordering (the intercolumnar vectors in this case).

4.4.2 Phase Behaviour

The phase behaviour of cut-spheres with $L/D = 1/10$ has been thoroughly documented [Frenkel, 1989; Veerman and Frenkel, 1992; Duncan et al., 2009], with the absence of any external field, and data for the eighteen state points studied is plotted in Figure 4.15 with coloured regions showing the expected phase behaviour. There is no obvious structure in the order parameter against density, hence it is necessary to examine other properties of the system more closely to determine the phases truly present.

Plots of the structure factor normal to the director must be examined to check for positional order. Even at the highest densities studied here, only liquid-like ordering was observed when plotting $\tilde{g}(k_z)$, leaving our systems considerably far from the solid phase. Therefore, to categorise the columnar phase, only $\tilde{g}(k_x, k_y)$ need be illustrated here. In the nematic phase, $\tilde{g}(k_x, k_y)$ should possess a cylindrically symmetrical ring-shaped main peak of finite height due to liquid-like positional order. As density increases, regions exhibiting columnar order arise, breaking the cylindrical symmetry of the ring into individual peaks of greater height. Shorter-ranged order is represented as the higher order rings break symmetry and intensify. Well

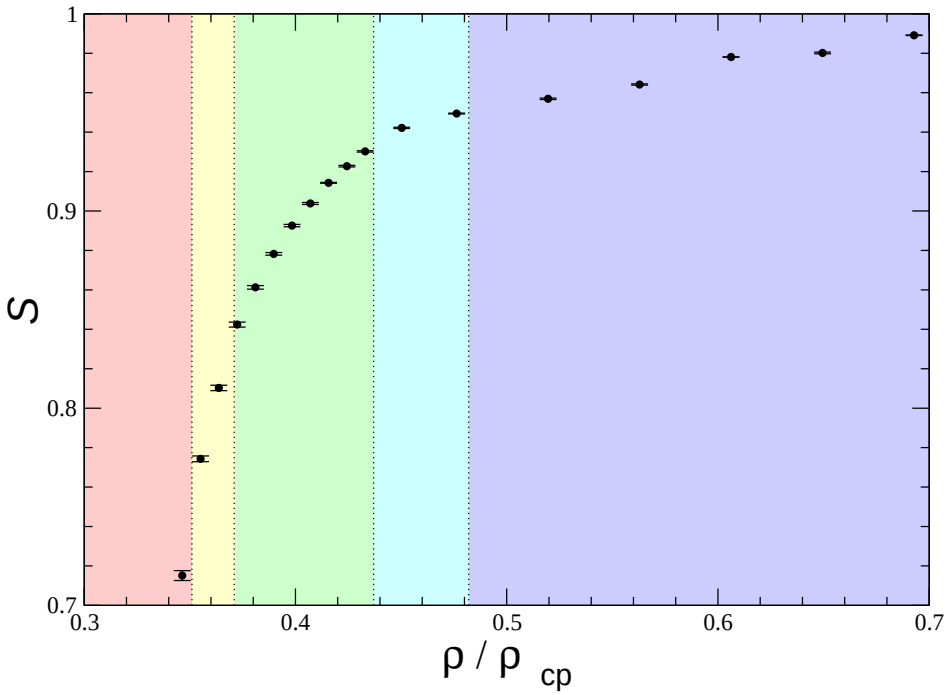

Figure 4.15: The nematic order parameter against density as observed in our systems of cut-spheres, with $L/D = 1/10$. According to Veerman and Frenkel [1992] and Duncan et al. [2009], the state points observed should be situated across three (sometimes coexisting) phases, shown by colour coded regions; Isotropic (red); Isotropic–Nematic coexistence (yellow); Nematic (green); Nematic–Columnar coexistence (cyan); Columnar (blue).

defined columnar order on a single lattice will produce peaks of of order N [Azzouz et al., 1992].

For $L/D = 1/20$, it would appear that the state points sampled were insufficiently dense to induce any columnar ordering, the structure factor spectra being accordingly without structure. Figure 4.16 shows the behaviour of $\tilde{g}(k_x, k_y)$ for $L/D = 1/15$ as density is increased sufficiently to induce columnar order, yielding a roughly hexagonal pattern, suggesting order on a hexagonal lattice. The first-order main peaks are close to $k_1 D/2\pi = 1$, indicating a correlation distance $\lambda_1 \approx D$, which seems a reasonable first approximation for the intercolumnar distance.

Configuration snapshots for the corresponding $L/D = 1/15$ systems are contained in Figures 4.17, 4.18. When viewed as cut-spheres, it is difficult to distinguish between the nematic and columnar phases, as while the orientational order is immediately apparent in both cases, the extent of positional order in certain regions cannot be deduced as it may appear to contain columns with molecules widely dispersed normal to the directional vector. When viewed as a system of rods with length L, however, the positional order in Figure 4.18 becomes noticable along a portion of the simulation box, with the remainder of the fluid in the nematic phase. This indicates that this state point is likely to have entered the nematic–columnar coexistence region. The lattice vectors for the columnar region are present in the structure factor as the locations of the first-order peaks, with higher-order peaks corresponding to shorter-range order.

The density variation of $\tilde{g}(k_x, k_y)$ for $L/D = 10$ is shown in Figure 4.19. It can be seen that between $\rho D^3 = 5.2$ and 5.5 the system undergoes a nematic–columnar transition, and the structure factor spectra of the different state points in the columnar phase correspond to some different lattices. Upon inspection of the corresponding configuration snapshots, contained in Figures 4.20, 4.21, 4.22, 4.23, it is evident that there are a number of different columnar lattices in the systems, each with a contribution to the structure factor spectrum depending on the number of molecules encompassed within the region.

For $\rho D^3 = 5.5$, the conformation shows two lattices oriented $\sim 30^\circ$ to one another about the vertical axis. This produces a structure factor spectrum that has its more intense peaks in a hexagonal pattern, corresponding to the lattice vectors of the larger region, with another set of less intense peaks spread across another hexagonal pattern, whose lattice vectors lie an angle of $\sim 30^\circ$ from those of the aforementioned region. Similarly, for $\rho D^3 = 6$, there are two regions with lattices

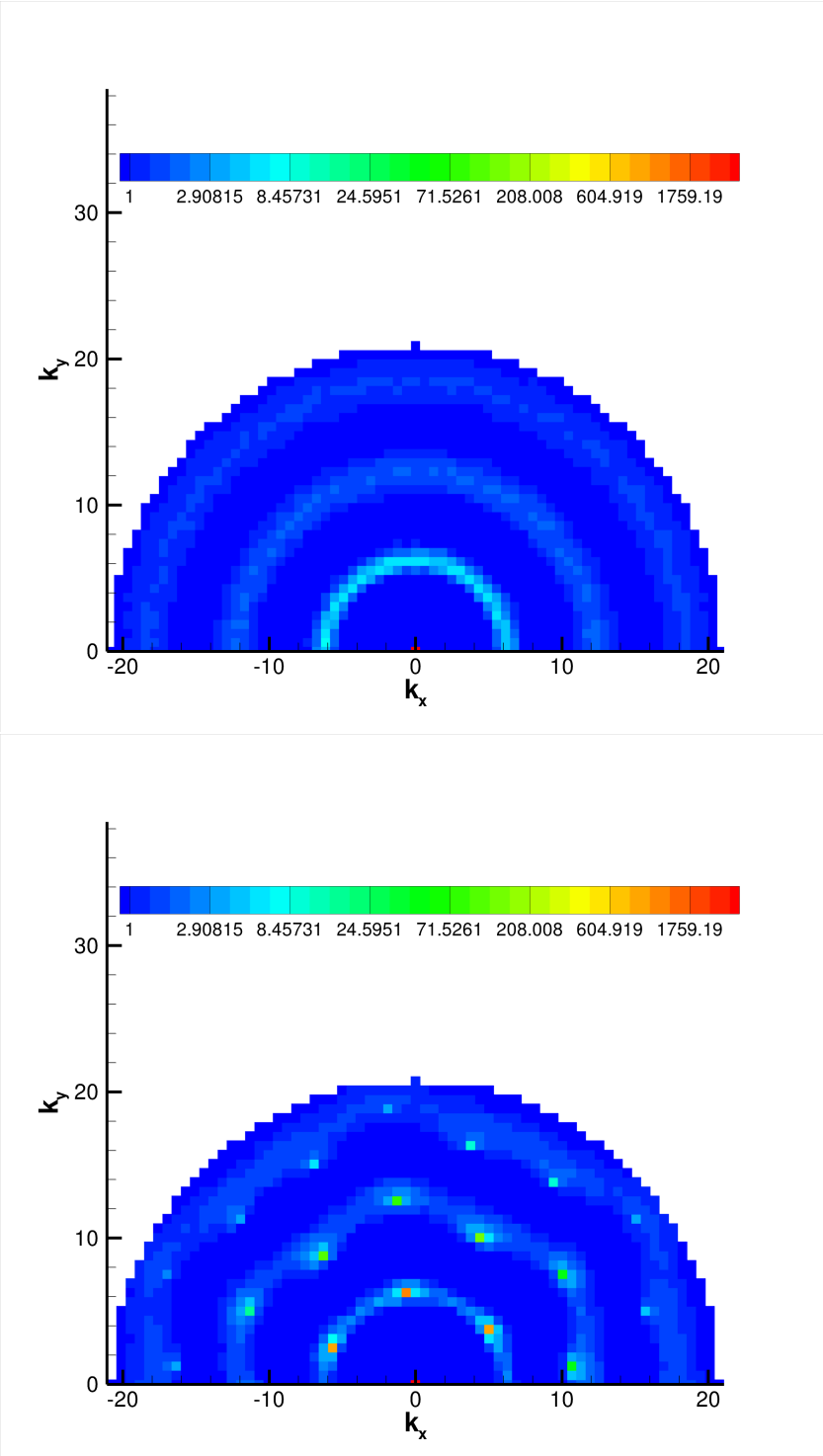

Figure 4.16: The structure factor of cut-spheres, $L/D = 1/15$, against wavevector normal to the director (k_1) for $\rho D^3 = 7.5$ (above) and 8.0 (below).

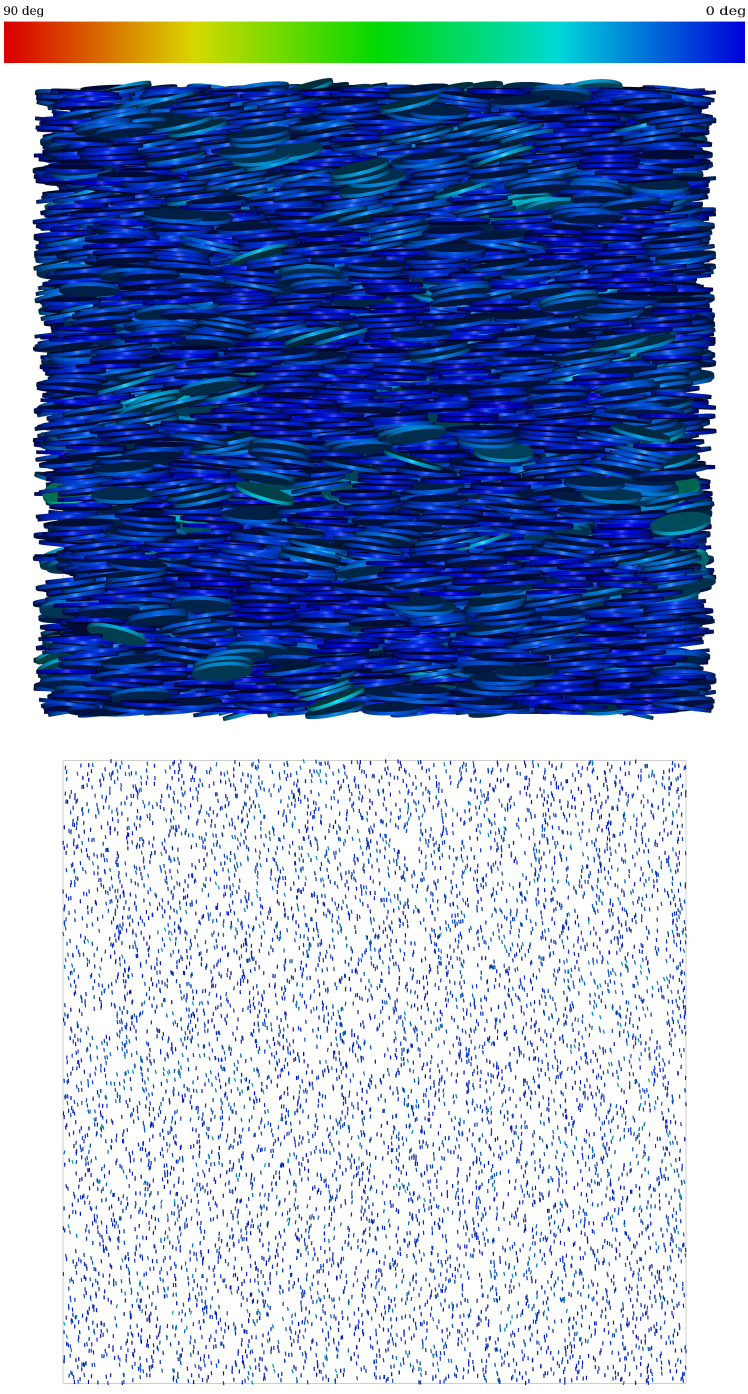

Figure 4.17: Instantaneous configuration of a system of hard cut-spheres, $L/D = 1/15$, for $\rho D^3 = 7.5$. The colour coding colours molecules according to their angle relative to the vertical axis: blue along the axis, red normal to the axis. The molecules are plotted as cut-spheres with diameter D and thickness L (upper image) and rods of length L (lower).

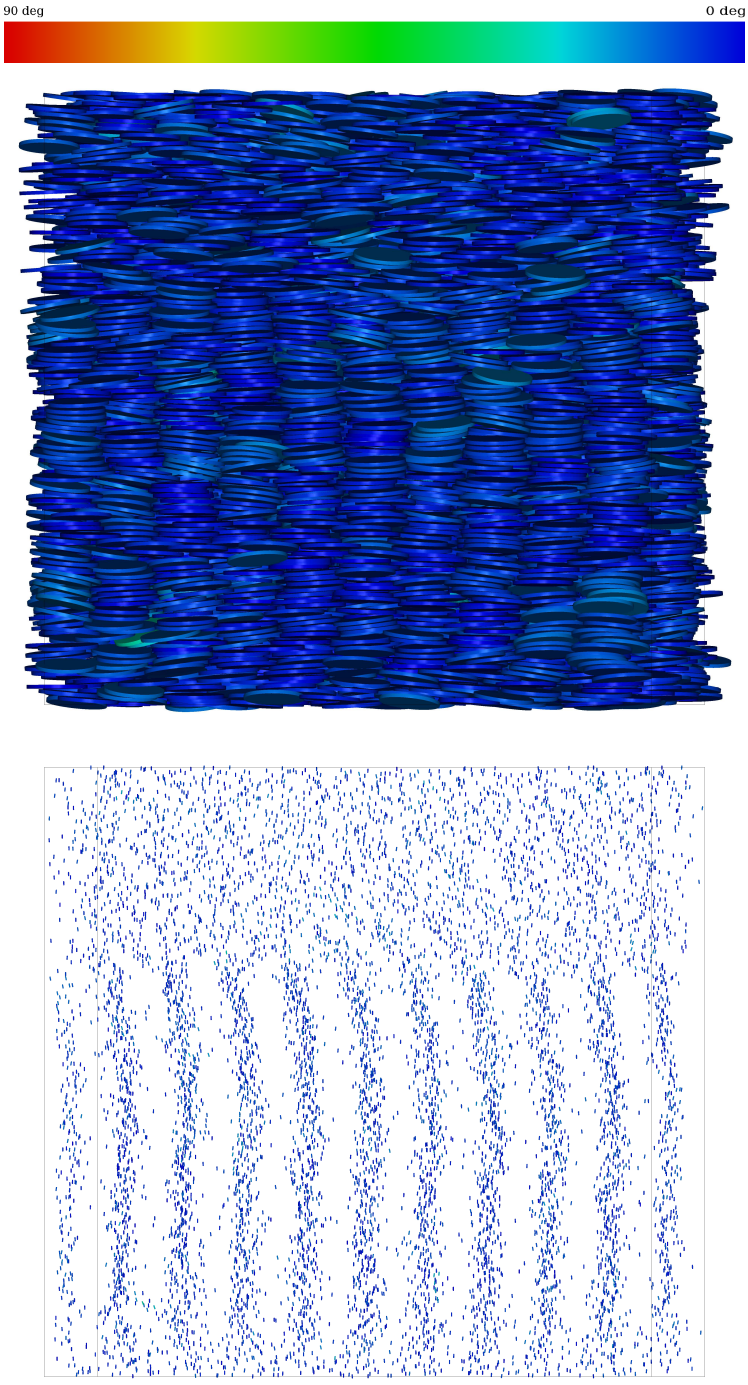

Figure 4.18: Instantaneous configuration of a system of hard cut-spheres, $L/D = 1/15$, for $\rho D^3 = 8$. The colour coding colours molecules according to their angle relative to the vertical axis: blue along the axis, red normal to the axis. The molecules are plotted as cut-spheres with diameter D and thickness L (upper image) and rods of length L (lower).

that differ by an angle of only $\sim 7^\circ$, hence $\tilde{g}(k_x, k_y)$ contains dominant peaks at lattice vectors close to a single hexagonal lattice, with small additional peaks in a nearby hexagonal pattern differing by angle of $\sim 7^\circ$ about the z-axis.

After increasing density beyond $\rho D^3 = 6$, more regions develop in the system with different columnar lattices, leading to structure factor spectra like that for $\rho = 8$, where there are a number of main peaks on the first order ring at locations corresponding to the different lattice vectors. There are also more higher order peaks, due to the short range order in the 1-direction between molecules on different lattices.

It is not obvious as to why there are more regions with different columnar lattices for increasing density, but this does suggest that the lattice free energy of ordering within such regions becomes far more significant than the distortion free energy of the interfaces between additional lattices. This could be due to strong dependencies on the angular distribution, as evidenced by the jump in order parameter from $\rho = 6.5$ to 7 in Figure 4.15.

Although the phase behaviour of these cut-spheres is interesting, we are most concerned with the nematic phase, for which the elastic constants may be examined.

4.4.3 Elastic Constants

The elastic constants obtained from the fitting procedure are summarized in Tables 4.3, 4.4, 4.5, with Figures 4.30, 4.34, 4.38 showing the elastic constants as a function of order parameter. The qualitative features of the results are again as expected for disc-like particles [Kroger and Ilg, 2007]: director twist induces the largest free energy penalty, bend is the least expensive and splay lies between the others. As for the platelets, the bend elastic constant K_3 is significantly smaller than the others, however the ratio increases with L/D, highlighting the reducing anisotropy of the cut-spheres. The large K_1 and K_2 generally decrease, and K_3 generally increases, with increasing thickness. These results are also in fair agreement with the results for tactoids in the work of van der Beek et al. [2008]; Verhoeff et al. [2009] (see section 4.3).

The data for each thickness of disk-like molecule are also shown together for each elastic constant in Figures 4.24, 4.25, 4.26. The layout of the data sets is encouraging; the large K_1 and K_2 generally reduce and K_3 generally increases for the thicker molecules, as the shape anisotropy decreases; and the plots against order parameter seem disparate enough to form a continuum of behaviour for varying

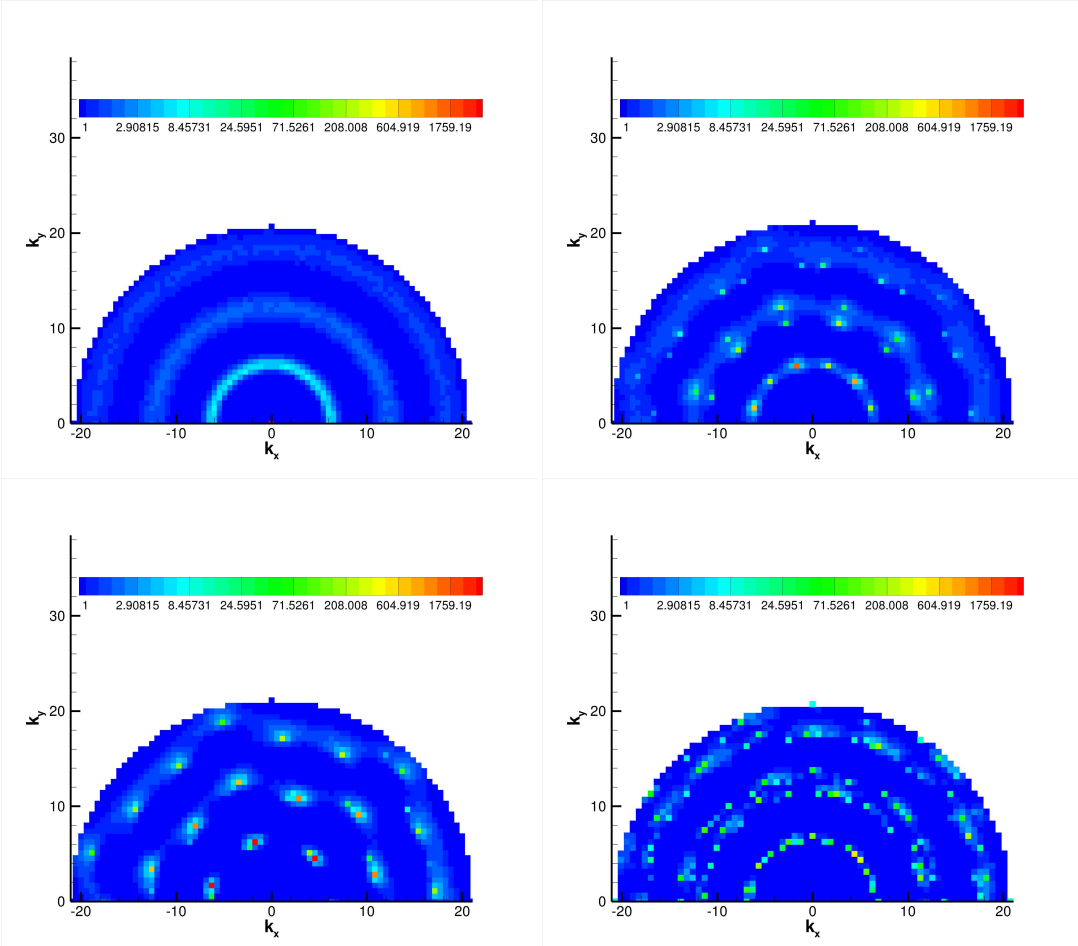

Figure 4.19: The structure factor of cut-spheres, $L/D = 1/10$, against wavevector normal to the director (k_1) for $\rho D^3 = 5.2$ (above left), 5.5 (above right), 6.0 (below left) and 8.0 (below right).

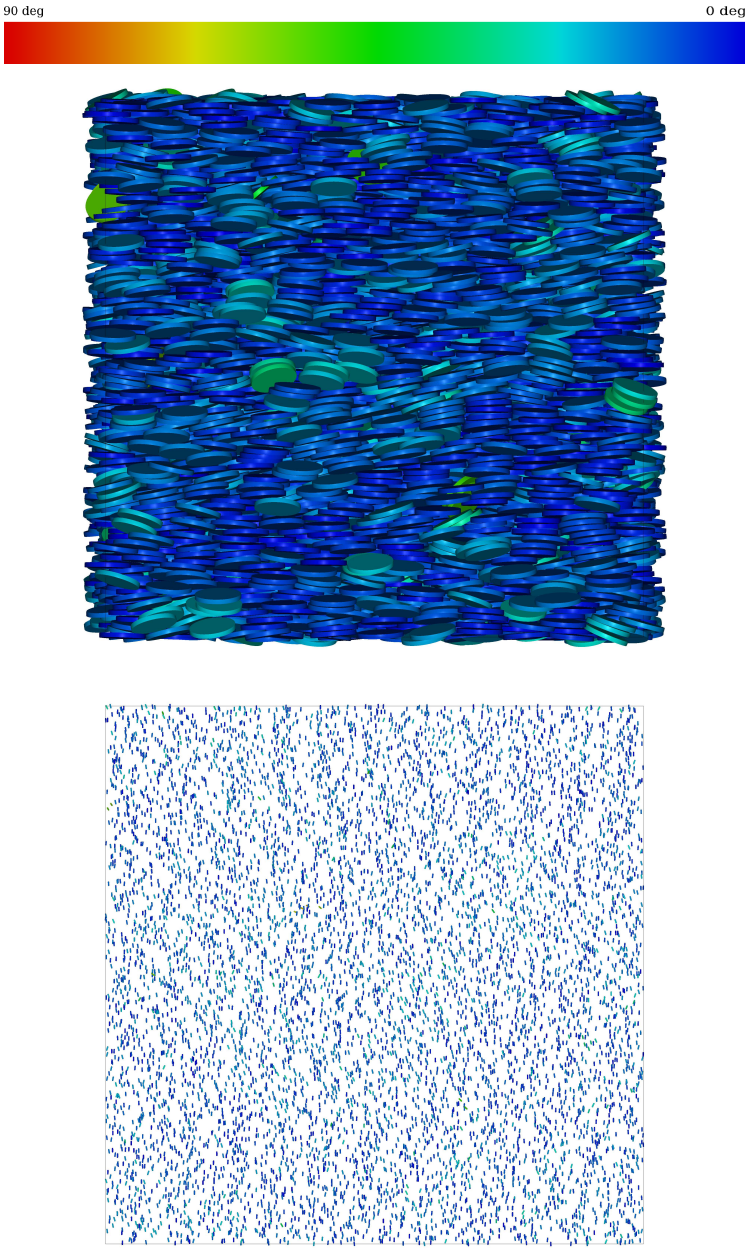

Figure 4.20: Instantaneous configuration of a system of hard cut-spheres, $L/D = 1/10$, for $\rho D^3 = 5.2$. The colour coding colours molecules according to their angle relative to the vertical axis: blue along the axis, red normal to the axis. The molecules are plotted as cut-spheres with diameter D and thickness L (upper image) and rods of length L (lower).

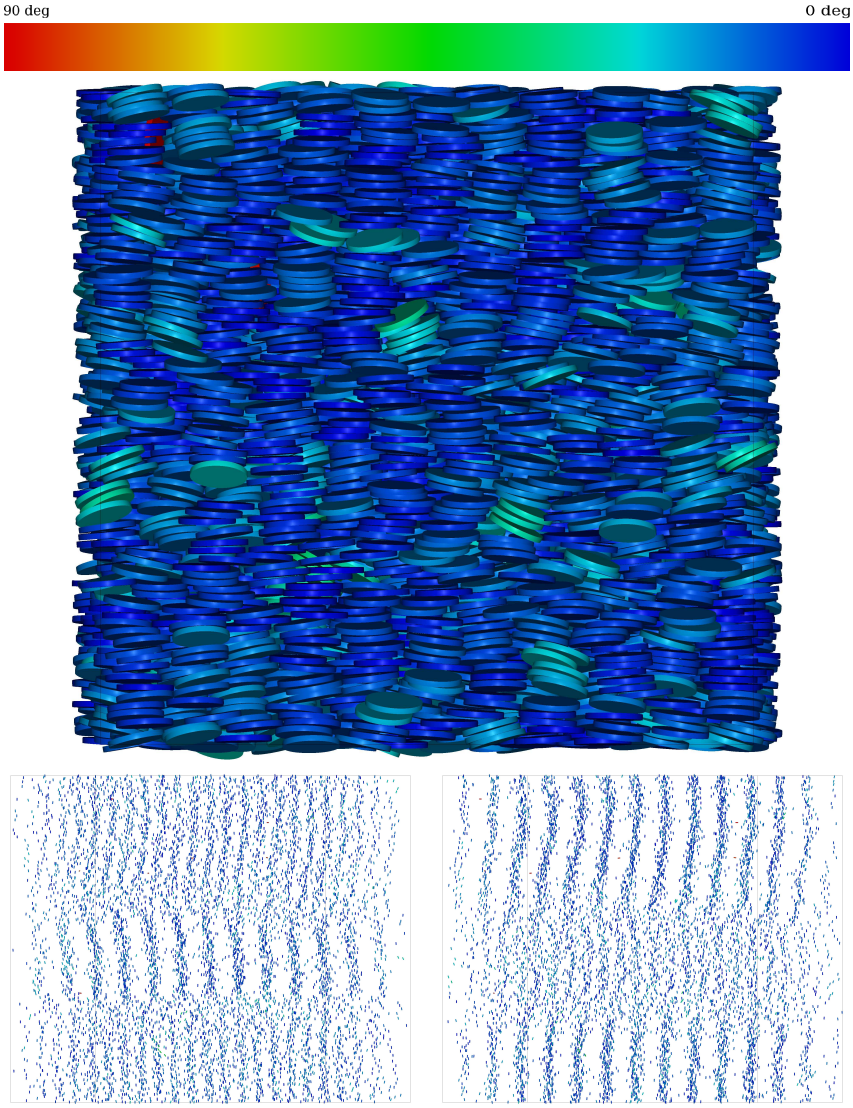

Figure 4.21: Instantaneous configuration of a system of hard cut-spheres, $L/D = 1/10$, for $\rho D^3 = 5.5$. The colour coding colours molecules according to their angle relative to the vertical axis: blue along the axis, red normal to the axis. The molecules are plotted as cut-spheres with diameter D and thickness L (top image) and rods of length L (lower images), showing columnar regions whose constructs of lattice vectors are separated by a rotation of $\sim 30^\circ$ about the z-axis.

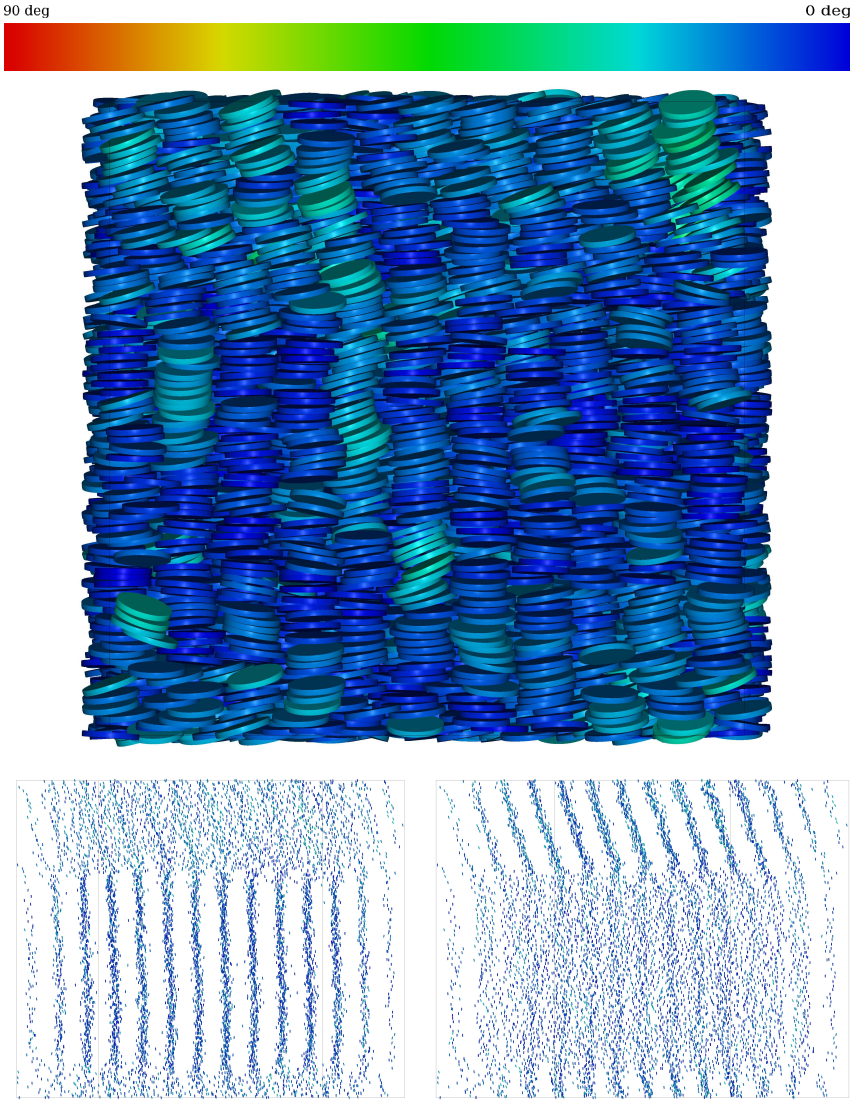

Figure 4.22: Instantaneous configuration of a system of hard cut-spheres, $L/D = 1/10$, for $\rho D^3 = 6$. The colour coding colours molecules according to their angle relative to the vertical axis: blue along the axis, red normal to the axis. The molecules are plotted as cut-spheres with diameter D and thickness L (top image) and rods of length L (lower images), showing columnar regions whose constructs of lattice vectors are separated by a rotation of $\sim 7^\circ$ about the z-axis.

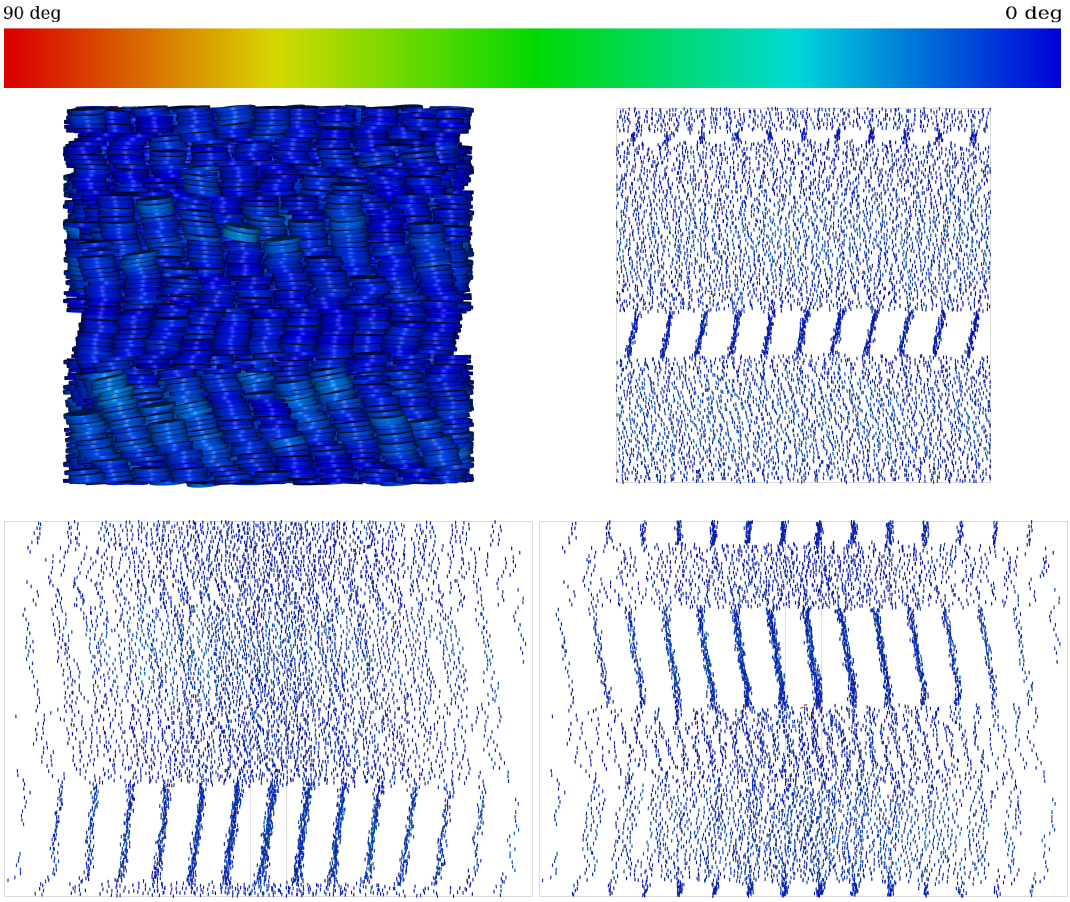

Figure 4.23: Instantaneous configuration of a system of hard cut-spheres, $L/D = 1/10$, for $\rho D^3 = 8$. The colour coding colours molecules according to their angle relative to the vertical axis: blue along the axis, red normal to the axis. The molecules are plotted as cut-spheres with diameter D and thickness L (upper left image) and rods of length L (remaining images). The three images of rods show the columnar order in several regions of the system. The lattice vectors for the first rod image can be mapped onto that of the second with a rotation about the z-axis of $\sim 11°$, with the lattice vectors for the final image obtained by a further rotation of $\sim 8°$.

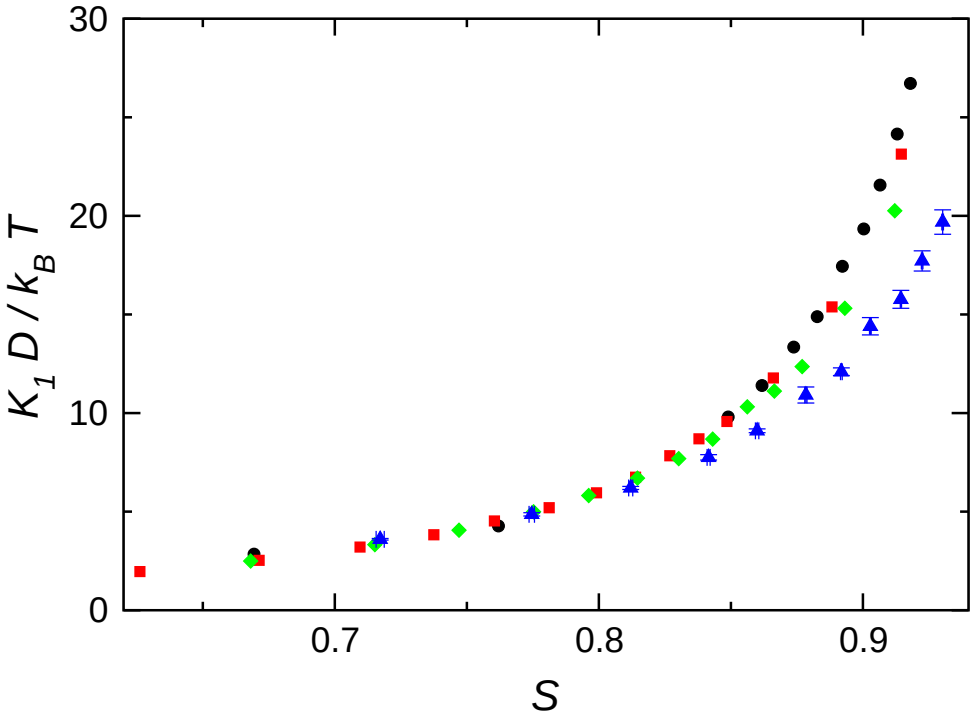

Figure 4.24: The splay elastic constant, K_1, as a function of order parameter for cut-spheres of varying thickness. $L/D \to 0$ (platelets), circles (black); $L/D = 1/20$, squares (red); $L/D = 1/15$, diamonds (green); $L/D = 1/10$, triangles (blue). The error bars are plotted for $L/D = 1/10$, and in the remaining cases the errors are smaller than the plotting symbols.

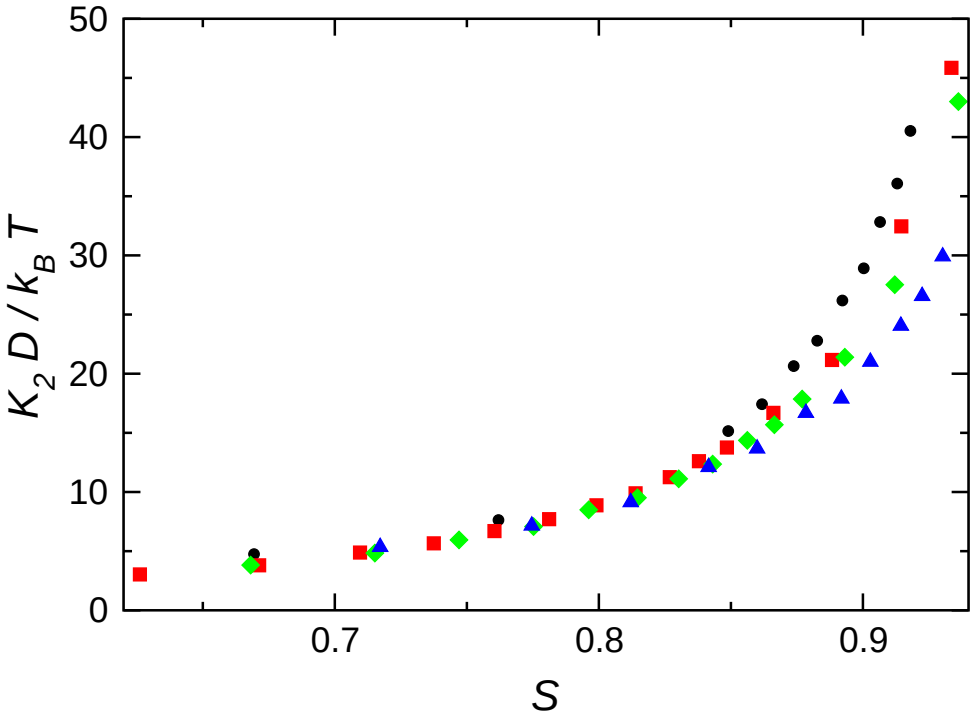

Figure 4.25: The twist elastic constant, K_2, as a function of order parameter for cut-spheres of varying thickness. $L/D \to 0$ (platelets), circles (black); $L/D = 1/20$, squares (red); $L/D = 1/15$, diamonds (green); $L/D = 1/10$, triangles (blue). In all cases the errors are smaller than the plotting symbols.

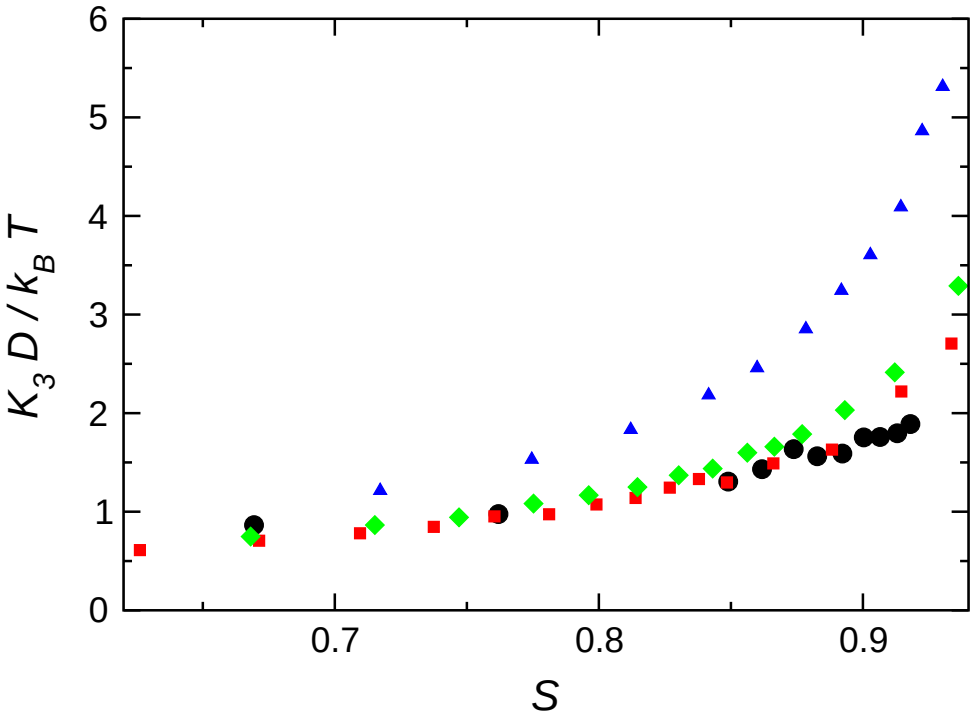

Figure 4.26: The bend elastic constant, K_3, as a function of order parameter for cut-spheres of varying thickness. $L/D \to 0$ (platelets), circles (black); $L/D = 1/20$, squares (red); $L/D = 1/15$, diamonds (green); $L/D = 1/10$, triangles (blue). In all cases the errors are smaller than the plotting symbols.

thickness.

Figures 4.27, 4.31, 4.35 show the functions $\mathcal{W}_{\alpha 3}(\boldsymbol{k})$, defined by eqn (3.16). As desired, the fitting functions describe the linear, low-k regime well, mostly passing through the data points within statistical error. $\mathcal{W}_{13}$ follows the structure over a maximum as k_1 and k_3 increase together and $\mathcal{W}_{23}$ describes the smoothing out of a sharply peaked profile in k_1 as k_3 increases.

This behaviour is also illustrated in Figures 4.28, 4.29, 4.32, 4.33, 4.36, 4.37, showing various slices of the data sets for $\mathcal{W}_{\alpha 3}(\boldsymbol{k})$. The structure for varying k_1 is more evident here, with the functions developing "kinks" or varying rapidly in the region of $(k_3 D)^2 \approx 35$–40, corresponding to a correlation distance $\lambda_1/D \approx 1.0$–1.1, i.e. close to the molecular diameter. It is apparent that the lower bend elastic constant, causing only gradually increasing fluctuations, couples with a lack of structure developing parallel to the director (compared to normal fluctuations) to allow more points to be included in the low-k treatment along to $\boldsymbol{n}$. Precursors to columnar order are increasingly visible in the $\mathcal{W}_{\alpha 3}$ for the thicker cut-spheres, in the form of more abrupt structure around the correlation distance, as well as statistical noise for higher-k_1.

Although the estimates for the elastic constants are sensitive to the range of wavevector spectrum and number of fitting parameters included, there is negligible visible effect on the low-k regions of each graph. Hence, we have plotted the fitting function as fitted up to the highest cutoff values of k chosen with the largest number of parameters used, in order to guide the eye over as much of the observed data as possible.

ρD^3	S	$K_1 D/k_\mathrm{B}T$	$K_2 D/k_\mathrm{B}T$	$K_3 D/k_\mathrm{B}T$
4.00	0.626(1)	1.96(4)	3.03(4)	0.611(8)
4.10	0.6713(8)	2.53(4)	3.80(4)	0.706(7)
4.20	0.7096(7)	3.2(2)	4.88(6)	0.78(5)
4.30	0.7375(5)	3.83(4)	5.66(8)	0.85(1)
4.40	0.7605(6)	4.53(5)	6.7(1)	0.95(2)
4.50	0.7812(4)	5.2(2)	7.70(7)	0.97(1)
4.60	0.7991(4)	5.95(6)	8.88(6)	1.074(9)
4.70	0.8139(3)	6.7(1)	9.89(7)	1.14(1)
4.80	0.8269(3)	7.83(8)	11.3(1)	1.24(1)
4.90	0.8379(4)	8.7(2)	12.60(8)	1.33(3)
5.00	0.8485(3)	9.57(9)	13.8(1)	1.30(1)
5.20	0.8661(3)	11.8(2)	16.7(2)	1.49(3)
5.50	0.8883(3)	15.4(3)	21.2(5)	1.63(3)
6.00	0.9145(3)	23.1(3)	32.5(6)	2.22(5)
6.49	0.9335(2)	34.1(6)	45.9(6)	2.71(7)
7.00	0.9463(2)	46.(1)	61.(1)	3.11(8)
7.50	0.9574(2)	60.2(6)	83.(1)	4.03(7)
8.00	0.9660(2)	83.(1)	115.(2)	4.9(2)

Table 4.3: Density ρD^3 of each simulation of cut-spheres with $L/D = 1/20$, with simulation averages of order parameter S, and elastic constants $K_\alpha D/k_\mathrm{B}T$. Figures in parentheses represent estimated errors in the last quoted digit.

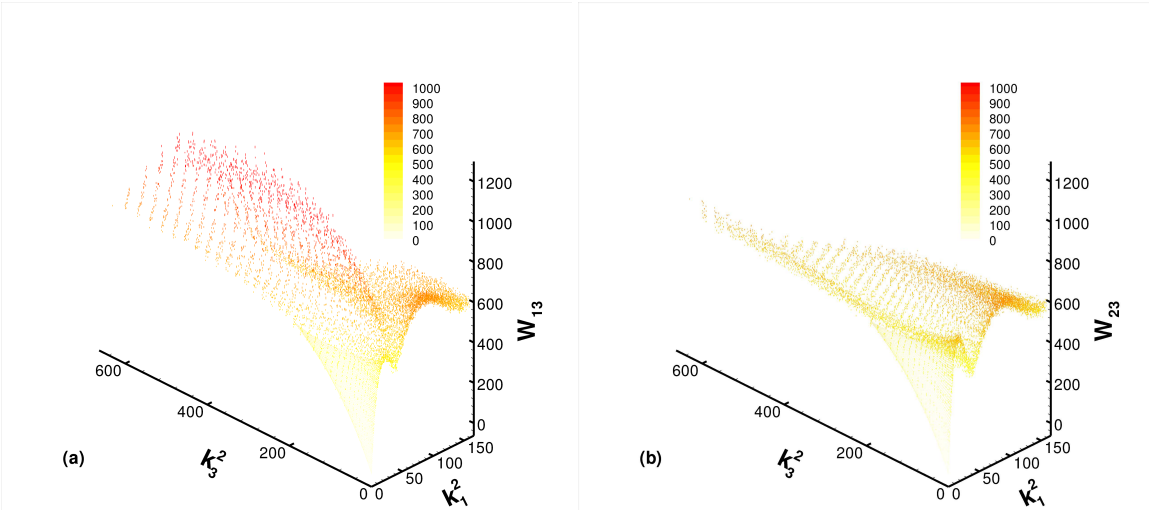

Figure 4.27: The functions $\mathcal{W}_{\alpha 3}$ as a function of wavevector components (k_1^2, k_3^2) at the $\rho D^3 = 8$ state point, for cut-spheres with $L/D = 1/20$. The simulation data with statistical error is given as a set of vertical lines, with the dotted surface representing the fitting function. The legends show the contour colour coding, with all units such that $D = 1$ and $k_B T = 1$.

ρD^3	S	$K_1 D/k_{\mathrm{B}}T$	$K_2 D/k_{\mathrm{B}}T$	$K_3 D/k_{\mathrm{B}}T$
4.00	0.668(1)	2.49(3)	3.82(5)	0.748(9)
4.10	0.7152(6)	3.32(5)	4.83(4)	0.86(2)
4.20	0.7470(8)	4.06(9)	5.95(8)	0.94(2)
4.30	0.7753(6)	4.99(4)	7.08(7)	1.083(9)
4.40	0.7962(5)	5.81(9)	8.5(1)	1.17(1)
4.50	0.8146(4)	6.70(8)	9.5(2)	1.25(2)
4.60	0.8303(3)	7.69(7)	11.1(1)	1.37(3)
4.70	0.8431(5)	8.68(8)	12.36(9)	1.44(2)
4.80	0.8562(3)	10.32(6)	14.4(2)	1.60(1)
4.90	0.8665(3)	11.1(2)	15.7(3)	1.66(3)
5.00	0.8770(3)	12.4(2)	17.9(4)	1.79(3)
5.20	0.8932(2)	15.3(2)	21.4(4)	2.03(2)
5.50	0.9121(4)	20.3(4)	27.5(5)	2.41(3)
6.00	0.9362(2)	30.2(3)	43.(1)	3.29(9)
6.49	0.9521(2)	43.9(8)	65.(1)	4.75(6)
7.00	0.9646(2)	59.7(7)	91.(1)	6.7(1)
7.50	0.9737(1)	76.(1)	122.(5)	9.4(2)

Table 4.4: Density ρD^3 of each simulation of cut-spheres with $L/D = 1/15$, with simulation averages of order parameter S, and elastic constants $K_\alpha D/k_{\mathrm{B}}T$. Figures in parentheses represent estimated errors in the last quoted digit.

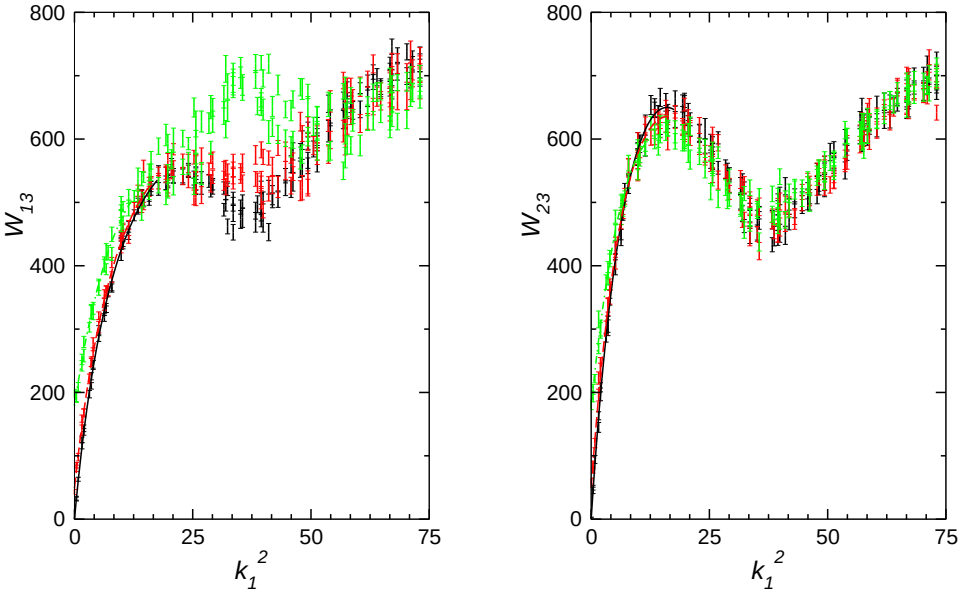

Figure 4.28: Slices through the $\mathcal{W}_{13}$ (left) and $\mathcal{W}_{23}$ (right) surfaces for fixed k_3 as a function of k_1^2, showing respectively splay and twist fluctuations, from simulations at the $\rho D^3 = 8$ state point, for cut-spheres with $L/D = 1/20$. The error bars give the data points with statistical error and the lines correspond to the fitting function for the entire surface in each case. $k_3 = 0$, full line (black); $k_3 = 15k_0$, dashed line (red); $k_3 = 30k_0$, dot-dashed line (green).

ρD^3	S	$K_1 D/k_\mathrm{B}T$	$K_2 D/k_\mathrm{B}T$	$K_3 D/k_\mathrm{B}T$
4.00	0.717(2)	3.60(4)	5.35(6)	1.21(1)
4.10	0.775(1)	4.86(8)	7.2(1)	1.53(2)
4.20	0.8121(8)	6.20(8)	9.1(2)	1.83(2)
4.30	0.8416(6)	7.8(1)	12.1(2)	2.18(6)
4.40	0.8599(6)	9.1(1)	13.7(2)	2.46(4)
4.50	0.8784(4)	10.9(4)	16.7(3)	2.85(7)
4.60	0.8918(3)	12.1(2)	17.9(3)	3.24(4)
4.70	0.9028(3)	14.4(4)	21.0(5)	3.60(4)
4.80	0.9144(2)	15.8(5)	24.0(4)	4.09(6)
4.90	0.9224(3)	17.7(5)	26.6(6)	4.86(6)
5.00	0.9302(3)	19.7(6)	29.9(6)	5.31(6)
5.20	0.9425(2)	23.5(5)	37.(2)	6.7(1)

Table 4.5: Density ρD^3 of each simulation of cut-spheres with $L/D = 1/10$, with simulation averages of order parameter S, and elastic constants $K_\alpha D/k_\mathrm{B}T$. Figures in parentheses represent estimated errors in the last quoted digit.

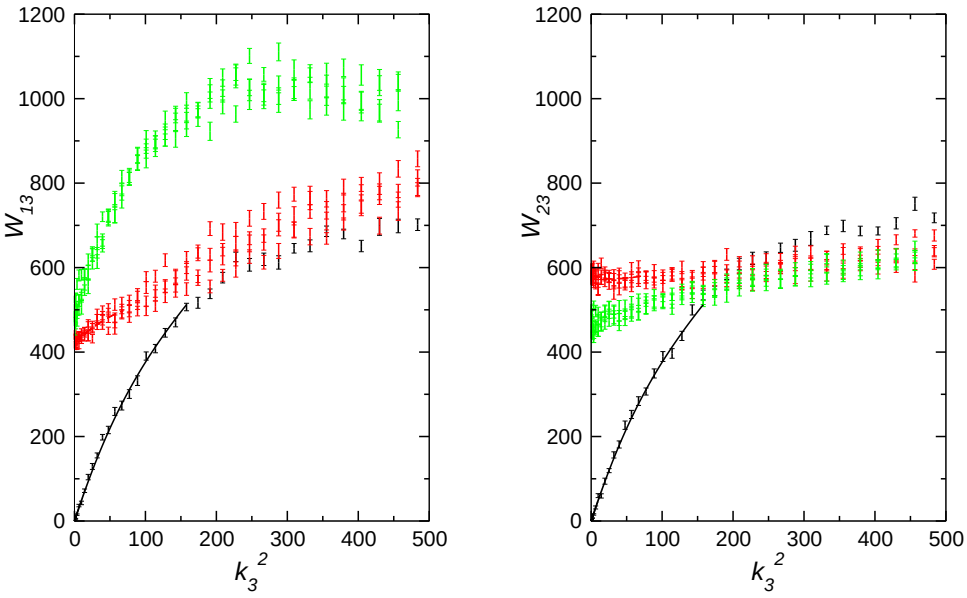

Figure 4.29: Slices through the $\mathcal{W}_{13}$ (left) and $\mathcal{W}_{23}$ (right) surfaces for fixed k_1 as a function of k_3^2, showing bend fluctuations, from simulations at the $\rho D^3 = 8$ state point, for cut-spheres with $L/D = 1/20$. The error bars give the data points with statistical error and the lines correspond to the fitting function for the entire surface in each case. $k_1 = 0$, full line (black); $k_1 = 5k_0$, dashed line (red); $k_1 = 10k_0$, dot-dashed line (green).

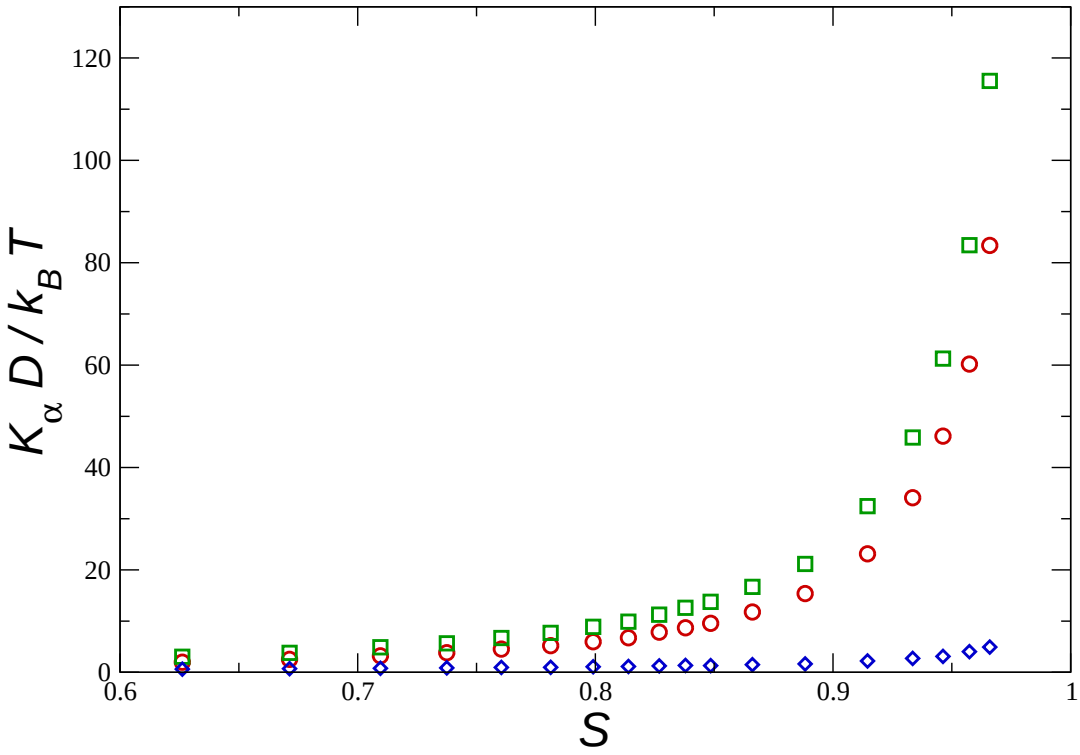

Figure 4.30: The splay, twist and bend elastic constants as a function of order parameter, for cut-spheres with $L/D = 1/20$. Splay, K_1, circles (red); twist, K_2, squares (green); bend, K_3, diamonds (blue). In all cases the errors are smaller than the plotting symbols, with those for K_3 being smaller by a factor of 3 or more.

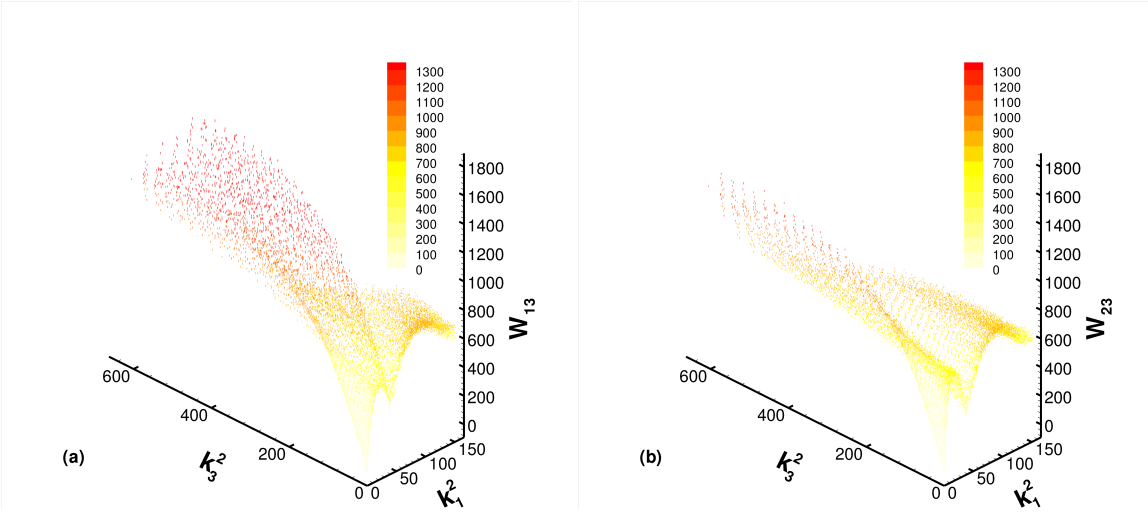

Figure 4.31: The functions $\mathcal{W}_{\alpha 3}$ as a function of wavevector components (k_1^2, k_3^2) at the $\rho D^3 = 7.5$ state point, for cut-spheres with $L/D = 1/15$. The simulation data with statistical error is given as a set of vertical lines, with the dotted surface representing the fitting function. The legends show the contour colour coding, with all units such that $D = 1$ and $k_B T = 1$.

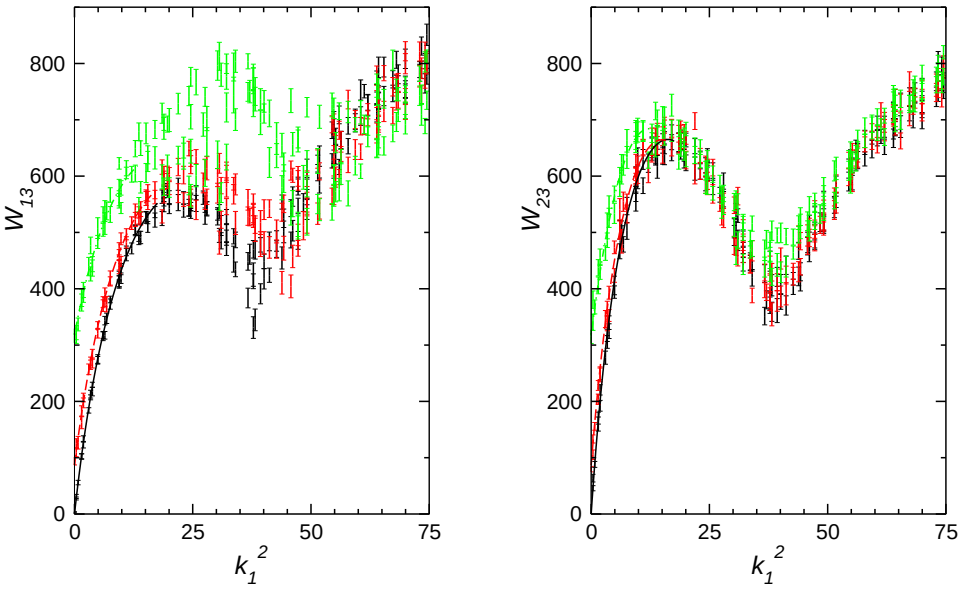

Figure 4.32: Slices through the $\mathcal{W}_{13}$ (left) and $\mathcal{W}_{23}$ (right) surfaces for fixed k_3 as a function of k_1^2, showing respectively splay and twist fluctuations, from simulations at the $\rho D^3 = 7.5$ state point, for cut-spheres with $L/D = 1/15$. The error bars give the data points with statistical error and the lines correspond to the fitting function for the entire surface in each case. $k_3 = 0$, full line (black); $k_3 = 15k_0$, dashed line (red); $k_3 = 30k_0$, dot-dashed line (green).

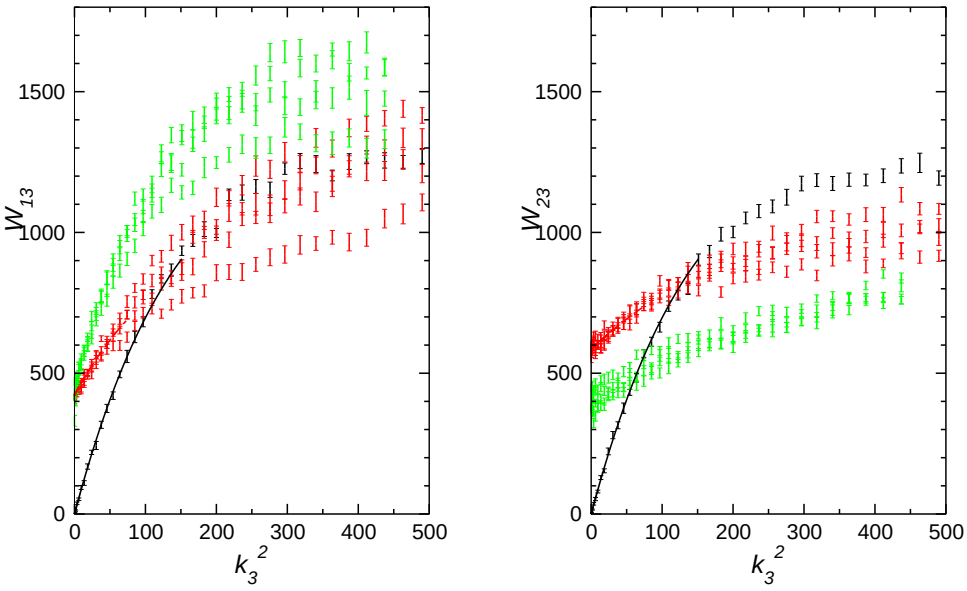

Figure 4.33: Slices through the $\mathcal{W}_{13}$ (left) and $\mathcal{W}_{23}$ (right) surfaces for fixed k_1 as a function of k_3^2, showing bend fluctuations, from simulations at the $\rho D^3 = 7.5$ state point, for cut-spheres with $L/D = 1/15$. The error bars give the data points with statistical error and the lines correspond to the fitting function for the entire surface in each case. $k_1 = 0$, full line (black); $k_1 = 5k_0$, dashed line (red); $k_1 = 10k_0$, dot-dashed line (green).

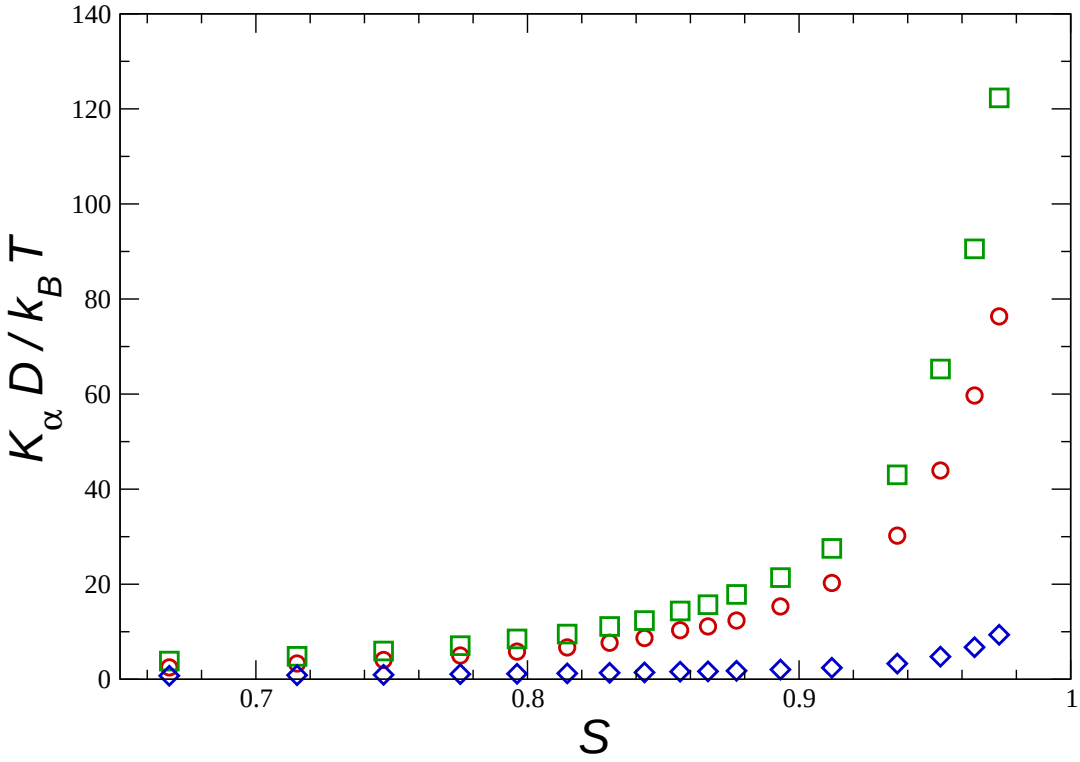

Figure 4.34: The splay, twist and bend elastic constants as a function of order parameter, for cut-spheres with $L/D = 1/15$. Splay, K_1, circles (red); twist, K_2, squares (green); bend, K_3, diamonds (blue). In all cases the errors are smaller than the plotting symbols, with those for K_3 being smaller by a factor of 3 or more.

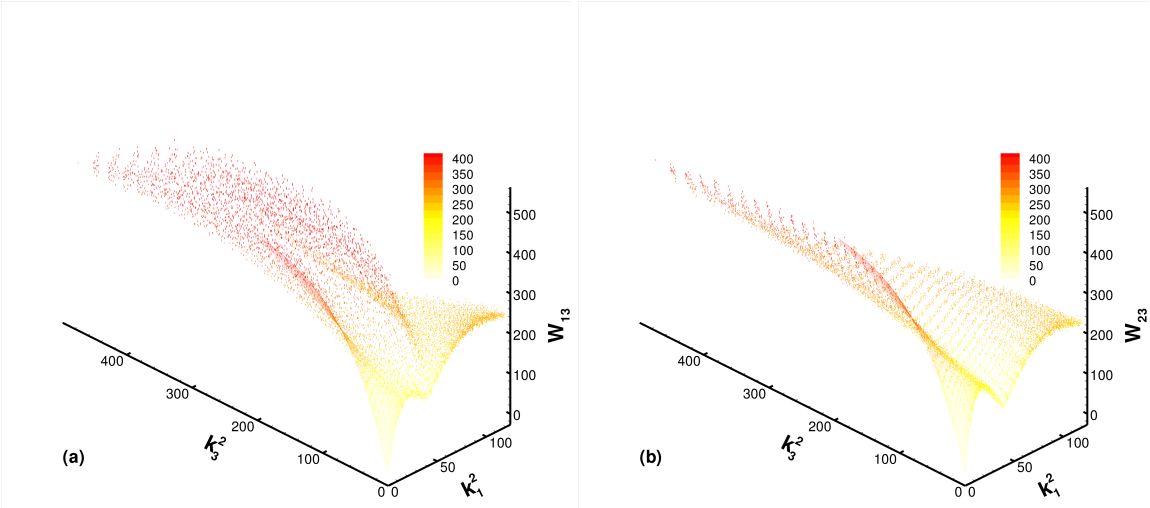

Figure 4.35: The functions $\mathcal{W}_{\alpha 3}$ as a function of wavevector components (k_1^2, k_3^2) at the $\rho D^3 = 5.2$ state point, for cut-spheres with $L/D = 1/10$. The simulation data with statistical error is given as a set of vertical lines, with the dotted surface representing the fitting function. The legends show the contour colour coding, with all units such that $D = 1$ and $k_B T = 1$.

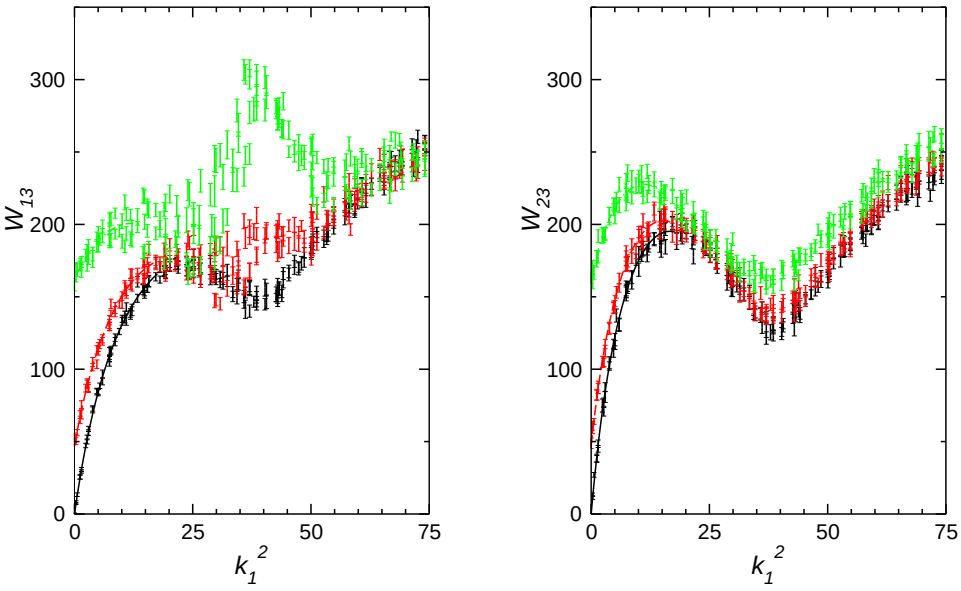

Figure 4.36: Slices through the $\mathcal{W}_{13}$ (left) and $\mathcal{W}_{23}$ (right) surfaces for fixed k_3 as a function of k_1^2, showing respectively splay and twist fluctuations, from simulations at the $\rho D^3 = 5.2$ state point, for cut-spheres with $L/D = 1/10$. The error bars give the data points with statistical error and the lines correspond to the fitting function for the entire surface in each case. $k_3 = 0$, full line (black); $k_3 = 15k_0$, dashed line (red); $k_3 = 30k_0$, dot-dashed line (green).

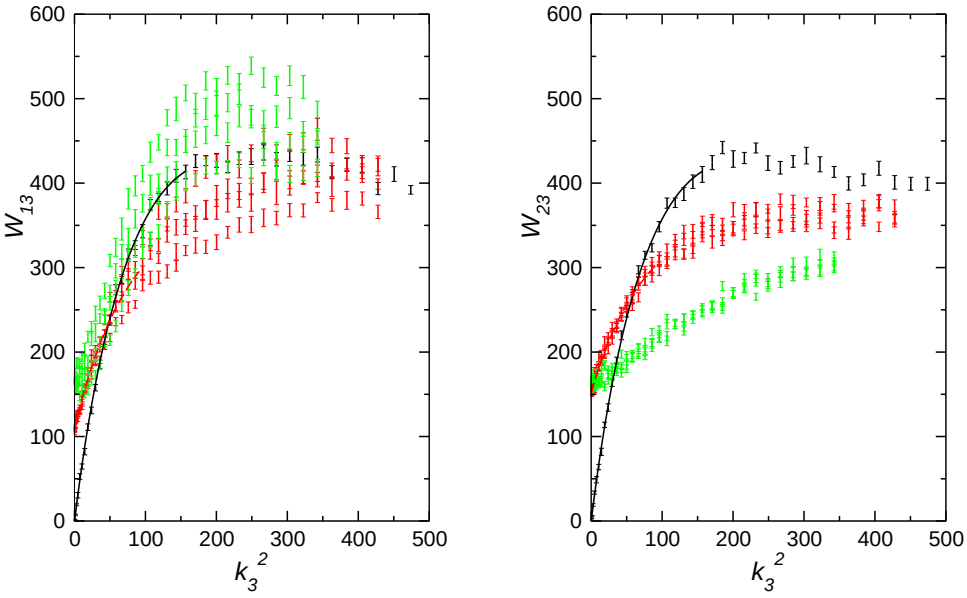

Figure 4.37: Slices through the $\mathcal{W}_{13}$ (left) and $\mathcal{W}_{23}$ (right) surfaces for fixed k_1 as a function of k_3^2, showing bend fluctuations, from simulations at the $\rho D^3 = 5.2$ state point, for cut-spheres with $L/D = 1/10$. The error bars give the data points with statistical error and the lines correspond to the fitting function for the entire surface in each case. $k_1 = 0$, full line (black); $k_1 = 5k_0$, dashed line (red); $k_1 = 10k_0$, dot-dashed line (green).

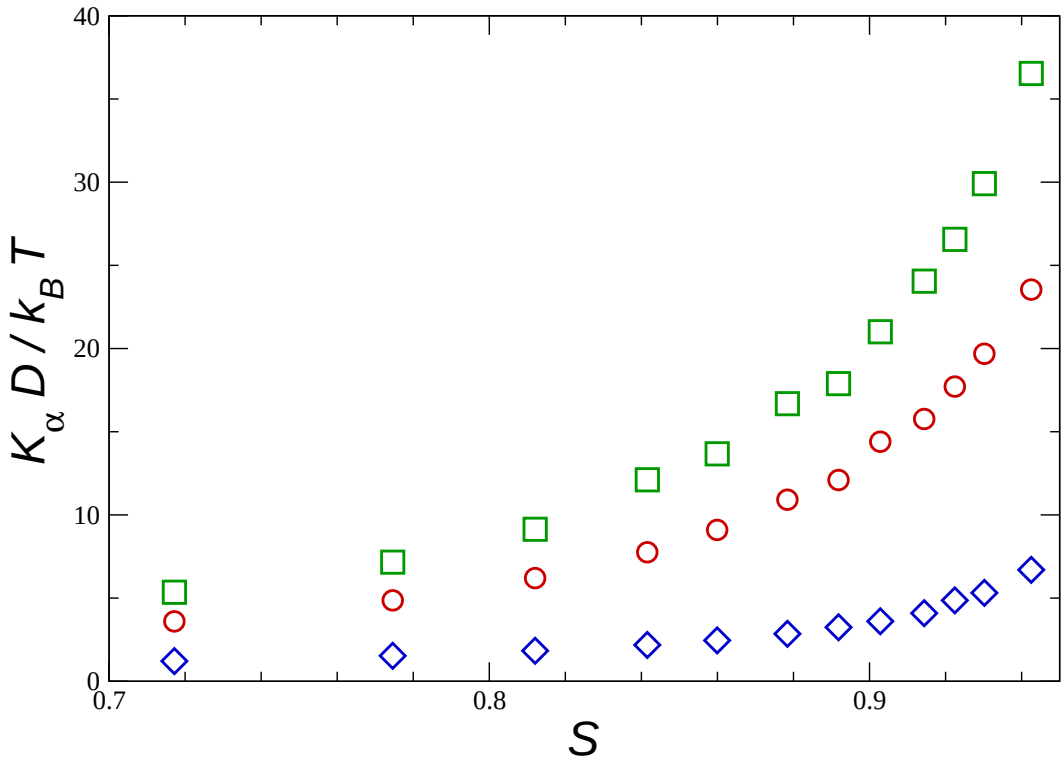

Figure 4.38: The splay, twist and bend elastic constants as a function of order parameter, for cut-spheres with $L/D = 1/10$. Splay, K_1, circles (red); twist, K_2, squares (green); bend, K_3, diamonds (blue). In all cases the errors are smaller than the plotting symbols, with those for K_3 being smaller by a factor of 3 or more.

Chapter 5

Wedge Geometry

5.1 Background

In recent years, several colloids have become real world examples of thin, hard disc-like molecules. Gibbsite, such an example, is quite monodisperse and can be synthesised with relative ease. Systems of both sterically- and charge-stabilised gibbsite platelets have been found to exhibit both nematic and columnar liquid crystalline phases. Orientational order may be induced at moderate magnetic field, they exhibit optical behaviour such as birefringence, form tactoids, undergo Frederiks transitions and such systems may be viewed using polarisation electron microscopy [van der Beek et al., 2006a]. This new experimental data has invited comparison with simulation and theory for bulk and confined discotic liquid crystals.

Theorists have encountered numerous problems in attempts to describe platelets, with the famous Onsager theory and others based upon it, though proven accurate for numerous systems of rods, failing to predict the phase diagram to required accuracy, with many of the peculiar features of the weakly first order isotropic-nematic phase transition completely unpredicted. However, fundamental measure theory (FMT), a density functional approach that includes contributions to the free energy from a third order density term, has provided an improved description of the equation of state and coexistence, and has shown quantitative agreement with simulation [Reich et al., 2007].

There have been a number of investigations into the behaviour of disc-like particles in confined geometry. Examining inhomogenous systems of liquid crystals can expose one to multiple phases, allowing the study of interfaces and exotic

geometric structures, each of which will be influenced by the interaction with the confining arrangement (or "walls"). This interaction may induce new phases, or change the properties of bulk phases and perturb the location of transitions on phase diagrams [Safran, 1994]. For particle between a pair of parallel walls, it has been shown experimentally that varying the wall separation can induce a sequence of phases [Pieranski et al., 1983]. There is a great deal of freedom in choosing a particle-wall interaction (or "type of wall"), and this can have a significant effect of the aforementioned modifications of confined systems. The effects of different types of wall interaction has also been investigated. We will provide some relevant details of such studies.

Wall and Cleaver [1997] performed Molecular Dynamics simulations on prolate (rod-like) Gay-Berne particles confined between two parallel walls. They chose an anisotropic molecule-wall interaction with two different coupling strengths, and these differences in the walls produced smectic phases with different levels of tilt in the surface layers at low temperature.

Cheung and Schmid [2005] performed Monte Carlo simulations of soft prolate ellipsoids in between "rough" walls. The walls were flat and hard, and roughness was introduced by embedding additional molecules with random conformations within the wall, and the number of embedded particles determined the level of roughness. They found that increasing surface roughness would reduce the density and order near the walls, as well as the anchoring coefficient.

Bellier-Castella et al. [2004] performed Monte Carlo simulations of oblate (disc-like) Gay-Berne molecules in between two types of parallel wall. One type favoured homeotropic (face-on) anchoring, with the other inducing planar (edge-on) anchoring. No change was found for either wall type in the isotropic-nematic transition compared to the bulk. However, the nematic-columnar transition temperature was found to increase for homeotropic anchoring and decrease for planar anchoring.

Piñeiro et al. [2007] performed Monte Carlo simulations of hard cut-spheres, with elongation = 1/10, between flat, parallel walls at several separations. They consider two types of hard wall interaction, one that favours homeotropic anchoring, with the other inducing planar anchoring. They found that, for homeotropic anchoring, the walls stabilise the nematic phase in the direction of the wall normal. For the other wall-interaction, the planar anchoring induces an adsorbed surface layer at each wall, acting as a rough hard wall for particles in the rest of the system, promoting isotropic and weaker nematic states. For each geometry, they calculate

the isotropic-nematic coexistence densities at a number of wall separations.

van der Beek et al. [2006b] performed experiments on a colloidal dispersion of sterically stabilised gibbsite platelets, under gravity in a glass column. They observed coexisting nematic and isotropic phases, and polarised light microscopy revealed that homeotropic anchoring was exhibited by the nematic phase at the bottom glass wall. They measured the rise of the meniscus at the side walls and used this value to and deduced the isotropic-nematic surface tension, which was in agreement with results from MC simulation and FMT.

Reich and Schmidt [2007] used fundamental measure density functional theory to investigate hard colloidal platelets confined between two parallel hard walls, favouring hometropic anchoring. They found that isotropic-nematic coexistence was shifted to lower values of chemical potential relative to the bulk system, and the coexistence vanished below a critical wall separation.

When investigating the properties of liquid crystals, one must change the state parameters of the system in order to determine the effect on these properties, as well as to observe new phases. For bulk systems, the state point may be specified by the chemical potential, density, pressure, or indeed any state variable that is valid. For systems in confined geometry, the chemical potential μ is a convenient quantity to specify the state point, as it is equal to the chemical potential of the bulk that is considered to be in equilibrium with the system [Binder, 1986]. Usually, when implementing a simulation study, one must organise an array of simulations that performs the calculations at a variety of state points.

There are techniques to make this more convenient, but it is also possible to use a "local approximation" to sample properties of many of these state points in one system. Applying a gravitational field throughout a system, for example, effectively induces a linear profile of the chemical potential, and this method is often said to invoke "sedimentation equilibrium". The local approximation assumes that each region of the system, with its independent value for the effective chemical potential, can be considered a subsystem that is representative of the bulk at the same value for μ. Provided that there is efficient sampling throughout the entire system, allowing particles to flow into and out of each region corresponding to each effective chemical potential, and the entire system is sufficiently large so as to ensure that the induced effective chemical potential is roughly constant over enough particle lengths to allow the fluid to exhibit the bulk properties, the approximation does not seem unreasonable. Calculations of the osmotic equation of state have shown that

systems under sedimentation equilibrium can represent the bulk accurately [Savenko and Dijkstra, 2004]. Simulation and theory incorporating gravity can be useful for comparison with experiment, and for liquid crystals there can be orientational and magnetic coupling to the gravitational field [Biben et al., 1993].

Reich and Schmidt [2010] performed fundamental measure density functional calculations on colloidal platelets in the presence of an aligning magnetic field, with and without the application of a gravitational field. For the system without gravity, paranematic-nematic coexistence was observed up until a critical value of the magnetic field strength. With the gravitational field, equilibrium sedimentation profiles were observed with a paranematic-nematic interface, the height of which would decrease with increasing gravitational strength, and increase with increasing aligning field strength. They also predicted, using a simple model for birefringence, the colour variation observed when such a system is viewed through crossed polarisers.

There are other applications of the local approximation. Considering a system of molecules in between flat parallel walls with set separation, one could be interested in the variation for different state points and wall separations. A system under sedimentation equilibrium could be constructed, with parallel side walls, and the local approximation would relate the system to a set of independent simulations of fluid between walls at the different state points, i.e. set the wall separation and vary the chemical potential.

Alternatively, one could use set up a system with a pair of *almost* parallel walls, inclined by some small angle, yielding an arrangement that has a pair of (almost) parallel walls at very small separation at one end of the system, with the separation varying slowly as one inspects along the wedge. This method of specifying a state point, and varying the wall separation, allows one to use the local approximation to relate the system to a set of subsystems with a range of wall separations at a fixed chemical potential. The shape of this arrangement is often referred to as a "wedge" geometry, being "thick" at one end, and "thin and pointy" at the other. Wedges are sometimes triangular, having a flat wall at the thick end, or having the shape of a sector, like a slice of cake.

Wedges have been used to investigate the confined behaviour of hard spheres, with simulations observing packing on different types of lattice as the separations varied [Botan et al., 2009], and some theoretical approaches have been applied [Boda and Chan, 1999; Henderson, 2002b, 2004]. The wedge geometry with a local approximation will be convenient for calculating depletion potentials and wall adsorp-

tion, providing properties as a function of wall separation as the separation varies smoothly in small steps, thus allowing one to perform the integrals with relative ease.

Ever since the work of [Asakura and Oosawa, 1954], depletion forces have been well-studied for a variety of surfaces immersed in a suspension of various macromolecules [Gotzelmann et al., 1998; Henderson, 2002a]. Very few treatments were performed for disc-like depletants before Piech and Walz [2000] managed to stabilise a suspension of silica spheres and silica coated gibbsite platelets. This prompted investigations of the depletion force between large hard spheres immersed in platelets, with Oversteegen and Lekkerkerker [2003] using a first-order theory (non-interacting platelets) to test the Derjaguin approximation. Harnau and Dietrich [2002] investigated some properties of platelets near a hard wall (with homeotropic anchoring using FMT), and the same authors [Harnau and Dietrich, 2004] applied those results, along with the Derjaguin approximation, to estimate the depletion forces between hard spheres in platelets. These theoretical approaches invite comparison with simulation, such as those mentioned earlier in this section. There has been little consideration of planar anchoring for discs in the literature, with no mention of a planar surface phase, although layers resembling such a phase were observed for cut-spheres [Piñeiro et al., 2007].

5.2 System Details

The simulated system consists of a fluid of infinitely thin hard discs (interaction potential between a pair of molecules $V_{ij} = \infty$ if the molecules overlap, and zero otherwise). The overlap criterion is described elsewhere [Eppenga and Frenkel, 1984; Allen et al., 1993]. For this system, due to the absence of any finite interaction potentials, the temperature is irrelevant, except as a scaling factor for energies and free energies. Reduced units of energy in these simulations are obtained by taking $k_{\mathrm{B}}T = 1$ and reduced units of distance by setting the platelet diameter $D = 1$.

Also present in each system are two types of hard wall, those that favour homeotropic surface anchoring of the platelets (by excluding the entire molecule), as well as those that induce planar anchoring (due to exclusion of only the centre of each platelet). Several instances of these wall boudary conditions are incident to form the wedge geometry. Two planar walls are placed almost parallel to one another, termed the "side" walls, oriented with a small angle of separation, Θ. The

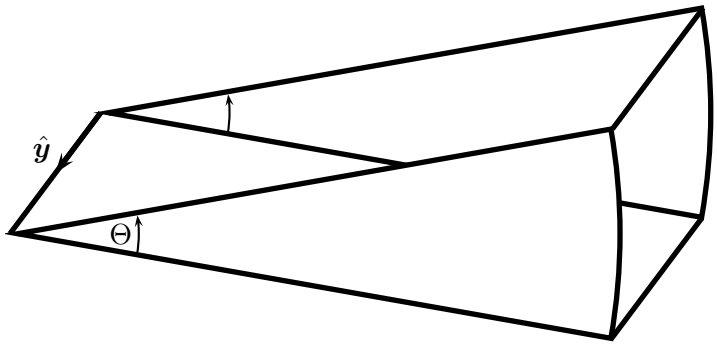

Figure 5.1: Sketch of the wedge geometry. It shows two hard, flat walls inclined at an angle Θ, with the line of intersection (vertex) lying along the y-axis. It is equal to the region mapped out by $\boldsymbol{r}(r, \theta, y)$ for $0 < r < R$, $-\Theta/2 < \theta < \Theta/2$ and $-L_y/2 < y < L_y/2$. We apply periodic boundary conditions along the y-direction. It resembles a sectoral slice from a cylindrical cake.

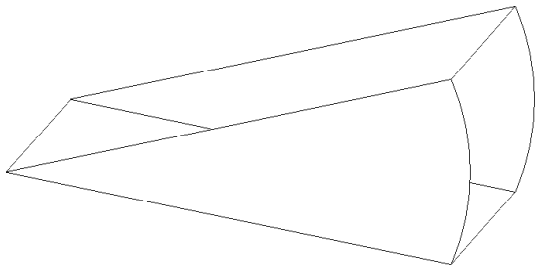

Figure 5.2: Sketch of the wedge geometry. It is equal to the region mapped out by $\boldsymbol{r}(r, \theta, y)$ for $0 < r < R$, $-\Theta/2 < \theta < \Theta/2$ and $-L_y/2 < y < L_y/2$. We apply periodic boundary conditions along the y-direction, and the dotted lines give the lines of intersection beween two flat planar walls and a curved, cylindrical wall. It resembles a sectoral slice from a cylindrical cake.

line of intersection between the planes forms the vertex of the wedge. A final wall with cylindrical curvature (of radius R), termed the "end" wall, is placed such that the cylindrical axis lies along the vertex. This arrangement results in a structure that is closed within the plane normal to the vertex, and open along it.

It is most convenient to express position coordinates within the wedge in terms of cylindrical coordinates, with r being the radial coordinate (equal to the perpendicular distance from the vertex of the wedge), and θ as the angular coordinate (describing rotation about the vertex). Using this convention, the side walls can be expressed as $\theta = \pm\Theta/2$, with the end wall described by $r = R$. Choosing the y-axis to lie along the vertex allows the xz-plane to contain r and θ, and thus position vectors are denoted (r, θ, y). Periodic boundary conditions are applied in the y-direction, and the profiles of observed quantities will be uniform in y due to the inability of platelets to form positionally ordered phases. The arc distance coordinate, $s = r\theta$, is also useful. The arc separation of the side walls, $w(r) = r\Theta$, as one inspects further up the wedge (away from the vertex), will be used to relate the different regions of the wedge to systems with parallel walls of separation w. Note that $-w/2 < s < w/2$.

The choice between homeotropic and planar anchoring-inducing walls in both the side and end walls will have dramatic effects of the order profiles. There are four combinations of type of side walls with type of end wall. If both favour homeotropic anchoring, discontinuities will be present in the director field $\boldsymbol{n}(\boldsymbol{r})$ due to the preferred director in the vicinity of the side walls being (approximately) normal to that near the end wall. As there is no director, $\boldsymbol{n}_\mathrm{c}$, that could be present throughout the entire system that would be commensurate with these boundary conditions, no simulations were performed for this case. For homeotropic anchoring near the side walls and planar anchoring in proximity to the end wall, a director along the x-axis throughout the system would be commensurate with the walls, hence the commensurate vector $\boldsymbol{n}_\mathrm{c} = \hat{\boldsymbol{x}}$ may be used to refer to this system. For planar anchoring close to the side walls, $\boldsymbol{n}_\mathrm{c} = \hat{\boldsymbol{y}}$ would be commensurate for an end wall inducing planar anchoring, with $\boldsymbol{n}_\mathrm{c} = \hat{\boldsymbol{z}}$ commensurate for a homeotropic-favouring end wall.

Monte Carlo simulations were performed for systems of hard platelets with wedge geometry in the canonical ensemble, at sixteen state points for each $\boldsymbol{n}_\mathrm{c} = \hat{\boldsymbol{x}}, \hat{\boldsymbol{y}}, \hat{\boldsymbol{z}}$. The initial configurations were constructed by setting particle orientations equal to $\boldsymbol{n}_\mathrm{c}$, ensuring no molecule overlaps due to their infinitesimal thickness, then choosing positions such that no wall overlaps were present. Then, for each system,

several runs of 10^6 sweeps were performed whilst experimenting with measuring different profiles on a cylindrical lattice, providing equilibration. Satisfactory equilibration was judged based upon observing a sufficiently uniform chemical potential profile, $\mu(r, \theta)$. Finally, production runs of 5×10^6 sweeps were performed, a relatively large number of sweeps required to obtain good statistics over a fine grid. Displacement parameters were chosen to give a move acceptance rate in the range 30–40%.

Of the wall overlap critera, the platelet near a flat, parallel wall has an analytical expression and is well studied. If $\boldsymbol{r}_\mathrm{w}$ is a point on a wall defined by wall normal $\hat{\boldsymbol{\nu}}$, pointing toward the inside of the system, then the closest distance between the wall and the centre of platelet i is given by $d_\mathrm{perp} = (\boldsymbol{r}_i - \boldsymbol{r}_\mathrm{w}) \cdot \hat{\boldsymbol{\nu}}$. For the flat wall favouring planar anchoring, $d_\mathrm{perp} < 0$ implies an overlap, with $d_\mathrm{perp} < \frac{D}{2}\left[1 - (\boldsymbol{u}_i \cdot \hat{\boldsymbol{\nu}})^2\right]^{1/2}$ giving the overlap criterion for the wall that favours homeotropic anchoring. For the curved end wall, in the case of planar-inducing geometry, we simply take the radial coordinate, r, for the molecule i and check that it does not exceed R to rule out an overlap. For homeotropic anchoring at the end of the wedge, however, where the wall excludes the entirety of each platelet, no method for determining the overlap was available in the literature. For the closest distance between a platelet and a cylindrical wall, we simply represented the rim of the platelet i by a coordinate vector $\boldsymbol{r}_\mathrm{rim}(\psi)$, where ψ parameterises each point on the molecule edge, then defined a radial distance function as $d_\mathrm{rad}(\psi) = r_\mathrm{rim}(\psi) - R$, and finally performed a numerical algorithm to minimise d_rad with respect to the parameter ψ. This minimum value would be < 0 should an overlap be present.

The systems each contain a fixed number of molecules, leaving an average density, $\langle \rho(\boldsymbol{r}) \rangle$. Averaging $\mu(r, \theta)$ over regions with good statistics will provide an estimate for the chemical potential of the system, μ. The pressure $P(w)$ between the side walls as we inspect along the wedge, depending on the wall arc separation, $w(r)$, may be calculated from an extrapolation of some edge density profile to find the wall contact value $\beta P\left(w(r)\right) = \rho_\mathrm{edge}(r, \theta = \pm\Theta/2)$. For walls inducing planar anchoring, which exclude the centre of each molecule, ρ_edge will simply be the number density of the molecule centres, $\rho(\boldsymbol{r})$. For the hometropic-inducing walls, excluding each platelet in its entirety, $\rho_\mathrm{edge}(\boldsymbol{r})$ is the density profile in which each molecule makes a contribution to the function at the coordinate of its edge with closest perpendicular

distance to the wall, i.e.

$$\rho_{\text{edge}}(\boldsymbol{r}) = \frac{1}{V}\sum_{i=1}^{N}\delta(\boldsymbol{r} - \boldsymbol{r}_{\text{edge}}) \tag{5.1}$$

where V is the system volume and $\delta(\cdots)$ is the Dirac delta function. $P(w)$ should converge to the bulk value of the pressure, P_{bulk}, in the limit of large w. As our wedge system will extend to only some finite value of w, we will check that $P(w)$ converges to some consistent limit well within our range, and take some average of $P(w)$ over the flat region with large w, termed $P(w_{\text{max}})$, and use it for our estimate of P_{bulk}.

The function $P(w)$ provides us with the outward pressure exterted by the fluid on the walls for different regions of the wedge. If the density and order profiles do not vary significantly over characteristic molecular length scales[Lu et al., 2007], a local approximation may be applied that is analagous to that in the work of Biben et al. [1993] on sedimentation equilibria and the osmotic equation of state. As the side walls in the wedge are roughly parallel, we will use the Derjaguin approximation. this allows one to use $P(w)$ as an estimation of the pressure between a range of systems consisting of platelets between parallel walls with a variety of wall separations, w. The validity of this and other profiles will determine whether the Derjaguin approximation is appropriate. Considering each such system immersed within a large reservoir of platelets, held at a chemical potential equal to that measured within our wedge, μ, then the surrounding fluid would exert an inward pressure on the walls equal to $P_{\text{bulk}}(\mu)$. The depletion force per unit wall area will then be given by $f_{\text{dep}}(w) = P(w) - P_{\text{bulk}}(\mu)$, i.e. the resultant outward pressure experienced by the walls due to the exclusion of a cell of bulk fluid with equal volume. From this definition, $f_{\text{dep}} > 0$ would be the case should depletion drive the walls apart. The depletion potential per unit wall area is defined by

$$W_{\text{dep}}(w) = -\int_{w'=\infty}^{w} f_{\text{dep}}(w')\mathrm{d}w' \tag{5.2}$$

and gives the work done in bringing the surfaces together from the far field, noninteracting limit to some separation w. The negative sign ensures that the depletion potential will be positive when the surfaces are brought together against a positive depletion force.

Some of the features of the depletion interaction can be captured by a first

order virial expansion. For the walls excluding only the centre of each molecule, the single-body term in the virial series will be independent of the wall separation, hence the first order theory predicts $W_{\mathrm{dep}}(w) = f_{\mathrm{dep}}(w) = 0$. The same is true for the walls that exclude the entire molecules for $w > D$, but for $w < D$ the orientations of a single molecule between the walls will be restricted. This leads to the following analytical expressions for the potential and force per unit area;

$$\frac{2\beta W_{\mathrm{dep}}(w)}{\rho_{\mathrm{bulk}} D} = \frac{w}{D}\left(1+\left(\frac{w}{D}\right)^2\right)^{1/2} - \sqrt{2} + \sinh^{-1}\left(\frac{w}{D}\right) - \sinh^{-1}(1) \quad (5.3)$$

$$\frac{\beta f_{\mathrm{dep}}(w)}{\rho_{\mathrm{bulk}}} = -\left(1+\left(\frac{w}{D}\right)^2\right)^{1/2} . \quad (5.4)$$

Another quantity of interest is the adsorption between the walls,

$$\sigma_{\mathrm{ex}}\big(w(r)\big) = \int_{s=-w/2}^{w/2} \big(\rho(r,s) - \rho_{\mathrm{bulk}}\big)\mathrm{d}s \quad (5.5)$$

providing a measure of the number of molecules per unit area that will be present between the walls in excess of those present in a bulk system of equal volume. In the limit of large w, this should be similar to the sum of the excess densities accumulating in the region of two isolated surfaces, i.e. twice the value of a single-wall adsorption.

The bulk equation of state will relate the pressure to the chemical potential, so this provides a useful check that our estimate for P_{bulk} against μ behaves as expected (see Figure 5.3). The equation of state may also be used to find the density of a bulk system with a matching chemical potential or pressure, ρ_{bulk}. Each state point is referred to by one of these state variables (μ, P or ρ), and the state point data are reported in Tables 5.1–5.3.

It was decided that a wedge with length $R/D = 100$ and angle $\Theta = 3.4°$, giving maximum arc width $w(R)/D \approx 6$ would provide a range of w sufficient to observe interesting pressure and adsorption profiles. Given our desired range of densities, system sizes of 5398–10797 platelets we required, enabling runs of 10^6 sweeps to complete in around 40–60 hours of CPU time, which was deemed acceptable.

Monte Carlo simulations were performed for systems of hard platelets with wedge geometry in the canonical ensemble, at sixteen state points for each $\boldsymbol{n}_{\mathrm{c}} = \hat{\boldsymbol{x}}, \hat{\boldsymbol{y}}, \hat{\boldsymbol{z}}$. The initial configurations were constructed by setting particle orientations equal to $\boldsymbol{n}_{\mathrm{c}}$, ensuring no molecule overlaps due to their infinitesimal thickness, then

choosing positions such that no wall overlaps were present. Then, for each system, several runs of 10^6 sweeps were performed whilst experimenting with measuring different profiles on a cylindrical lattice, providing equilibration. Satisfactory equilibration was judged based upon observing a sufficiently uniform chemical potential profile, $\mu(r, \theta)$. Finally, production runs of 5×10^6 sweeps were performed, a relatively large number of sweeps required to obtain good statistics over a fine grid. Displacement parameters were chosen to give a move acceptance rate in the range 30–40%.

Considerable memory was required to record all of the desired profiles for each state point of each wedge geometry on a grid of $\delta r = 0.1D$ and $\delta s \approx 0.01D$. The small value for δs was required to obtain an accurate estimation of the side wall contact density from an extrapolation. The size and volume of data files also meant that over 1TB of space was used on the CSC Network. It was also found that the size of the arrays used in the simulation program caused problems for the Intel Fortran compiler, thus that of the Portland Group was used to compile programs for the simulation runs.

5.3 Results

A number of profiles were calculated at each state point in wedge geometry for $\boldsymbol{n}_{\mathrm{c}} = \hat{\boldsymbol{x}}, \hat{\boldsymbol{y}}, \hat{\boldsymbol{z}}$, on a fine grid in the radial coordinate, r, and the arc distance, s. The contour plots were produced in Tecplot 360, and follow a variety of RGB colour codings. For each plot, a caption will specify a list of colours along with the corresponding value the plotted function will have at any point that each colour is plotted. For function values between those specified to correspond to a listed colour, several more contour levels will be interdispersed, with RGB values varying linearly (with constant spacing between consecutive levels), unless the caption reveals that the levels vary exponentially (with a term that increases by a fixed ratio between consecutive levels). Should function values above the highest mentioned contour level be present, these values will be plotted with the colour corresponding to that maximum level, with the lowest level contour colour being used for the function where it is below the corresponding minimum. The colour coding for the 3D plots is described in the same fashion.

In addition to quantities defined in earlier sections, plots of the excess density, $\rho_{\mathrm{ex}}(\boldsymbol{r}) = \rho(\boldsymbol{r}) - \rho_{\mathrm{bulk}}$, as well as several angles derived from the director, $\boldsymbol{n}$, were

$\langle\rho(\boldsymbol{r})\rangle D^3$	μ	$\beta P_{\text{bulk}} D^3$	$\rho_{\text{bulk}} D^3$
3	6.15(3)	10.78(7)	3.02
3.2	6.36(3)	11.61(9)	3.14
3.4	6.61(3)	12.33(9)	3.31
3.6	6.79(3)	13.06(8)	3.43
3.8	6.96(3)	13.60(9)	3.58
4	7.14(4)	14.12(9)	3.74
4.2	7.25(3)	14.5(1)	3.89
4.4	7.33(3)	14.90(9)	4.15
4.6	7.40(3)	15.25(9)	4.36
4.8	7.50(3)	15.68(9)	4.55
5	7.60(3)	16.1(1)	4.85
5.2	7.70(3)	16.6(1)	5.10
5.4	7.79(3)	17.1(1)	5.33
5.6	7.87(3)	17.6(1)	5.51
5.8	7.97(3)	18.2(1)	5.72
6	8.08(3)	18.7(1)	5.95

Table 5.1: State point data for the $\boldsymbol{n}_{\text{c}} = \hat{\boldsymbol{x}}$ wedge. The average density, $\langle\rho(\boldsymbol{r})\rangle D^3$, our estimates of the chemical potential from averaging over its profile, μ, and pressure from wall contact in the high-w limit, P_{bulk}, are provided along with the corresponding bulk density, ρ_{bulk}. Figures in parentheses represent estimated errors in the last quoted digit.

$\langle\rho(\boldsymbol{r})\rangle D^3$	μ	$\beta P_{\text{bulk}} D^3$	$\rho_{\text{bulk}} D^3$
3	5.33(2)	8.51(6)	2.60
3.2	5.64(2)	9.34(7)	2.74
3.4	5.93(2)	10.19(8)	2.89
3.6	6.17(3)	11.00(8)	3.03
3.8	6.45(3)	11.78(8)	3.21
4	6.68(3)	12.58(8)	3.37
4.2	6.89(3)	13.36(9)	3.52
4.4	7.08(3)	13.99(8)	3.69
4.6	7.26(3)	14.67(9)	3.92
4.8	7.39(3)	15.2(1)	4.36
5	7.47(3)	15.5(1)	4.48
5.2	7.53(3)	15.8(1)	4.66
5.4	7.59(3)	16.1(1)	4.81
5.6	7.66(3)	16.4(1)	5.01
5.8	7.74(3)	16.7(1)	5.22
6	7.81(3)	17.2(1)	5.38

Table 5.2: State point data for the $\boldsymbol{n}_{\text{c}} = \hat{\boldsymbol{y}}$ wedge. The average density, $\langle\rho(\boldsymbol{r})\rangle D^3$, our estimates of the chemical potential from averaging over its profile, μ, and pressure from wall contact in the high-w limit, P_{bulk}, are provided along with the corresponding bulk density, ρ_{bulk}. Figures in parentheses represent estimated errors in the last quoted digit.

$\langle\rho(\boldsymbol{r})\rangle D^3$	μ	$\beta P_{\text{bulk}} D^3$	$\rho_{\text{bulk}} D^3$
3	5.32(2)	8.60(6)	2.59
3.2	5.63(2)	9.42(7)	2.73
3.4	5.91(3)	10.27(8)	2.88
3.6	6.20(3)	11.06(8)	3.05
3.8	6.44(3)	11.82(9)	3.20
4	6.67(3)	12.63(8)	3.36
4.2	6.92(4)	13.4(1)	3.55
4.4	7.08(4)	14.02(9)	3.69
4.6	7.22(3)	14.66(8)	3.86
4.8	7.39(3)	15.2(1)	4.35
5	7.46(3)	15.5(1)	4.48
5.2	7.52(3)	15.8(1)	4.63
5.4	7.57(3)	16.0(1)	4.78
5.6	7.67(3)	16.5(1)	5.03
5.8	7.72(3)	16.8(1)	5.16
6	7.84(3)	17.2(1)	5.45

Table 5.3: State point data for the $\boldsymbol{n}_{\text{c}} = \hat{\boldsymbol{z}}$ wedge. The average density, $\langle\rho(\boldsymbol{r})\rangle D^3$, our estimates of the chemical potential from averaging over its profile, μ, and pressure from wall contact in the high-w limit, P_{bulk}, are provided along with the corresponding bulk density, ρ_{bulk}. Figures in parentheses represent estimated errors in the last quoted digit.

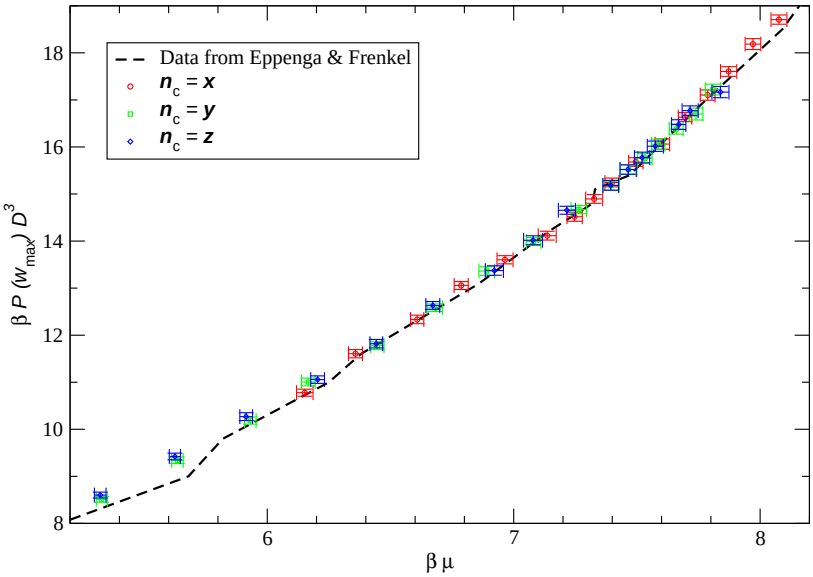

Figure 5.3: Plot of pressure against measured chemical potential for state points taken from each wedge geometry, compared to data from the bulk equation of state as calculated by Eppenga and Frenkel [1984]. It is worth noting that the values in the vicinity of the Isotropic-Nematic transition are $\beta\mu \approx 7.3$ and $\beta P_{\text{bulk}} D^3 \approx 15$

calculated. Consider a coordinate system in which the zenith (or polar) angle, $\theta_{\boldsymbol{n}}$, is measured from the x-axis, with the azimuthal angle, $\phi_{\boldsymbol{n}}$, lying in the yz-plane, with $\phi_{\boldsymbol{n}} = 0$ aligned with the z-axis. This allows the director to be written $\boldsymbol{n} = \big(\cos(\theta_{\boldsymbol{n}}), \sin(\theta_{\boldsymbol{n}})\sin(\phi_{\boldsymbol{n}}), \sin(\theta_{\boldsymbol{n}})\cos(\phi_{\boldsymbol{n}})\big)$, with the angles recovered via $\theta_{\boldsymbol{n}} = \cos^{-1}(\boldsymbol{n}\cdot\hat{\boldsymbol{x}})$ and $\phi_{\boldsymbol{n}} = \tan^{-1}\left(\frac{\boldsymbol{n}\cdot\hat{\boldsymbol{y}}}{\boldsymbol{n}\cdot\hat{\boldsymbol{z}}}\right)$.

All observed phases are liquid crystalline, exhibiting invariance to director inversion (the transformation $\boldsymbol{n} \to -\boldsymbol{n}$). We are interested in the angles only as parameters to indicate the degree of alignment parallel to each of the coordinate axes. Hence it is unnecessary to distinguish between the individual components, n_α, and their inversions, $-n_\alpha$, allowing us to use the same colour coding for $\theta_{\boldsymbol{n}}$ and $\pi - \theta_{\boldsymbol{n}}$, as well as for $\phi_{\boldsymbol{n}}$, $\pi \pm \phi_{\boldsymbol{n}}$ and $2\pi - \phi_{\boldsymbol{n}}$, when producing contour plots. Thus the caption for each plot includes the contour levels for $\theta_{\boldsymbol{n}}, \phi_{\boldsymbol{n}} \epsilon [0, \pi/2]$, and the colour coding for levels outside of this range will be such that $n_\alpha \to -n_\alpha$ does not change the contour colour, for each $\alpha = x, y, z$. For each figure containing a number of plots, the coordinate axes are shown on only one of the plots.

Figure 5.3 shows how the pressure from wall contact density observed in our simulations compares to the bulk equation of state as calculated by Eppenga and Frenkel [1984], when plotted against the observed chemical potential for each wedge geometry, $\boldsymbol{n}_{\mathrm{c}} = \hat{\boldsymbol{x}}, \hat{\boldsymbol{y}}, \hat{\boldsymbol{z}}$. The line joining the equation of state data passes through most of the data points for each wedge system within statistical error, which is encouraging for the process of obtaining the pressure from wall contact in the wedge systems. The poorest agreement is present for the points with lower μ, and it is unclear whether this is due to the effects of small system size in the literature, or whether the variation in density profiles in our wedge for low density is too abrupt to obtain an accurate value for the pressure from an extrapolation procedure. Notice that there is no visible deviation from a smooth relationship close to bulk values corresponding to the isotropic-nematic transition.

5.3.1 $\boldsymbol{n}_{\mathrm{c}} = \hat{\boldsymbol{x}}$

The phase behaviour present in the $\boldsymbol{n}_{\mathrm{c}} = \hat{\boldsymbol{x}}$ wedge for a range of state points can be determined from the plots in Figures 5.5–5.7, showing profiles of the middle eigenvalue and angles of the director. It is not necessary to show a plot from every state point, as for each profile some of the plots for the higher densities may be qualitatively the same, as will those for some of the lower densities. Examining the low-density profiles for the middle eigenvalue, one can see that the centre of the

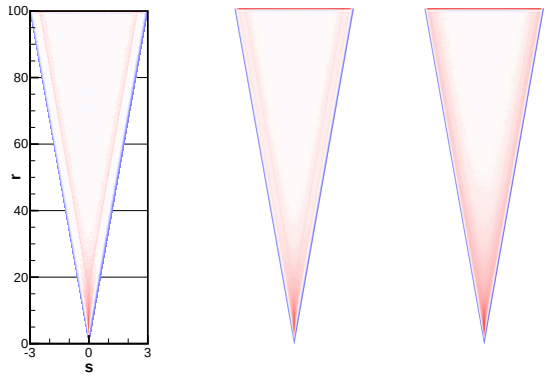

$\rho_{\text{bulk}}D^3 = 3.02$ 3.32 3.59

3.90 4.36 4.85

5.34 5.73 5.95

Figure 5.4: Profiles of $\rho_{\text{ex}}(\boldsymbol{r})$ for $\boldsymbol{n}_{\text{c}} = \hat{\boldsymbol{x}}$. The colour coding plots points as follows; $\rho_{\text{ex}}D^3 = -6$ blue, 0 white, 4 red.

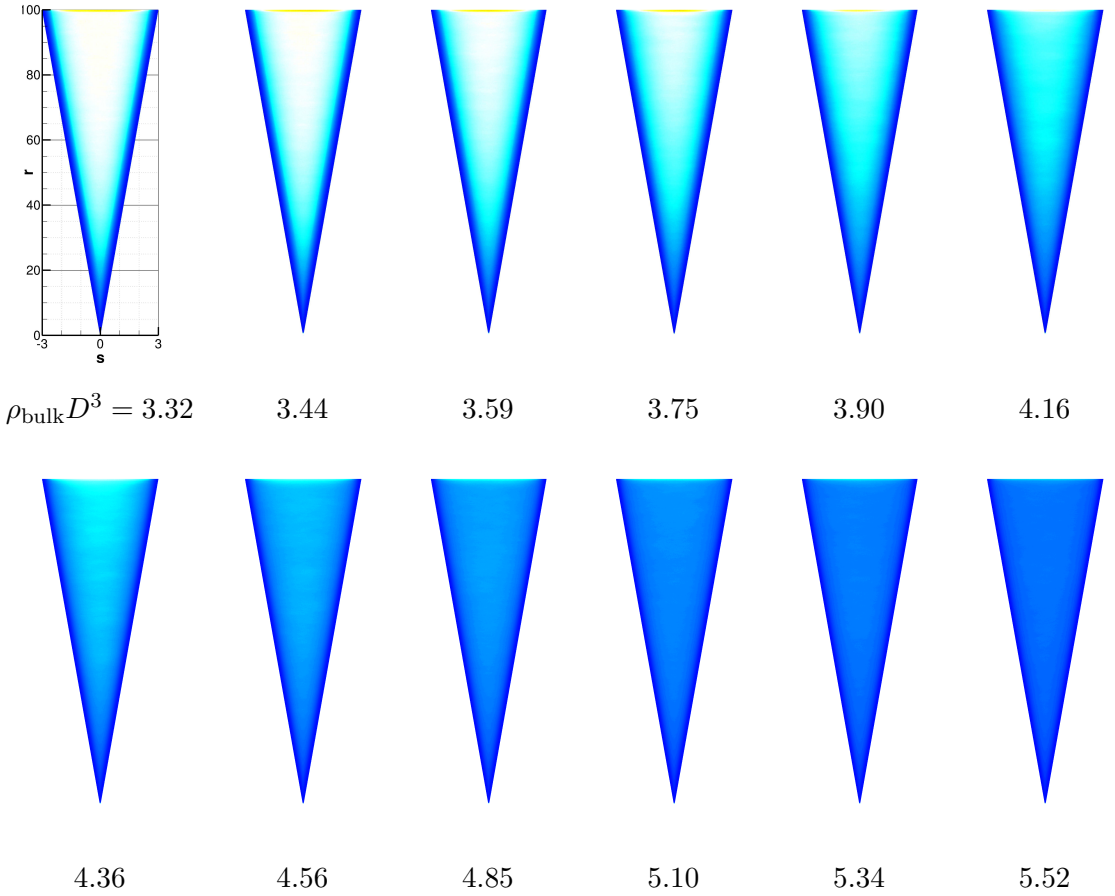

Figure 5.5: Profiles of λ^0 for $\boldsymbol{n}_{\text{c}} = \hat{\boldsymbol{x}}$. The colour coding plots points as follows; $\lambda^0 = -0.5$ blue, -0.25 cyan, 0 white, 0.125 yellow, 0.25 red.

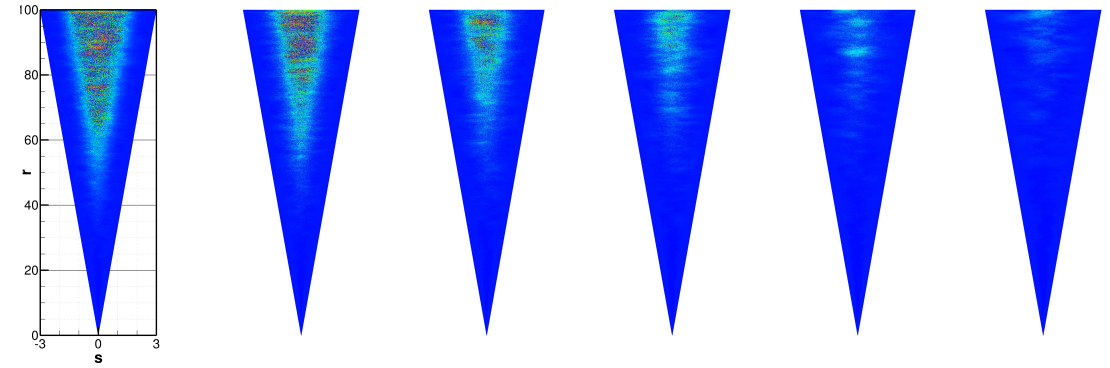

$\rho_{\text{bulk}}D^3 = 3.02$ 3.15 3.32 3.44 3.59 3.75

3.90 4.16 4.36 4.56 4.85 5.10

Figure 5.6: Profiles of $\theta_{\boldsymbol{n}}$ for $\boldsymbol{n}_{\text{c}} = \hat{\boldsymbol{x}}$. The colour coding plots points as follows; $\theta_{\boldsymbol{n}} = 0°$ blue, 22.5° cyan, 45° green, 67.5° yellow, 90° red.

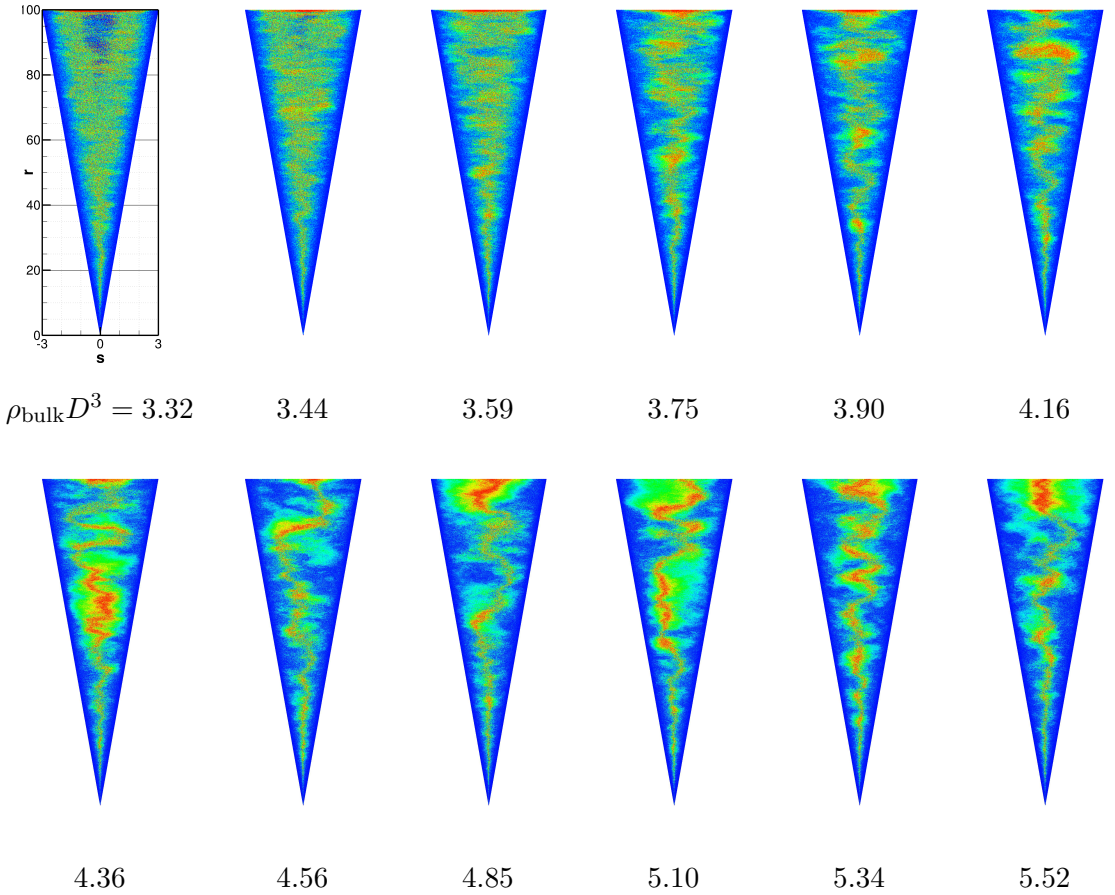

Figure 5.7: Profiles of $\phi_{\boldsymbol{n}}$ for $\boldsymbol{n}_{\text{c}} = \hat{\boldsymbol{x}}$. The colour coding plots points as follows; $\phi_{\boldsymbol{n}} = 0°$ blue, 22.5° cyan, 45° green, 67.5° yellow, 90° red.

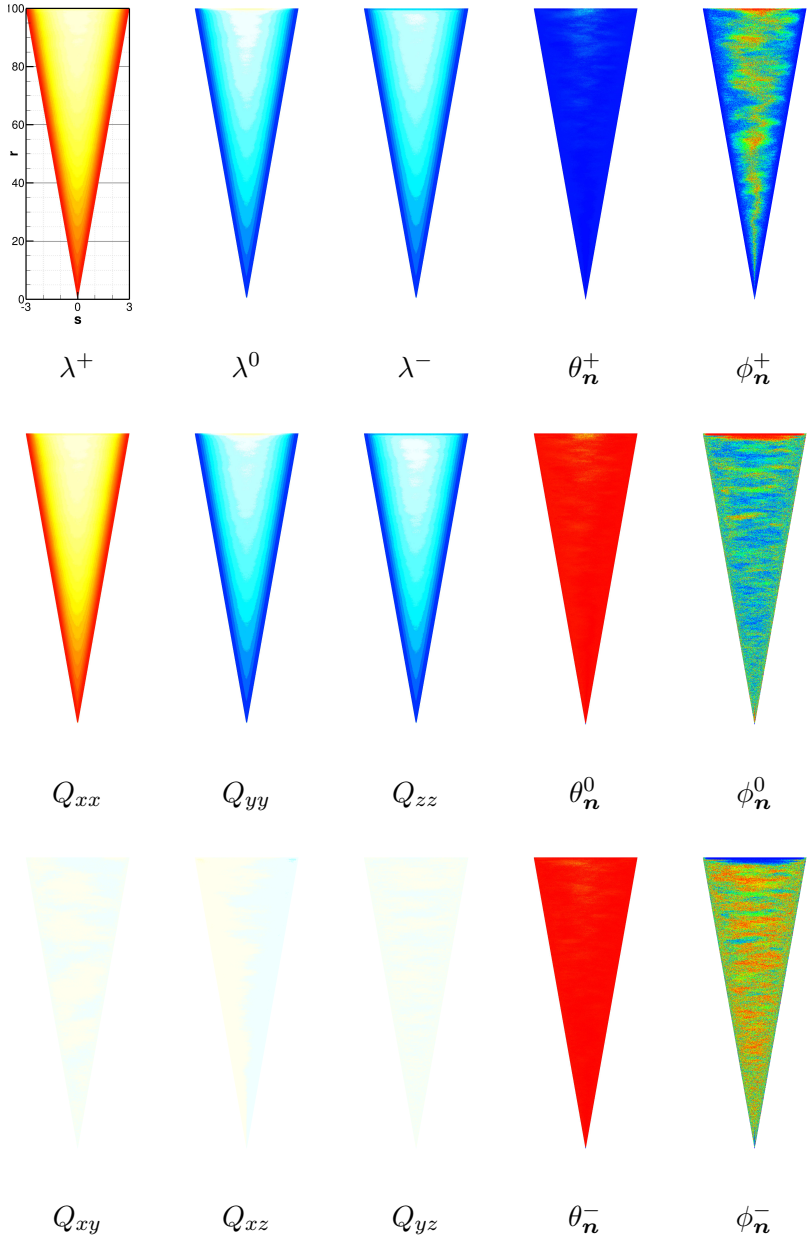

Figure 5.8: Profiles of various order parameters for $\boldsymbol{n}_\mathrm{c} = \hat{\boldsymbol{x}}$ at the $\rho_\mathrm{bulk} D^3 = 3.75$ state point. Data is plotted for each eigenvalue, λ^γ, as well as for the angles specifying each corresponding eigenvector, $\theta^\gamma_{\boldsymbol{n}}$ and $\phi^\gamma_{\boldsymbol{n}}$. Also plotted is each component of the order tensor, $Q_{\alpha\beta}$. The colour coding plots points for all of the $\lambda^\gamma, Q_{\alpha\beta}$ according to -0.5 blue, -0.25 cyan, 0 white, 0.5 yellow, 1 red. The coding for the $\theta^\gamma_{\boldsymbol{n}}, \phi^\gamma_{\boldsymbol{n}}$ is 0° blue, 22.5° cyan, 45° green, 67.5° yellow, 90° red.

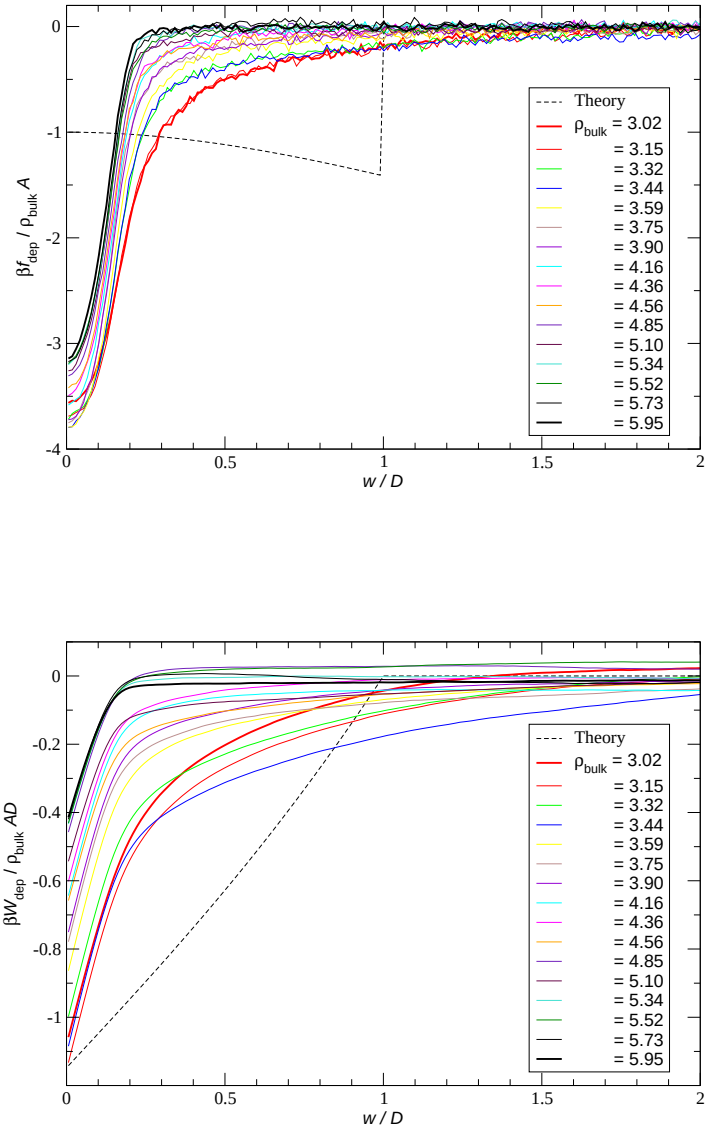

Figure 5.9: The depletion force, f_{dep}, and depletion potential, W_{dep}, per unit area against wall separation, w, for the $\boldsymbol{n}_{\text{c}} = \hat{\boldsymbol{x}}$ wedge. The theoretical prediction from a first-order virial expansion, given by eqns (5.2), varies between state points by only a factor of ρ_{bulk}, hence the $1/\rho_{\text{bulk}}$ multiplier allows data from all simulated state points to be present alongside a single dataset for the theoretical results.

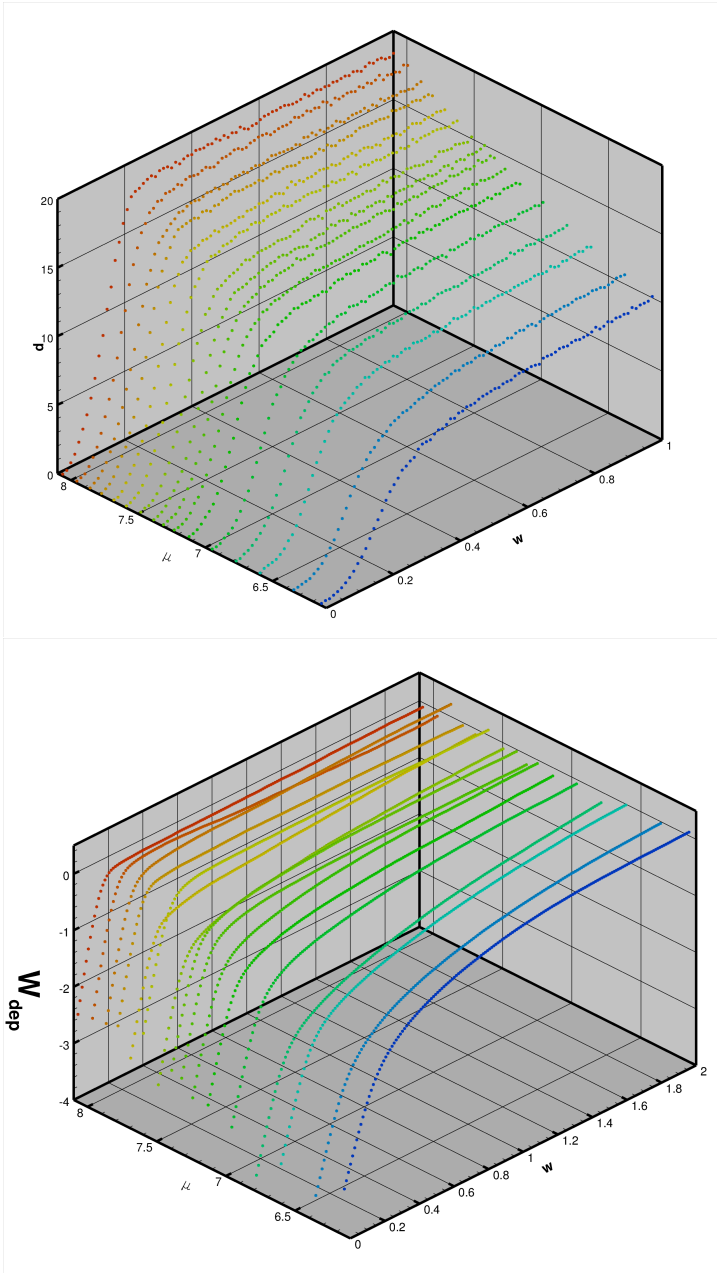

Figure 5.10: The pressure from wall contact, P, along with depletion potential, W_{dep}, each plotted against chemical potential, μ, and wall separation, w, from the $\boldsymbol{n}_{\text{c}} = \hat{\boldsymbol{x}}$ wedge, with units such that $k_{\text{B}}T = D = 1$. Each plot is colour coded according to chemical potential, with $\mu = 6$ blue, 8.2 red, and the colours cyan, green and yellow present at uniform intervals in between.

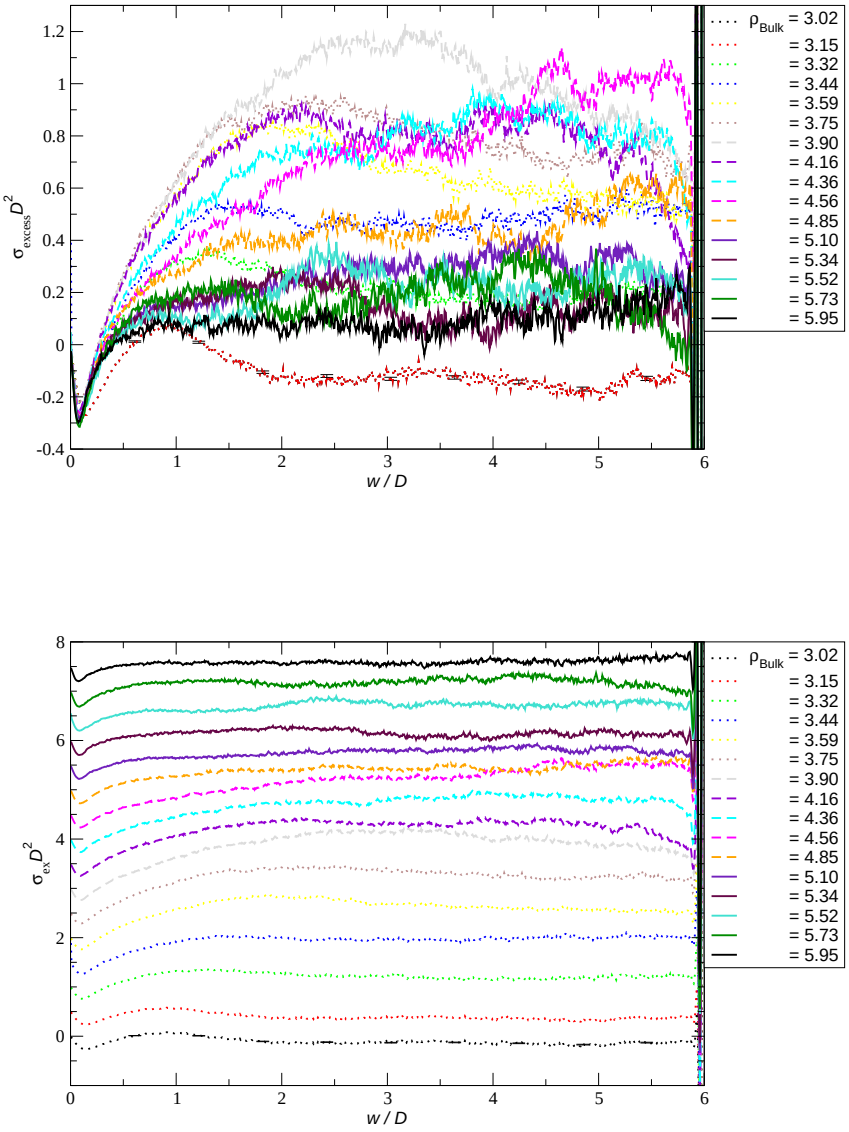

Figure 5.11: Profiles of the number of adsorbed particles per unit area, σ_{ex}, between parallel walls of separation w for each state point in the $\boldsymbol{n}_{\text{c}} = \hat{\boldsymbol{x}}$ wedge. Both plots contain the same data, with the sets in the lower graph each separated by an additional 0.5 units in the vertical direction. Typical error bars are plotted for the lowest density curve.

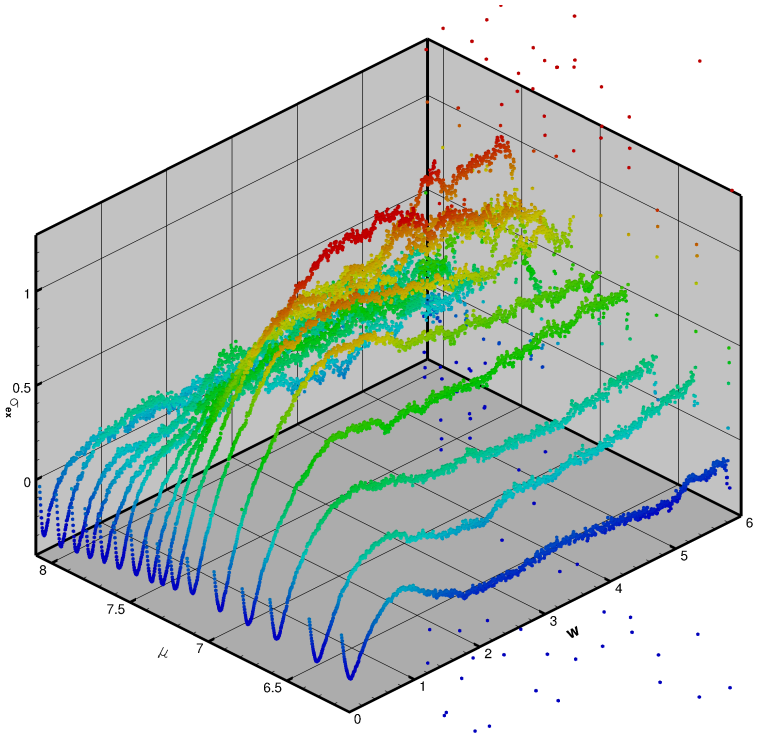

Figure 5.12: The number of adsorbed particles between the walls, σ_{ex}, per unit area as a function of wall separation, w, and chemical potential, μ, for $\boldsymbol{n}_{\text{c}} = \hat{\boldsymbol{x}}$. The plot is colour coded according to adsorption, with $\sigma_{\text{ex}}D^2 = -0.2$ blue, 1.1 red, and the colours cyan, green and yellow present at uniform intervals in between.

wedge (far from the walls) contains an extensive region with $\lambda^0 \approx 0$, corresponding to the isotropic phase. The wedge is large enough for this region to resemble the bulk. For regions close to the homeotropic-inducing side walls (within $\approx D$), λ^0 becomes negative corresponding to a wall-induced nematic, with the degree of alignment increasing as the wall is approached. There is a layer close to the planar-inducing end wall that also deviates from the isotropic phase. Near the centre of the end wall (away from the corners), λ^0 takes a positive value, signifying a planar surface phase. The corners of the wedge also exhibit a strong nematic, with the director normal to the side walls and in the plane of the end wall, due to interaction with both types of wall. Between the corners and the centre of the end wall, an intermediate phase is present with an angular distribution between that typical of a planar phase and that of a nematic, leading λ^0 to vary accordingly, passing through $\lambda^0 = 0$.

As the bulk density increases, the wall-stabilised nematic layers near the side walls increase in thickness as the interaction becomes more long-ranged, causing the isotropic region to reduce in size, until it disappears at around $\rho_{\text{bulk}} D^3 = 4.16$ as the nematic consumes all but the very end of the box. The planar phase persists in the end wall surface layer up until this density, at which the centre of the layer contains the intermediate phase with $\lambda^0 \approx 0$. Further increase in the chemical potential causes the nematic region to increase in order parameter, as well as allowing nematic phase to occupy that prestigious layer near the end wall.

Examination of the profiles of the director angles supports these observations. Deep into a bulk isotropic phase, in which all solid angles are available as directors, $\cos\theta_{\boldsymbol{n}}$ and $\phi_{\boldsymbol{n}}$ will each vary uniformly, showing a texture of colours in the plots. For the planar phase, with directors confined roughly in the xy-plane, $\theta_{\boldsymbol{n}}$ should vary uniformly, with $\phi_{\boldsymbol{n}}$ being close to $\pi/2$ or $3\pi/2$ when $\theta_{\boldsymbol{n}}$ is significantly different from 0 or π, and will be poorly defined otherwise, leading to fluctuation. For low density, $\theta_{\boldsymbol{n}}$ shows n to be aligned close to $\pm\hat{\boldsymbol{x}}$ (and thus roughly along the side wall normal) within the wall-induced nematic and the outer limits of the isotropic phase, with considerable variation of $\theta_{\boldsymbol{n}}$ toward the centre of the isotropic where the director is undefined. There is also fluctuation in the layer toward the end wall, where the planar phase preferrs directors roughly equally in the xy-plane (the plane of the wall). As the isotropic and planar phases fade with increasing chemical potential, this variation diminishes and the profiles approach $\theta_{\boldsymbol{n}} = 0$ or π everywhere as the nematic (with $n \approx \pm\hat{\boldsymbol{x}}$) dominates the entire wedge.

For $\phi_{\boldsymbol{n}}$, one can see from the plots that the z-direction is preferred relative

to the y- near the side walls, due to the wall normals having a small but significant component in z, despite the normals being close to $\pm\hat{\boldsymbol{x}}$. There is significant variation throughout the isotropic region, with two slightly different regimes seemingly present. Toward the end of the wedge, where the separation is large enough for centre of the isotropic region to be more than $2D$ from the side walls, there seems to be slightly more tendency within the central region to have director components in the $\pm z$-direction. It is interesting to note that this region seems similar in size and position to the region in which $\theta_{\boldsymbol{n}}$ shows the director to no longer be roughly along $\pm\hat{\boldsymbol{x}}$ for the same state point, suggesting that the side wall interaction affects the ill-defined director observed in the isotropic until reaching this region. Examining the layer near the end wall, the fluctuation is heavily peaked toward tendency in the $\pm y$-direction, as is expected for the planar phase. As the bulk density increases, firstly that central isotropic region which was unlike its surroundings diminishes and becomes more like the surrounding phase. Then, as the bulk isotropic-nematic transition is approached, $\phi_{\boldsymbol{n}}$ begins to take similar values within local clusters in the isotropic as the director is beginning to become more well-defined. These clusters seem to keep growing larger up to around $\rho_{\text{bulk}}D^3 = 4.16$, the state point at which the nematic phase consumes the central (formerly isotropic) region, and above this density they remain fairly consistent in size. At the end wall, the central part of the planar surface region, favouring components in the $\pm y$-direction, seems to roughly decrease in width as density increases up to $\rho_{\text{bulk}}D^3 = 4.36$ (the state point at which the surface layer is absorbed into the nematic). For subsequently higher densities, the centre of the nematic within $\approx 10D$ to $20D$ of the end wall shows vague preference toward $\pm\hat{\boldsymbol{y}}$, with other regions showing such a tendency present in other fluctuating regions of the wedge, away from the side walls.

The density profiles for $\boldsymbol{n}_{\text{c}} = \hat{\boldsymbol{x}}$ for a range of state points are given in Figure 5.4. For each state point, There is a very narrow low-density layer close to each homeotropic-inducing side wall, characteristic of platelets due to the exclusion of any platelet not possessing an orientation exactly along the wall normal. There will then be a peak in density a small distance ($< D/2$) from the wall, due to the accumulation of a large number of platelets all roughly oriented along the wall normal. Near the end wall, the density increases sharply up to wall contact, due to a dense layer of planar surface or wall-stabilised nematic phase. Due to the size of our wedge, far from all of the walls there will be a central region with properties similar to the bulk fluid, hence $\rho_{\text{ex}} \approx 0$. In the low bulk density limit, the side wall density peak

is small but abrupt, and situated at a perpendicular distance of $D/2$ from each wall. We observe such a case for $\rho_{\text{bulk}}D^3 = 3.02$, due to the interaction of the wall with the central region, which is in the low-density isotropic phase, meaning that many molecules are not well aligned with the wall normal, and hence are excluded at a distance well away from the surface. As the bulk density increases, the wall-induced nematic phase gains stability and more molecules are able to attain a position closer to the wall, causing the peak to broaden and move closer to the surface. The central region of the fluid, with $\rho_{\text{ex}} \approx 0$, shrinks noticably as the bulk density for the isotropic-nematic transition is approached, due to the interaction with the boundaries causing the phase profile to differ from the phase of the bulk fluid, whether that be isotropic or nematic. Increasing bulk density far from the transition point, the wedge attains a fully nematic phase profile, with the wall interactions becoming less significant as the order parameter increases everywhere. This allows the central region with $\rho_{\text{ex}} \approx 0$ to counter its earlier contraction, expanding with a boundary increasingly closer to the wall with increasing ρ_{bulk}.

In order to confirm this observed phase behaviour, profiles were produced and examined for a multitude of quantities based on the order tensor. Although unnecessary to publish all of the plots produced, Figure 5.8 shows profiles of most of the quantities in order to illustrate the amount of data gathered and processed, and allows the reader to see all of the order parameters in one figure for the state point exhibiting the largest range of phase behaviour, which is $\rho_{\text{bulk}}D^3 = 3.75$ for the $\boldsymbol{n}_{\text{c}} = \hat{\boldsymbol{x}}$ wedge. By first examining the eigenvalues of the order tensor, one can confirm the presence of a uniaxial nematic phase throughout most of the wedge, evidenced by a significant positive value for λ^+ along with similar and significantly negative values for λ^0 and λ^-. There is a region, away from the side walls and nearer the end of the wedge, for which the middle eigenvalue ≈ 0, as is the case for a wide central portion of the end wall surface layer. Upon observing that the other eigenvalues ≈ 0 in that region away from the walls, one can conclude that there is an isotropic phase present. For the layer close to the end wall, a positive value is present for the top eigenvalue, telling us that there is tendency toward some director, $\boldsymbol{v}^+$. A distinctly negative bottom eigenvalue in the region suggests a tendency away from another director, $\boldsymbol{v}^-$. The noticable difference between λ^0 and λ^- allows one to determine that there is indeed a degree of biaxiality, hence the phase of this central portion of the end wall surface layer corresponds to an angular distribution between that of a uniaxial nematic along $\boldsymbol{v}^+$ and a planar phase directed away from $\boldsymbol{v}^-$.

The individual elements of the order tensor can also be informative in their undiagonalised form. Looking at those plotted in Figure 5.8, one can see that each of the diagonal elements are roughly equal in the central region far from the walls, telling us that none of the coordinate axes are preferred by the director over the others, a characteristic of the isotropic phase. In the nematic region, Q_{xx} strongly resembles λ^+, whereas Q_{yy} and Q_{zz} are very similar and resemble both λ^0 and $\lambda^-.\lambda^+$, meaning that $\hat{\boldsymbol{x}}$ would be a reasonable approximation for the $\boldsymbol{v}^+$, with $\hat{\boldsymbol{y}}$ and $\hat{\boldsymbol{z}}$ each being equally suitable possibilities for $\boldsymbol{v}^0$ or $\boldsymbol{v}^-$. In the end wall surface layer, Q_{xx}, Q_{yy} and Q_{zz} are very close to λ^+, λ^0 and λ^- respectively, making clear the most suitable choices for the eigenvectors as $\boldsymbol{v}^+, \boldsymbol{v}^0, \boldsymbol{v}^- = \hat{\boldsymbol{x}}, \hat{\boldsymbol{y}}, \hat{\boldsymbol{z}}$ to describe this intermediate between the uniaxial nematic and planar phase. The off-diagonal components of $Q_{\alpha\beta}$ are very close to 0 everywhere, suggesting that there is no region in which there is a strong tendency to align along any vectors that are not roughly parallel to one of the coordinate axes. The profile of Q_{xz} changes sign as the arc distance coordinate changes from $s < 0$ to $s > 0$, due to the influence of the wall normals, each inclined slightly from $\hat{\boldsymbol{x}}$ by opposing angles in the xz-plane.

Looking at the angles of the eigenvectors, $\theta^+_{\boldsymbol{n}}$ shows that $\boldsymbol{v}^+$ is close to $\hat{\boldsymbol{x}}$ throughout the wedge, with a slight deviation toward the centre of the region close to the end wall. $\phi^+_{\boldsymbol{n}}$ shows a tendency toward the y-direction within in this region due to the planar phase, preference to the z-direction near the side walls, and shows fluctuation throughout the rest of the system. The other eigenvectors are then contained in the plane normal to $\boldsymbol{v}^+$, and near the end wall $\boldsymbol{v}^0$ is close to the y-direction (with small deviation into the x-direction due to the planar anchoring), with $\phi^-_{\boldsymbol{n}}$ showing a lack of tendency for the director to align toward $\hat{\boldsymbol{z}}$. For the rest of the system, both $\boldsymbol{v}^0$ and $\boldsymbol{v}^-$ fluctuate considerably, $\phi^0_{\boldsymbol{n}}$ and $\phi^-_{\boldsymbol{n}}$ showing a slight preference for director alignment toward $\hat{\boldsymbol{z}}$, as is expected for a small isotropic region within wall-stabilised nematic that is influenced by wall normals with small but considerable components in the z-direction.

Figure 5.9 gives the depletion force and potential measured in the $\boldsymbol{n}_{\mathrm{c}} = \hat{\boldsymbol{x}}$ wedge, as a function of arc wall separation, w, for all of the observed state points. The functions are only plotted up to $w/D = 2$ in order to provide emphasis on the region in which the most variation is observed. As expected, depletion was observed to be a short-ranged interaction, with convergence to zero of the force and potential observed well within the range of wall separations available in the wedge ($0 < w/D < 6$). Looking at the depletion force plot, $f_{\mathrm{dep}}(w)$ seems to vary

roughly continuously from the lowest bulk densities to the highest, with $f_{\text{dep}}(w)$ shrinking in the w-direction to become shorter ranged. This is to be expected, since an increasingly sharp orientational distribution will be present between the walls, leading to the projection of each molecule in the direction of the wall normal being narrower, thus reducing the wall separation required to exclude each molecule.

In the limit of a perfectly-aligned system of platelets, the pair-excluded volume converges to 0, as do in fact all of the virial coefficients beyond first order. This fluid will then exhibit the properties of an ideal gas, meaning that the entropy of the fluid between the walls will not differ from that in the bulk, leading the depletion force and potential to also converge to 0. Considering this limit, it seems reasonable that, for increasing density (and thus increasing order parameter), the depletion force per particle should reduce in magnitude, eventually converging to 0, and this reduction is what is observed in Figure 5.9. The first order virial prediction does not vary between state points apart from by a factor of ρ_{bulk}, therefore our variation in $f_{\text{dep}}(w)$ is due to that of the higher-order virials, and it is interesting to note that this variation is not abrupt once we divide by density. This is despite the properties of the fluid undergoing considerable changes between some of the state points, such as phase transitions and local restructuring.

The plot for $W_{\text{dep}}(w)$ does not show as promising evidence of a continuum of functions for a range of densities, due to the potential possessing a greater susceptibility to statistical error. The relationship compared to the one-body prediction however, is more asthetically supportive, with increasingly low-density curves seeming to give an extrapolation to $w = 0$ that is increasingly close to that predicted by the first-order theory. This is not entirely surprising; the theory does not account for particle-particle interactions, hence better approximating systems with low densities and sharply peaked orientational distributions. The latter will be true to the greatest extent for small separations in which any molecule not oriented close to the wall normal is excluded by the wall.

We have calculated the depletion force from measurements of the pressure exerted by the fluid on the side walls of the wedge for a variety of state points. Figure 5.10 shows the value of this pressure against wall separation and chemical potential. As could be inferred from the earlier depletion force plot, for the $\boldsymbol{n}_{\text{c}} = \hat{\boldsymbol{x}}$ wedge, it is more clear in this figure that increasing the chemical potential produces a pressure profile that becomes shorter-ranged and converges more quickly to a higher bulk value for the pressure. Also contained in this figure is a plot for the value of

the depletion potential, without the factor of $1/\rho_{\text{bulk}}$, against separation and chemical potential. This shows that, although the shape changes significantly, the values of the function $W_{\text{dep}}(w)$ as $w \to 0$ change gently and actually generally reduce in magnitude as the state points become more dense. This is also not entirely surprising; depletion is a measure of the difference in entropy between the fluid between the walls and that in the bulk. For the higher densities, the walls simply provide support for the nematic phase, which is already stable in the bulk, whereas at lower densities, the walls invoke another phase, the wall-stabilised nematic. Therefore it follows that the entropy difference should be lower for the higher bulk densities, thus the work done in bringing the surfaces together (equal to the depletion potential) is less significant.

Another quantity that provides a measure for the difference between properties exhibited by the platelets within our wedge system and those within a bulk phase at the same state point is the adsorption, σ_{ex}, which is plotted in Figures 5.11 and 5.12. For $\boldsymbol{n}_{\text{c}} = \hat{\boldsymbol{x}}$, each state point shows similar behaviour down to a minimum value of $\sigma_{\text{ex}} D^2 = -0.3$ at around $w/D = 0.1$, and then the profiles deviate. The number of adsorbed molecules between the walls beyond the bulk for $w/D < 0.1$ being roughly independent of state point is interesting in of itself, as it requires the average density within this thin slit to increase along with the density of the corresponding bulk phase. The adsorption profile seems to generally increase up to $\rho_{\text{bulk}} = 3.90$ or $\mu = 7.25$, and then reduces from $\rho_{\text{bulk}} = 4.16$ or $\mu = 7.33$ onwards, which is the range of densities for which no isotropic phase is present. In between the two mentioned state points, the isotropic-nematic transition takes place in the bulk at around $\rho_{\text{bulk}} = 4$.

At each state point, the region near the centre of the wedge, far from the walls, achieves reasonably uniform density and order profiles, and this is the region that best represents the bulk phase. Note that not only will the chemical potential in this region be equal to that of the bulk, but also the ideal and excess contributions, μ_{id} and μ_{ex}, will be similar to the bulk values. For the other regions, the density and orientational profiles will results in a different value for each of μ_{id} and μ_{ex} from that in the bulk, but they will combine to give the same $\mu = \mu_{\text{id}} + \mu_{\text{ex}}$ as the bulk.

Taking this behaviour into account, it is reasonable to expect, for bulk densities leading up to the isotropic-nematic transition, the wedge will contain an isotropic bulk region surrounded by a wall-induced nematic at higher density than this bulk phase, leading to increasingly large values for the wall adsorption. Once all of this

central region has been absorbed into the wall-stabilised nematic, the density difference between the phase near the walls and the central region, now also a nematic, will have decreased due to the phase transition, yielding smaller values for the adsorption, yet still $\sigma_{\text{ex}} > 0$ for the most part due to the nematic near the walls being more ordered and dense than that within the central region.

5.3.2 $\boldsymbol{n}_\mathrm{c} = \hat{\boldsymbol{y}}$

The phase behaviour observed in the other wedge geometries is somewhat richer than that for $\boldsymbol{n}_\mathrm{c} = \hat{\boldsymbol{x}}$ discussed in section 5.3.1. This is due to the extremely strong anchoring of platelets in the plane of the side walls which exclude only the centre of each molecule, but the director within this plane can be allowed to take any distribution without compromising the anchoring, hence $\boldsymbol{n}$ may fluctuate uniformly or be perturbed into some profile by interaction with neighbouring geometries.

The phase behaviour present in the $\boldsymbol{n}_\mathrm{c} = \hat{\boldsymbol{y}}$ wedge for a range of state points can be determined from the plots in Figures 5.14–5.16, showing profiles of the middle eigenvalue and angles of the director. It again unnecessary to show plots from every state point. As one would expect for a low-density case, the profiles for the middle eigenvalue for the less dense state points show that the centre of the wedge (far from the walls) contains an extensive region with $\lambda^0 \approx 0$, corresponding to the isotropic phase. Once again the system is large enough for this region to resemble the bulk. For regions close to the planar-inducing side walls (within $\approx D$), λ^0 becomes negative corresponding to a wall-induced planar phase, with the degree of alignment increasing as the wall is approached. The end wall also induces planar anchoring, and λ^0 exhibits similar behaviour close to the end wall. There is an exception, however, near the corners of the wedge, for the regions within the interaction distance of more than one wall, in which a nematic phase is present with $\boldsymbol{n}$ oriented along the line of intersection between the planes of the two walls, which for this geometry is always the $\pm y$-direction. One could expect this phase to also be present near the vertex of the wedge, but no such nematic is observed, suggesting that the wall separation near the vertex is sufficiently small to allow molecules sufficient freedom to follow any director in the yz-plane. Between the corners and the regions near the walls supporting a planar phase, the intermediate phase between nematic and planar is present, leading λ^0 to vary accordingly, passing through $\lambda^0 = 0$.

As the bulk density increases, the wall interaction becomes more long-ranged, the isotropic region reduces in size, and the planar phase seems to occupy the centre of the wedge by $\rho_\mathrm{bulk} D^3 = 4.36$, with λ^0 small but noticably greater than zero. As this changeover in the central region is taking place, a thin layer a short distance (several platelet diameters) from the end wall begins a transition into the nematic phase. This region thin layer is first noticable at $\rho_\mathrm{bulk} D^3 = 3.92$ and seems to increase in size only gradually up to $\rho_\mathrm{bulk} D^3 = 4.46$, at which another slightly

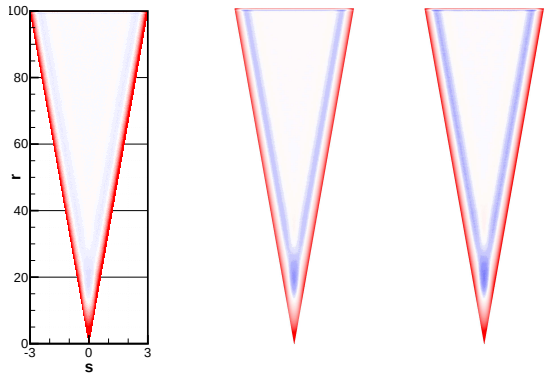

$\rho_{\text{bulk}}D^3 = 2.60$ 2.89 3.21

3.52 3.92 4.48

4.81 5.22 5.38

Figure 5.13: Profiles of $\rho_{\text{ex}}(\boldsymbol{r})$ for $\boldsymbol{n}_{\text{c}} = \hat{\boldsymbol{y}}$. The colour coding plots points as follows; $\rho_{\text{ex}}D^3 = -2$ blue, 0 white, 8 red.

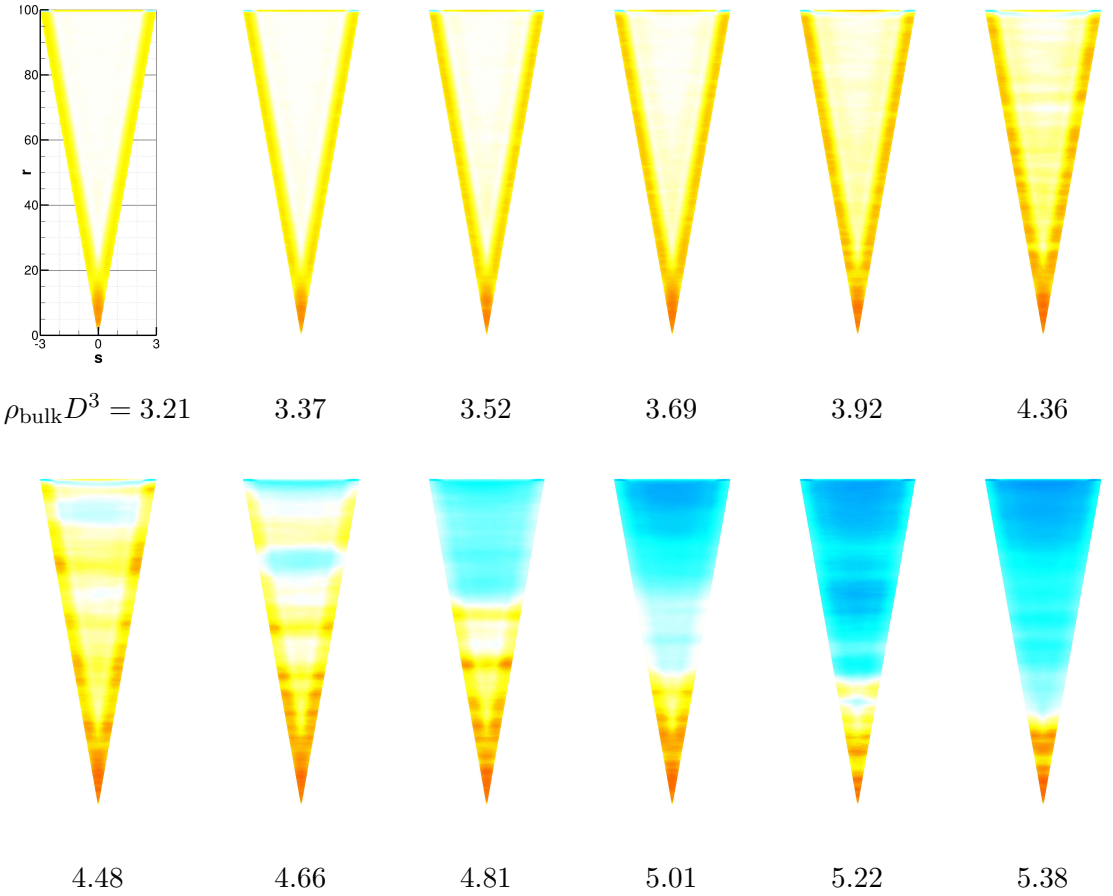

Figure 5.14: Profiles of λ^0 for $\boldsymbol{n}_{\text{c}} = \hat{\boldsymbol{y}}$. The colour coding plots points as follows; $\lambda^0 = -0.5$ blue, -0.25 cyan, 0 white, 0.125 yellow, 0.25 red.

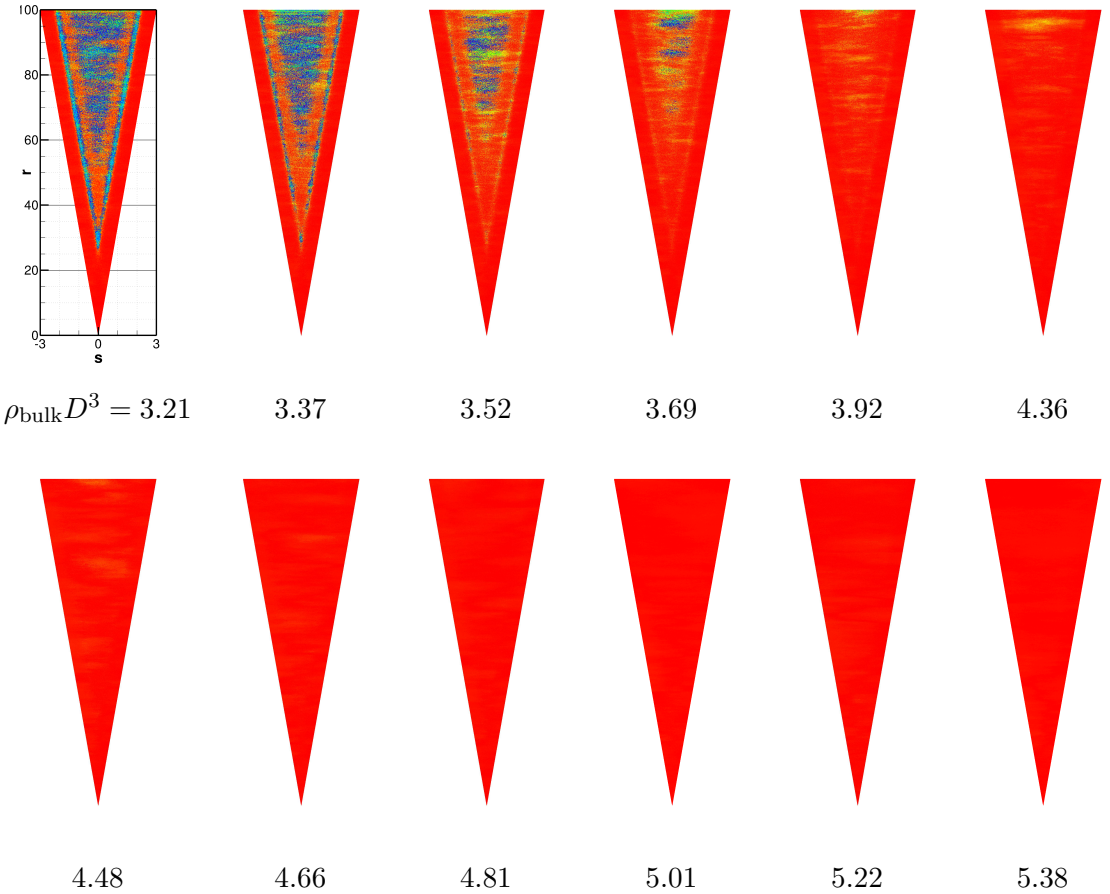

Figure 5.15: Profiles of $\theta_{\boldsymbol{n}}$ for $\boldsymbol{n}_{\text{c}} = \hat{\boldsymbol{y}}$. The colour coding plots points as follows; $\theta_{\boldsymbol{n}} = 0°$ blue, 22.5° cyan, 45° green, 67.5° yellow, 90° red.

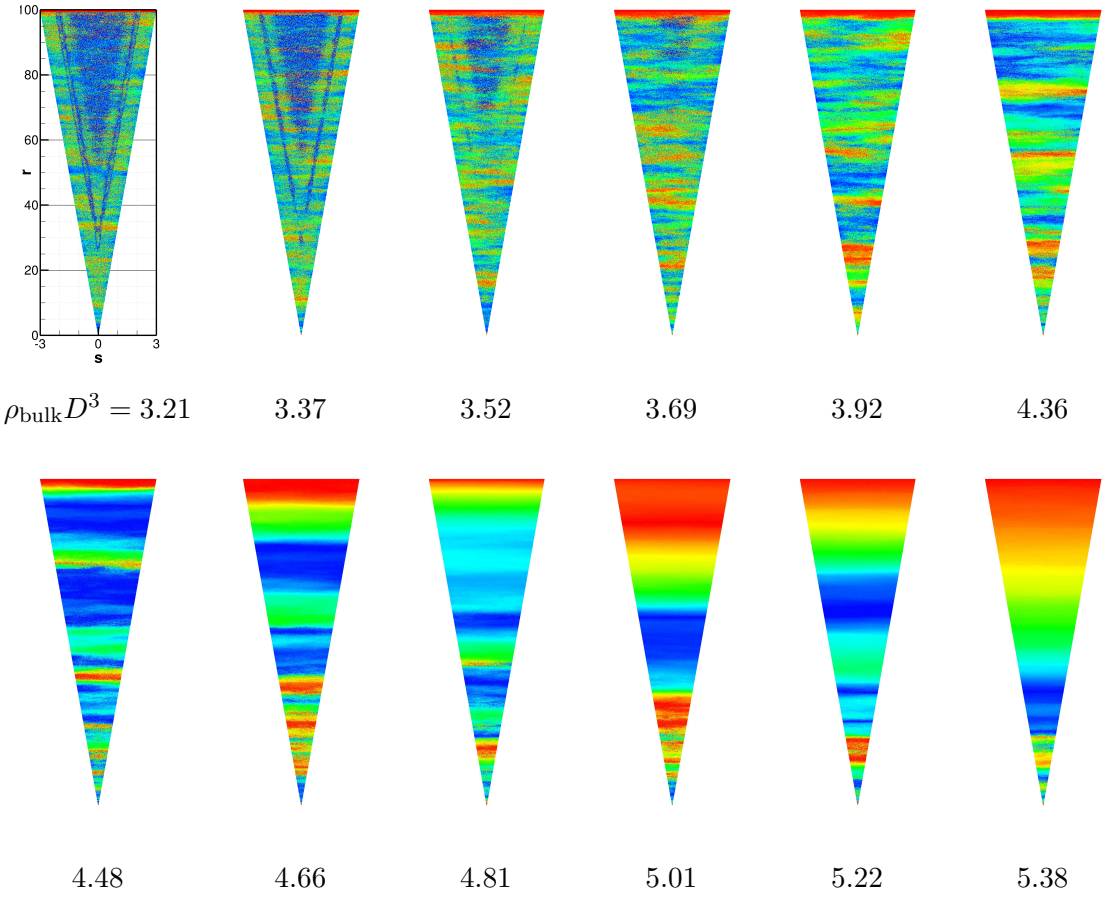

Figure 5.16: Profiles of $\phi_{\boldsymbol{n}}$ for $\boldsymbol{n}_{\text{c}} = \hat{\boldsymbol{y}}$. The colour coding plots points as follows; $\phi_{\boldsymbol{n}} = 0°$ blue, 22.5° cyan, 45° green, 67.5° yellow, 90° red.

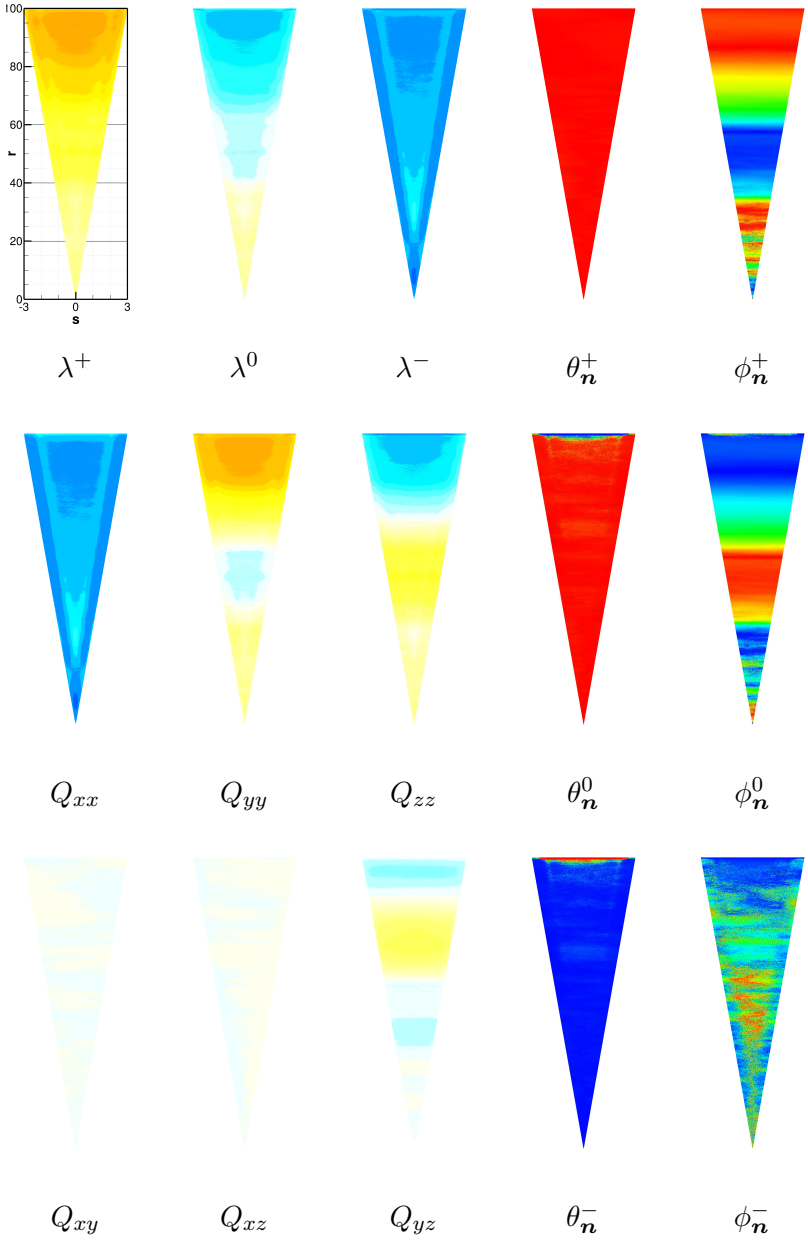

Figure 5.17: Profiles of various order parameters for $\boldsymbol{n}_{\mathrm{c}} = \hat{\boldsymbol{y}}$ at the $\rho_{\mathrm{bulk}} D^3 = 5.01$ state point. Data is plotted for each eigenvalue, λ^γ, as well as for the angles specifying each corresponding eigenvector, $\theta^\gamma_{\boldsymbol{n}}$ and $\phi^\gamma_{\boldsymbol{n}}$. Also plotted is each component of the order tensor, $Q_{\alpha\beta}$. The colour coding plots points for all of the $\lambda^\gamma, Q_{\alpha\beta}$ according to -0.5 blue, -0.25 cyan, 0 white, 0.5 yellow, 1 red. The coding for the $\theta^\gamma_{\boldsymbol{n}}, \phi^\gamma_{\boldsymbol{n}}$ is 0° blue, 22.5° cyan, 45° green, 67.5° yellow, 90° red.

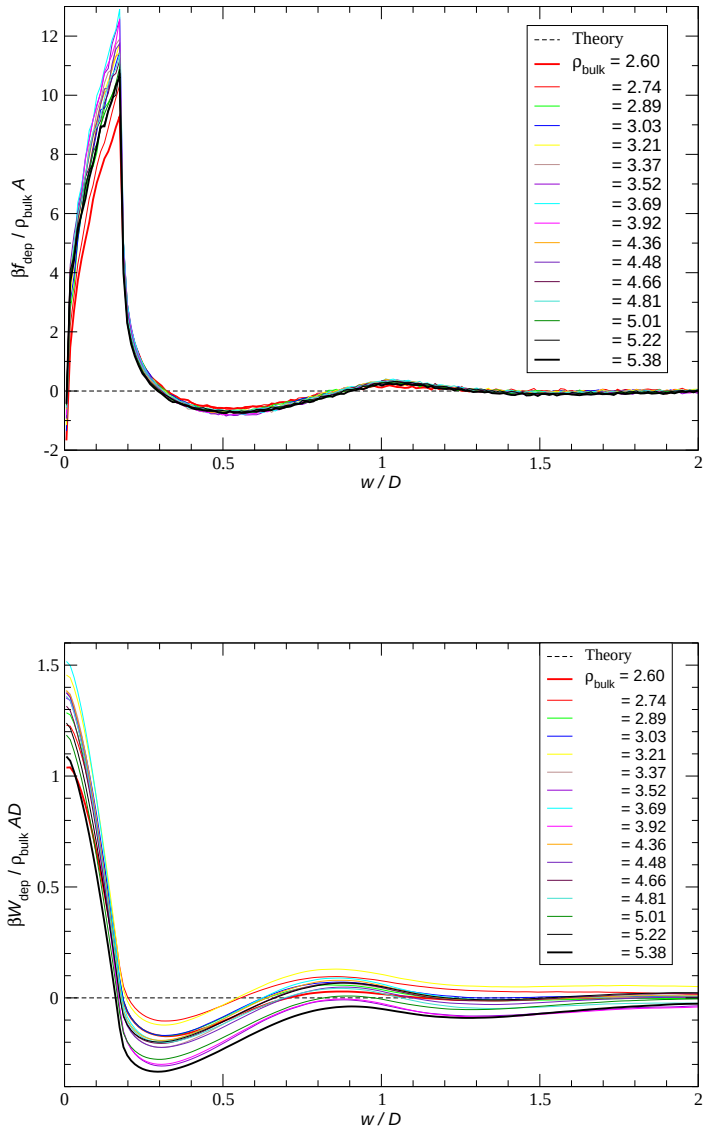

Figure 5.18: The depletion force, f_{dep}, and depletion potential, W_{dep}, per unit area against wall separation, w, for the $\boldsymbol{n}_{\text{c}} = \hat{\boldsymbol{y}}$ wedge. The theoretical prediction from a first-order virial expansion reduces to zero, and the $1/\rho_{\text{bulk}}$ multiplier is present for comparison with Figures 5.9 and 5.27.

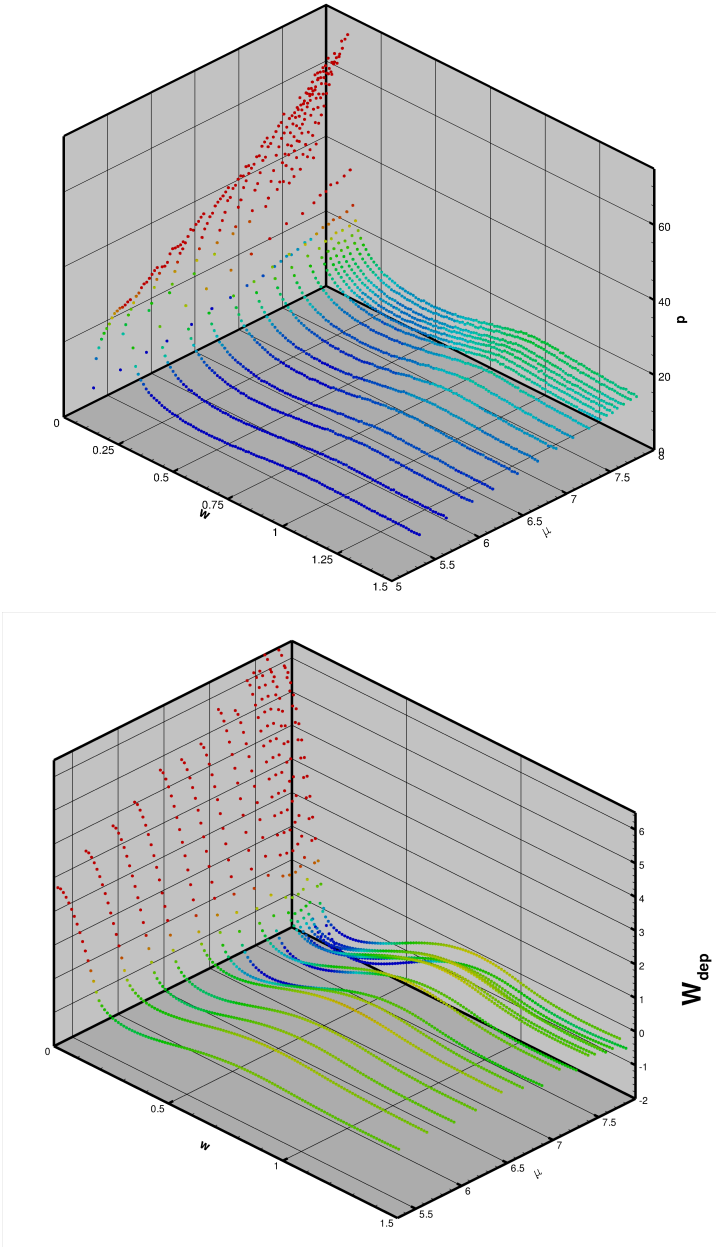

Figure 5.19: The pressure from wall contact, P, along with depletion potential, W_{dep}, each plotted against chemical potential, μ, and wall separation, w, from the $\boldsymbol{n}_{\mathrm{c}} = \hat{\boldsymbol{y}}$ wedge, with units such that $k_{\mathrm{B}}T = D = 1$. The pressure plot is colour coded according to P, with $P = 10$ blue, 30 red. The potential plot is colour coded according to W_{dep}, with $W_{\mathrm{dep}} = -1$ blue, 1 red. For both graphs, the colours cyan, green and yellow are present at uniform intervals in between blue and red.

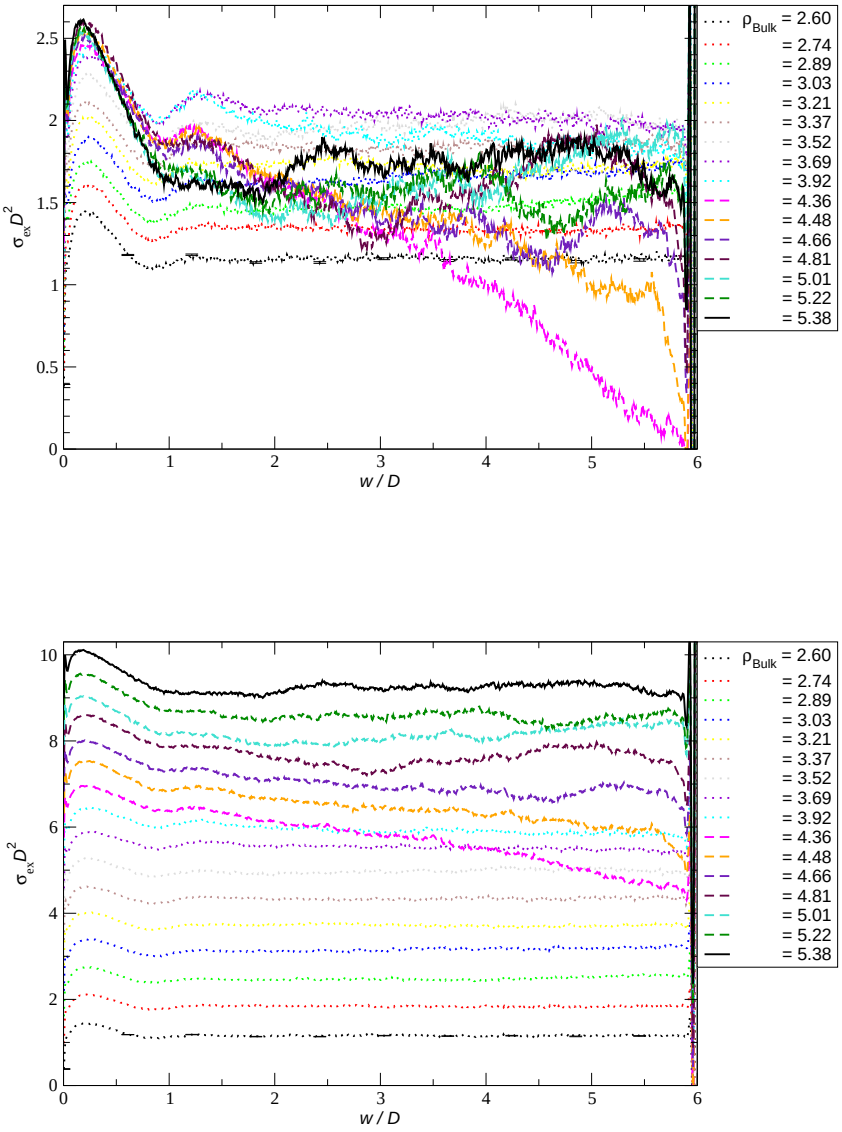

Figure 5.20: Profiles of the number of adsorbed particles per unit area, σ_{ex}, between parallel walls of separation w for each state point in the $\boldsymbol{n}_{\mathrm{c}} = \hat{\boldsymbol{y}}$ wedge. Both plots contain the same data, with the sets in the lower graph each separated by an additional 0.5 units in the vertical direction. Typical error bars are plotted for the lowest density curve.

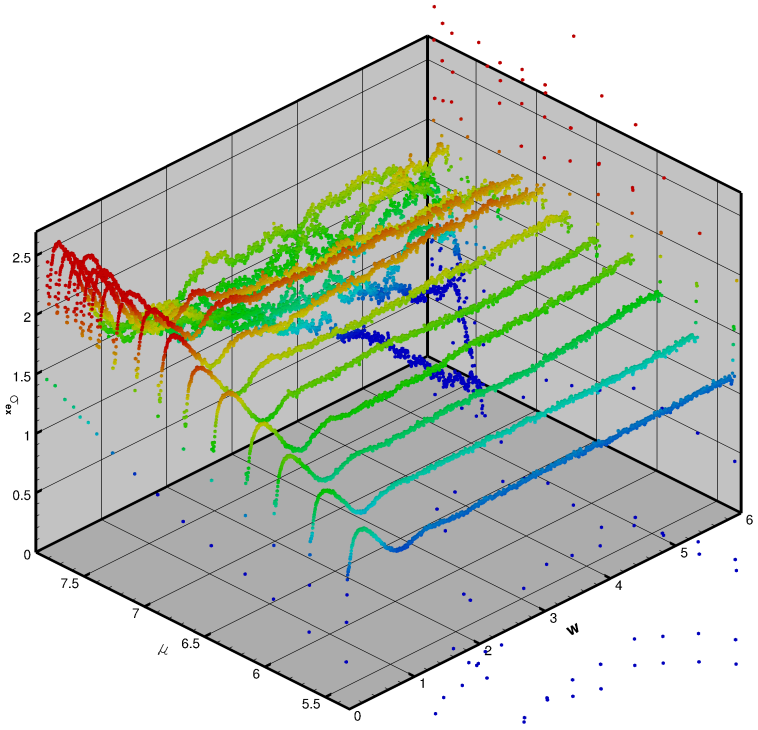

Figure 5.21: The number of adsorbed particles between the walls, σ_{ex}, per unit area as a function of wall separation, w, and chemical potential, μ, for $\boldsymbol{n}_{\text{c}} = \hat{\boldsymbol{y}}$. The plot is colour coded according to adsorption, with $\sigma_{\text{ex}}D^2 = 1$ blue, 2.2 red, and the colours cyan, green and yellow present at uniform intervals in between.

nematic region, being around 5 or 10 diameters farther from the end wall and $\approx 10D$ in thickness, also develops. These two nematic regions appear to combine together at the following density, $\rho_{\text{bulk}}D^3 = 4.66$, as the nematic consumes the region that had occupied the end wall, leading to a completely nematic region near the end wall that is around $10D$ thick in the centre (away from the side walls). This state point has yet another sizable nematic region at a wall separation of around $w = 2$, and $\lambda^0 \approx 0$ within a number of regions, both forming a side wall surface layer surrounding the nematic regions and near the central regions (where arc distance $s \to 0$) away from the side walls, showing the intermediate phase between planar and nematic. The profile of the middle eigenvalue contains a number of significant portions of the wedge for which λ^0 is less than or approximately 0 at bulk densities from $\rho_{\text{bulk}}D^3 = 4.46$ onwards, signalling the beginning of a transition from a planar-dominated wedge to one supporting the nematic phase. As the bulk density increases in excess of $\rho_{\text{bulk}}D^3 = 4.66$, the nematic phase is contained in a large single region, reaching from the end wall and increasing in thickness, except for $\rho_{\text{bulk}}D^3 = 4.66$ where an additional small pocket of nematic seems to form inside the planar-dominated region at a separation between 1 and 2 platelet diameters.

Examination of the profiles of the director angles supports these observations, and is useful in the distinction between the isotropic phase and the intermediate between the planar and nematic phases. As previously discussed, $\cos\theta_{\boldsymbol{n}}$ and $\phi_{\boldsymbol{n}}$ will each vary uniformly deep into a bulk isotropic phase, showing a texture of colours in the plots. For the planar phase, with directors confined roughly in the yz-plane, $\theta_{\boldsymbol{n}}$ should tend to 0 or π, with $\phi_{\boldsymbol{n}}$ varying uniformly as orientations within the plane are sampled with equal probability. Should the planar phase contain directors mostly in the xy-plane, $\theta_{\boldsymbol{n}}$ should vary uniformly, with $\phi_{\boldsymbol{n}}$ being close to $\pi/2$ or $3\pi/2$ when $\theta_{\boldsymbol{n}}$ is significantly different from 0 or π, and will be poorly defined otherwise, leading to fluctuation. For low density, $\theta_{\boldsymbol{n}}$ shows n to be contained closely within the yz-plane for the planar phase close to the side walls (within $\sim D$). The rest of the system exhibits considerable variation of the director, with three distinct regions with a slightly different distribution of $\theta_{\boldsymbol{n}}$ present. These consist of a thin layer (thickness of order $D/4$), in contact with the planar phase near the side walls, then a thicker layer ($\sim D$ in thickness) slightly further from the walls, and finally a central region far from the side walls. The central region seems to exhibit roughly uniform variation in $\theta_{\boldsymbol{n}}$, with the thicker layer possessing more of a tendency away from $\theta_{\boldsymbol{n}} = 0$ and, curiously, the thin layer preferring to take values of $\theta_{\boldsymbol{n}}$ slightly closer to

0. The distribution of $\theta_{\boldsymbol{n}}$ present in the few diameters closest to the end wall also seems to be slightly different from that in the central isotropic region. For increasing density, the thicker layer, with small preference away from $\theta_{\boldsymbol{n}} = 0$, favours directors that are increasingly different from the x-axis and spreads to mostly encompass the thin outer layer, whilst causing the central isotropic region to shrink, and by $\rho_{\text{bulk}} D^3 = 3.92$ the distribution of directors in the system is strongly biased away from the x-direction.

The plots for $\phi_{\boldsymbol{n}}$ seem to show regimes for the director separated into regions that match those mentioned for $\theta_{\boldsymbol{n}}$. Near the end wall for all densities, we see that $\boldsymbol{n}$ preferrs y-contributions, as is expected due to the planar surface phase present. For low-density, the directors in the planar phase near the side walls show variation within local clusters, and with a distribution slightly biased toward the y-direction. In the isotropic phase, a shorter-range and more uniform fluctuation in $\phi_{\boldsymbol{n}}$ is present, as is the case for the thin layer near the planar phase. The thicker layer near the walls shows clusters sizes and director distribution similar to the planar regions. As the density is increased, these different regions gradually merge and the distribution observed for the central isotropic region seems to disappear at $\rho_{\text{bulk}} D^3 = 4.36$ The sizes of the clusters of roughly constant-$\phi_{\boldsymbol{n}}$ also seem to increase slowly with density, which seems reasonable as correlation distances should increase. By $\rho_{\text{bulk}} D^3 = 4.66$ the clusters seem to stretch across entire widths of the wedge, and such correlation in director certainly rules out the presence of any isotropic phase, despite the regions present with $\lambda^0 \approx 0$. This also tells us that the planar phase at these higher densities interacts normal to its plane of directors (the s-direction) with a considerable correlation distance, such that the directors on each side wall influence one another. As the density increases further and the nematic phase takes over the top end of the wedge, there is still fluctuation in $\phi_{\boldsymbol{n}}$ along the r-direction, but each layer of constant r looks more uniform in $\phi_{\boldsymbol{n}}$. Interestingly, the nematic-planar interfaces present in the higher-density wedge systems seem to favour an orientation along the z-axis.

The density profiles for $\boldsymbol{n}_{\text{c}} = \hat{\boldsymbol{y}}$ for a range of state points are given in Figure 5.13. For each state point, There is a narrow high-density layer close to each of the walls due to the anchoring inducing a planar phase. There will then be a local minimum in density, this low density region beginning at a distance of around $D/2$ from each wall as well as $\sim D/2$ in thickness. In the low-density limit, the density profile will be flat and the fluid properties identical to the bulk,

as in general the tendency of the molecules to accumulate near the wall is due to particle-particle interaction: there are no molecules on the other side of the wall to interact and overlap with. Near the vertex of the wedge, the density minimum is more pronounced due to interaction with the two side walls, and the range of this low-density region increases with bulk density. There is a slight decrease in density at the wall contact for the smaller wall separations (from $\approx D/2$ to $D/4$), for which molecules at each wall are forced to align with one another to prevent overlap, until the separation is small enough for any molecules present to be almost totally pretruding out of the system. The range of phase behaviour does not seem to significantly influence the structure of ρ_{ex}, although there is an interesting formation of a second low-density layer at a distance of $\sim 3D/2$ from the walls for some of the higher bulk densities.

Figure 5.17 provides a convenient example of a range of order profiles for a particular state point, from which a determination of the phases present was performed for each bulk density. From examination of the eigenvalues of the order tensor, we firstly notice that λ^- is significantly lower than 0 throughout the system, excluding the possibility of any isotropic phase. We can see that there is a large region ($\sim 30D$ in thickness) toward the end of the system that is roughly in the nematic phase, with $\lambda^+ \geq 0.5$ and $\lambda^0 \leq -0.25$. There is some biaxiality in this region, however, with λ^- being noticably different from the middle eigenvalue throughout a significant portion. There is then another region, with thickness $\sim 30D$ in the r-direction, where $\lambda^+ \geq 0.25$ and λ^0 is mostly negative but close to 0, meaning that there is a slight tendency of orientations toward $\boldsymbol{v}^+$, suggesting a nematic, but at least some of the region is in an intermediate with the planar phase, with considerable difference between the middle and bottom eigenvalues. The remaining portion of the system, toward the vertex, seems to be well within the planar surface phase, with λ^+ and $\lambda^0 > 0$ along with a significantly negative bottom eigenvalue.

Looking at the individual elements of the order tensor, it is first apparent from Q_{xx} that $\hat{\boldsymbol{x}}$ would be a suitable choice for $\boldsymbol{v}^-$, as it so closely resembles the profile of λ^-. Throughout most of the upper region, Q_{yy} most resembles the top eigenvalue with Q_{zz} showing similarity to λ^0, expecting one to find $\boldsymbol{v}^{+,-} \approx \hat{\boldsymbol{z}}, \hat{\boldsymbol{y}}$. Similarly, we would expect the director to be close to $\hat{\boldsymbol{y}}$ for the central region, leaving $\boldsymbol{v}^0$ roughly along $\hat{\boldsymbol{z}}$, and we find that either axis would be appropriate for the director in the lower region exhibiting the planar phase. From examining the yz-element of the order tensor, one can see the portions of the system for which the

y- and z- directions would not be appropriate directors, and we thus see that the director protrudes into the yz-plane away from the individual axes considerably as the upper region changes to the central region, as well as within the central region and near the interface between the central and lower regions.

Looking at the angles of the eigenvectors, $\theta^+_{\boldsymbol{n}}$ shows that the directors are closely contained within the yz-plane. and $\phi^+_{\boldsymbol{n}}$ assures that the director is roughly along the y-direction at the end of the wedge, commensurate with both end and side walls, and that the director varies rotates slowly as we move through the nematic phase, and then fluctuates more substantially in the planar phase toward the vertex. $\theta^0_{\boldsymbol{n}}$ tells us that, near the end wall, there is some tendency to orient toward the x-axis, due to the planar anchoring at the wall, and for the rest of the system $\boldsymbol{v}^0$ is also well away from $\hat{\boldsymbol{x}}$. $\phi^0_{\boldsymbol{n}}$ is then degenerate close to the end wall, and varies similarly to $\phi^+_{\boldsymbol{n}}$ otherwise. $\theta^-_{\boldsymbol{n}}$ and $\phi^-_{\boldsymbol{n}}$ inform us that the direction of least orientational preference is along $\hat{\boldsymbol{z}}$ near the end wall, due to the planar anchoring, and in the x-direction otherwise, due to planar anchoring near the side walls.

For the side walls favouring planar anchoring, it was found that more structural features were present in the depletion force and potential than for homeotropic-inducing walls, but the functions exhibited more subtle variation from one state point to another. For this type of geometry, the prediction from a first order virial expansion will be zero, as each single particle is excluded by the walls independent of its orientation, hence its range of orientations is not affected by the wall separation, hence the entropy of an individual particle is equal to that of a bulk system of equal volume. Hence any depletion potential will be a measure of the effects that the boundary conditions inflict upon the interaction profile of the fluid, unlike for the homogeneous anchoring-inducing walls, which also deplete each molecule directly.

Figure 5.18 gives the depletion force and potential measured in the $\boldsymbol{n}_{\mathrm{c}} = \hat{\boldsymbol{y}}$ wedge, as a function of arc wall separation, w, for all of the observed state points. Once again, the functions are only plotted up to $w/D = 2$ in order to provide emphasis on the region in which the most variation is observed. As expected, depletion was observed to be a short-ranged interaction, with convergence to zero of the force and potential observed well within the range of wall separations available in the wedge ($0 < w/D < 6$). The qualitative features of the depletion force and potential from each state point are the same. For the force, decreasing w/D from 2, the value of $f_{\mathrm{dep}}(w)$ is negligible, until climbing to a small positive peak in the region of $w/D = 1$, before crossing $f_{\mathrm{dep}} = 0$ around $w/D = 0.9$ and continuing down to a

minimum near $w/D = 0.5$. The force then increases and passes through zero once more at $w/D = 0.3$, before abruptly increasing and reaching a sharp maximum in the region of $w/D = 0.2$, with any further decrease in w causing f_{dep} to reach 0 again close to $w = 0$. This means that parallel walls of this kind, when coming together in a large system of platelets held at the chemical potential of any of our state points, would first experience a small outward thermodynamic force, and after passing $w/D \approx 0.9$ would be forced inwards, until meeting a more formidable force as their separation were to become less than $\sim 0.3D$.

The corresponding potential, $W_{\text{dep}}(w)$, as the surface separation becomes $< 2D$, takes a value reasonably close to 0, passes a very gently peak at around $w/D = 0.8$ to 0.9, then falls to a negative minimum value in the region of $w/D = 0.3$, before then assuming a relatively large maximum as w tends to 0. As we obtain the depletion potential from an integral of f_{dep}, a function containing mild statistical noise, $W_{\text{dep}}(w)$ is highly susceptable to fluctuation and the plot shows a spread of datasets with the same basic shape. There does appear to be an approximate general behaviour with increasing bulk density, with the less dense state points possessing a mildly positive value for W_{dep} at $w/D > 0.5$ and a shallower negative minimum near $w/D = 0.3$, whereas the minimum is deeper at the higher densities, with W_{dep} increasing from the minimum to only small negative values with increasing w. This range of behaviour for the potential means that, for high density, the surfaces will be have a small energy incentive to come firstly within $w/D = 2$ of each other, and then a far deeper minimum is available for the walls to come together to $w/D = 0.3$, a separation that should be fairly stable, with significantly decreasing separation then meeting a large energy barrier. For the lowest densities, the minimum is of similar depth to the height of the small barrier encountered in bringing the surfaces from far apart to $w/D \approx 0.8$, meaning that the thermal fluctuations required for the surfaces to become far separated again after having been brought together to within the minimum will not be large compared to those that were required to overcome the barrier in bringing them together initailly. For the force plot, the datasets for the different state points seem to varymore continuously than for the potential, with the lower density functions tending to be compressed toward zero compared to those for higher density, which generally have taller peaks and deeper minima.

It is not unreasonable to expect the depletion effects to become more significant with increasing density, as the separation of the walls should perturb the density and order profiles to a greater degree due to simply more molecules being

present to interact with one another, and in the limit of low density the depletion interaction will converge to 0 as described by the first order virial expansion. As the first order virial prediction does not vary between state points, our variation in $f_{\mathrm{dep}}(w)$ is due to that of the higher-order virials, and it is interesting to note that once again this variation is not so abrupt once we divide by density. This is despite the properties of the fluid undergoing considerable changes between some of the state points, such as phase transitions and local restructuring.

We have calculated the depletion force from measurements of the pressure exerted by the fluid on the side walls of the wedge for a variety of state points. Figure 5.19 shows the value of this pressure against wall separation and chemical potential. For the $\boldsymbol{n}_{\mathrm{c}} = \hat{\boldsymbol{y}}$ wedge, increasing the chemical potential produces a pressure profile that converges to a higher bulk value for the pressure. Also contained in this figure is a plot for the value of the depletion potential, without the factor of $1/\rho_{\mathrm{bulk}}$, against separation and chemical potential. This shows that, although the shape remains fairly consistent, the values of the peak in $W_{\mathrm{dep}}(w)$ as $w \to 0$ increase, and the value of the minimum becomes more negative.

The number of particles adsorbed between the walls per unit area in excess to the bulk, σ_{ex}, for $\boldsymbol{n}_{\mathrm{c}} = \hat{\boldsymbol{y}}$ is plotted in Figures 5.20 and 5.21. Each state point shows posesses a maximum value at around $w/D = 0.2$, with a small narrow additional local maximum as w approaches 0 for densities above $\rho_{\mathrm{bulk}} = 2.74$. For densities up to 3.69, the peak value increases fairly consistently and σ_{ex} also posesses a minimum just before $w/D = 1$, before climbing to a roughly flat value for the rest of the wedge. At $\rho_{\mathrm{bulk}} = 3.86$, the peak value shows only a slight increase, with a decrease in σ_{ex} beyond about $w/D = 1.4$. Each subsequent increase in bulk density causes only a small change in the peak, and at $\rho_{\mathrm{bulk}} = 4.36$ the adsorption after the initial peak suddenly exhibits a steadily declining value as w increases, reaching 0 as the separation approaches $w/D = 6$. Any further increase in density causes σ_{ex} after the peak to recover some of the former flat shape and increase, with considerable fluctuation.

The sudden change in shape of the density profile not only occurs at the first state point with density above that of the bulk isotropic-nematic phase transition, but also takes place within the same sytem ($\rho_{\mathrm{bulk}} = 4.36$) in which the isotropic phase has been absorbed by the planar phase, and the nematic is still restricted to a fine layer near the end wall. Prior to this density, there is a central isotropic region with a denser planar phase surrounding it, leading to a fairly constant value

to the adsorption as the central isotropic region is similar to the bulk and the planar region contributes to the adsorption. At this transitioning density, the bulk fluid undergoes a transition into the nematic phase, the fluid in the wedge falls mostly into the planar phase, and the gradient in the adsorption plot tells us that this planar phase assumes a density increasingly close to that of the bulk nematic with increasing wall separation. The subsequent increases in density, with the transition within the wedge from the planar to nematic phase for increasingly large portions near the end wall, comes an increase in adsorption, implying that the nematic formed in the wedge is more dense than that found in the bulk phase, and $\sigma_{\text{ex}}(w)$ seems to depend strongly on these phase changes.

5.3.3 $\boldsymbol{n}_{\mathrm{c}} = \hat{\boldsymbol{z}}$

The phase behaviour observed in the $\boldsymbol{n}_{\mathrm{c}} = \hat{\boldsymbol{z}}$ wedge geometry is similar to the $\boldsymbol{n}_{\mathrm{c}} = \hat{\boldsymbol{y}}$ case, discussed in section 5.3.2, due to both systems posessing large side walls that favour planar anchoring. The phase behaviour for this wedge may be determined by examination of the various order profiles, a procedure described in detail in sections 5.3.1 and 5.3.2, hence it is unnecessary to give as much detail here. The significant difference in these order profiles is that the end wall, inducing homeotropic anchoring in its vicinity, gives rise to a wall-stabilised nematic present, with $\boldsymbol{n} \approx \hat{\boldsymbol{z}}$, at the end wall for all state points. In such a nematic, λ^0 is negative, $\theta_{\boldsymbol{n}}$ will be close to $\pi/2$ or $3\pi/2$ and $\phi_{\boldsymbol{n}}$ tends to 0 or π.

For low density, an isotropic phase is present in a central region of the wedge, far from the walls, with $\lambda^0 \approx 0$ and significant fluctation in the angles of the director. Near the side walls, a planar phase is present, with λ^0 positive and directors close to the yz-plane. The wall-stabilised nematic is present only within a thin layer $\sim D$ of the end wall, including the corners of the system, and an intermediate phase with $\lambda^0 \approx 0$ is found when inspecting around $D - 2D$ from the corners along the side walls.

As the density is increased, the isotropic phase shrinks as the range of the wall interactions increase, with the isotropic phase disappearing completely at $\rho_{\mathrm{bulk}} D^3 = 4.36$, with the wedge filled with a small layer of wall-stabilised nematic ($< 5D$ in thickness) near the end wall along with an extensive region in the planar phase. Further increases in the bulk density see an increase in thickness of the nematic region, up to $\rho_{\mathrm{bulk}} D^3 = 5.03$, for which the nematic phase from the end wall somewhere near $60D$ thick. Increasing density beyond this value was not observed to cause significant increase in the size of the nematic region. One difference that can be discerned from these plots is that the director in the nematic region underwent noticably less fluctuation than observed for the $\boldsymbol{n}_{\mathrm{c}} = \hat{\boldsymbol{y}}$ geometry, suggesting the wall-stabilised nematic having a significantly longer range for the case of the end wall favouring homeotropic anchoring. As for $\boldsymbol{n}_{\mathrm{c}} = \hat{\boldsymbol{y}}$, the director seemed to show a general preference toward $\hat{\boldsymbol{z}}$ close to the nematic-planar interface.

Figure 5.8 gives profiles of various order parameters for $\boldsymbol{n}_{\mathrm{c}} = \hat{\boldsymbol{z}}$ at the $\rho_{\mathrm{bulk}} D^3 = 4.78$ state point. The eigenvalues of the order tensor show a nemtic region near the end wall that is around $40D$ in thickness with noticable biaxiality, particularly in the lower 25 diameters, which contains some of the intermediate

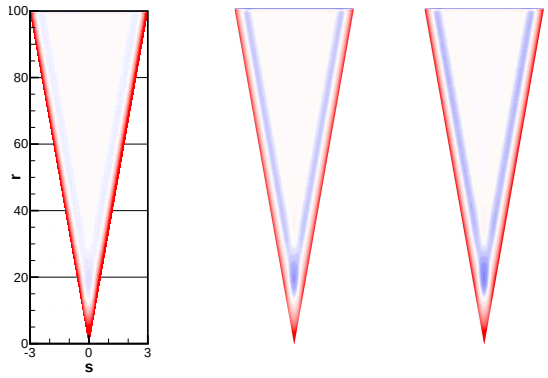

$\rho_{\text{bulk}}D^3 = 2.59$ 2.88 3.20

3.55 3.86 4.48

4.78 5.16 5.45

Figure 5.22: Profiles of $\rho_{\text{ex}}(\boldsymbol{r})$ for $\boldsymbol{n}_{\text{c}} = \hat{\boldsymbol{z}}$. The colour coding plots points as follows; $\rho_{\text{ex}}D^3 = -2$ blue, 0 white, 8 red.

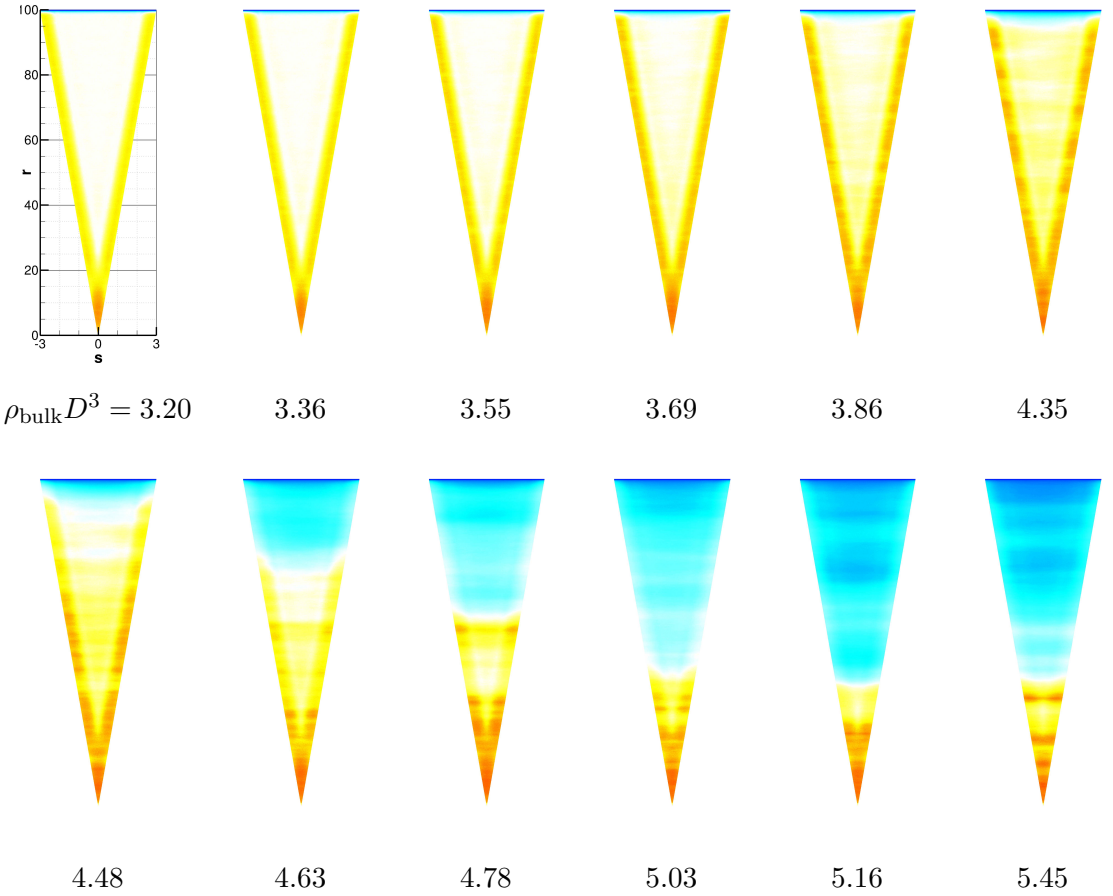

Figure 5.23: Profiles of λ^0 for $\boldsymbol{n}_{\text{c}} = \hat{\boldsymbol{z}}$. The colour coding plots points as follows; $\lambda^0 = -0.5$ blue, -0.25 cyan, 0 white, 0.125 yellow, 0.25 red.

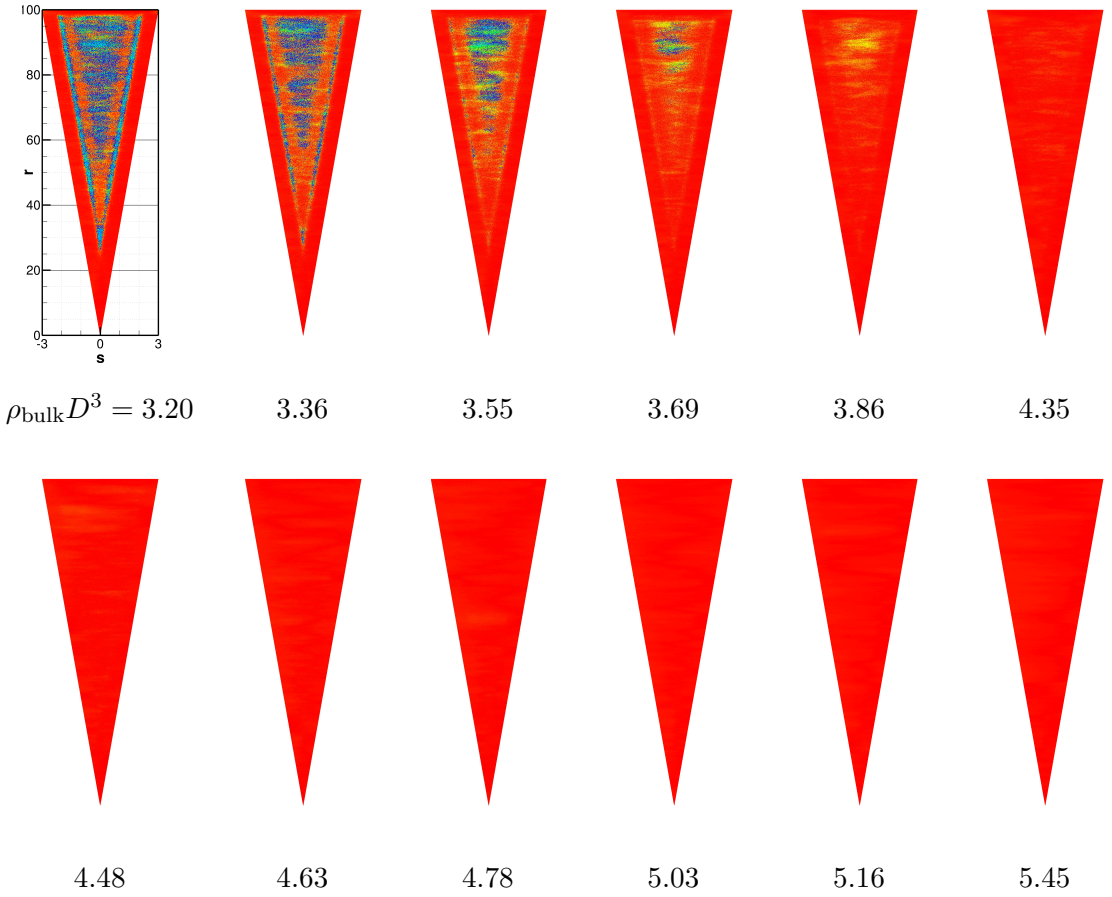

Figure 5.24: Profiles of $\theta_{\boldsymbol{n}}$ for $\boldsymbol{n}_{\text{c}} = \hat{\boldsymbol{z}}$. The colour coding plots points as follows; $\theta_{\boldsymbol{n}} = 0°$ blue, 22.5° cyan, 45° green, 67.5° yellow, 90° red.

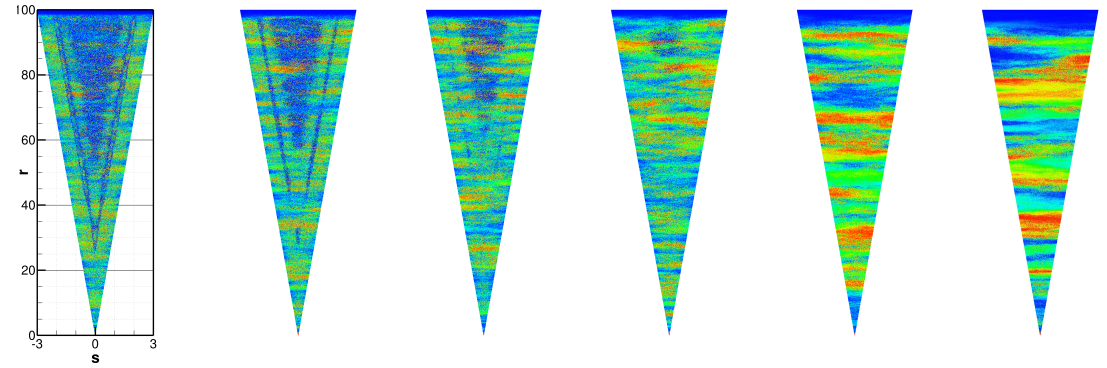

$\rho_{\text{bulk}}D^3 = 3.20$ 3.36 3.55 3.69 3.86 4.35

4.48 4.63 4.78 5.03 5.16 5.45

Figure 5.25: Profiles of $\phi_{\boldsymbol{n}}$ for $\boldsymbol{n}_{\text{c}} = \hat{\boldsymbol{x}}$. The colour coding plots points as follows; $\phi_{\boldsymbol{n}} = 0°$ blue, 22.5° cyan, 45° green, 67.5° yellow, 90° red.

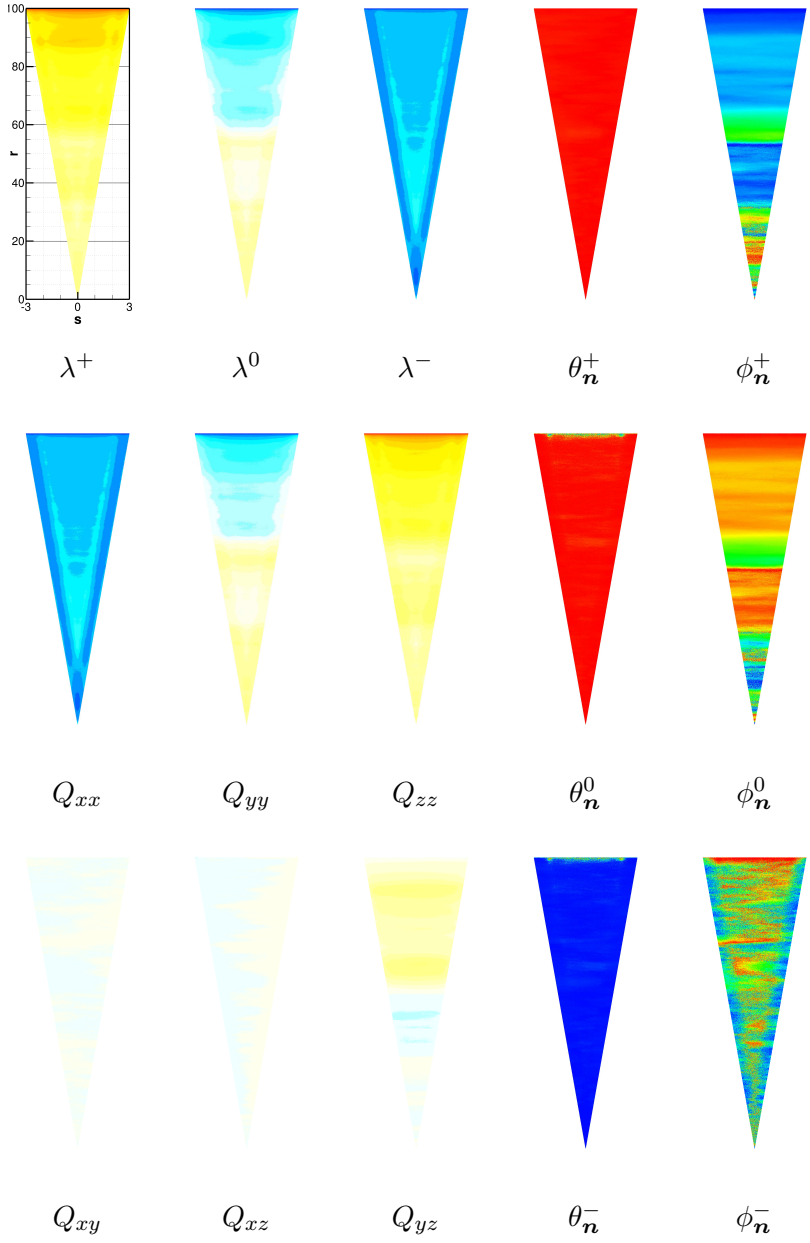

Figure 5.26: Profiles of various order parameters for $\boldsymbol{n}_{\mathrm{c}} = \hat{\boldsymbol{z}}$ at the $\rho_{\mathrm{bulk}} D^3 = 4.78$ state point. Data is plotted for each eigenvalue, λ^γ, as well as for the angles specifying each corresponding eigenvector, $\theta^\gamma_{\boldsymbol{n}}$ and $\phi^\gamma_{\boldsymbol{n}}$. Also plotted is each component of the order tensor, $Q_{\alpha\beta}$. The colour coding plots points for all of the $\lambda^\gamma, Q_{\alpha\beta}$ according to -0.5 blue, -0.25 cyan, 0 white, 0.5 yellow, 1 red. The coding for the $\theta^\gamma_{\boldsymbol{n}}, \phi^\gamma_{\boldsymbol{n}}$ is 0° blue, 22.5° cyan, 45° green, 67.5° yellow, 90° red.

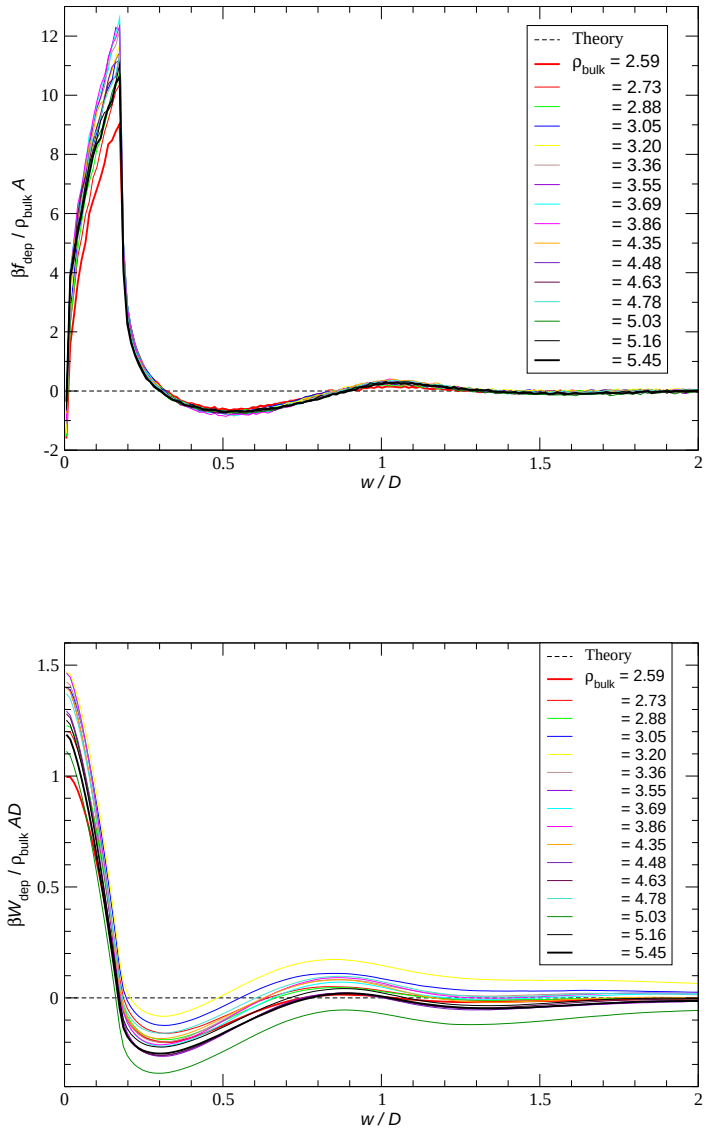

Figure 5.27: The depletion force, f_{dep}, and depletion potential, W_{dep}, per unit area against wall separation, w, for the $\boldsymbol{n}_{\text{c}} = \hat{\boldsymbol{z}}$ wedge. The theoretical prediction from a first-order virial expansion reduces to zero, and the $1/\rho_{\text{bulk}}$ multiplier is present for comparison with Figures 5.9 and 5.18.

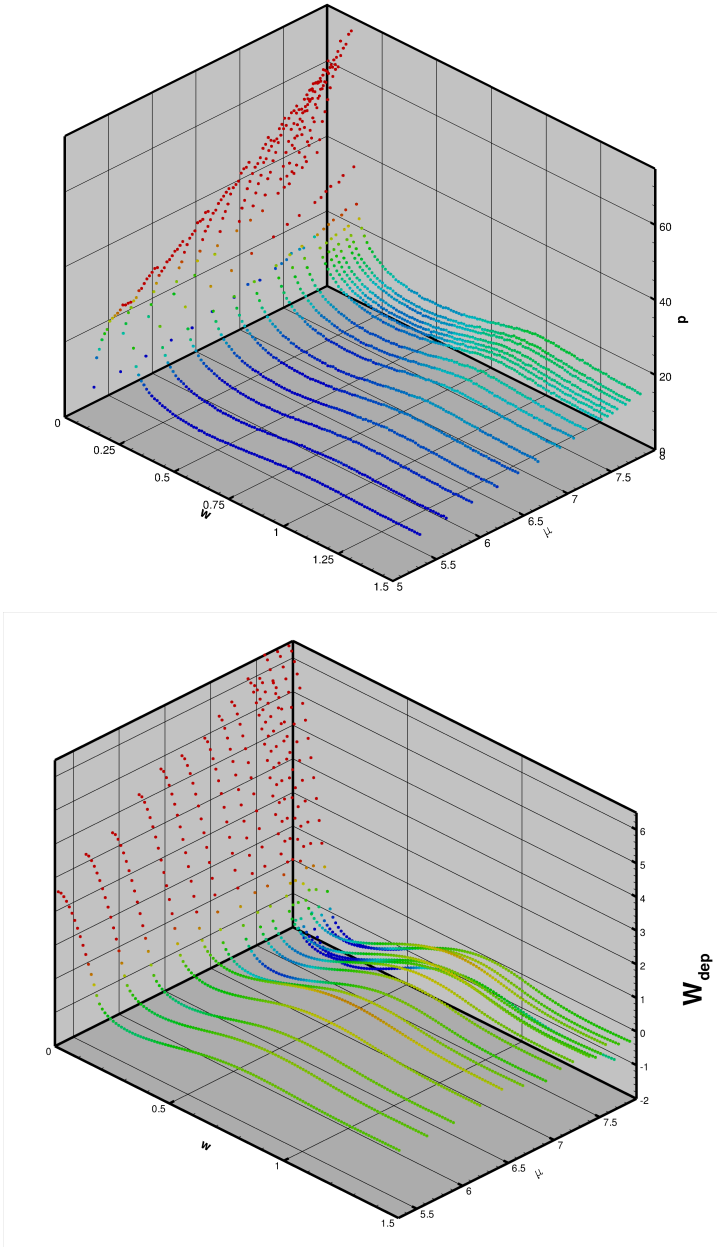

Figure 5.28: The pressure from wall contact, P, along with depletion potential, W_{dep}, each plotted against chemical potential, μ, and wall separation, w, from the $\boldsymbol{n}_{\text{c}} = \hat{\boldsymbol{z}}$ wedge, with units such that $k_{\text{B}}T = D = 1$. The pressure plot is colour coded according to P, with $P = 10$ blue, 30 red. The potential plot is colour coded according to W_{dep}, with $W_{\text{dep}} = -1$ blue, 1 red. For both graphs, the colours cyan, green and yellow are present at uniform intervals in between blue and red.

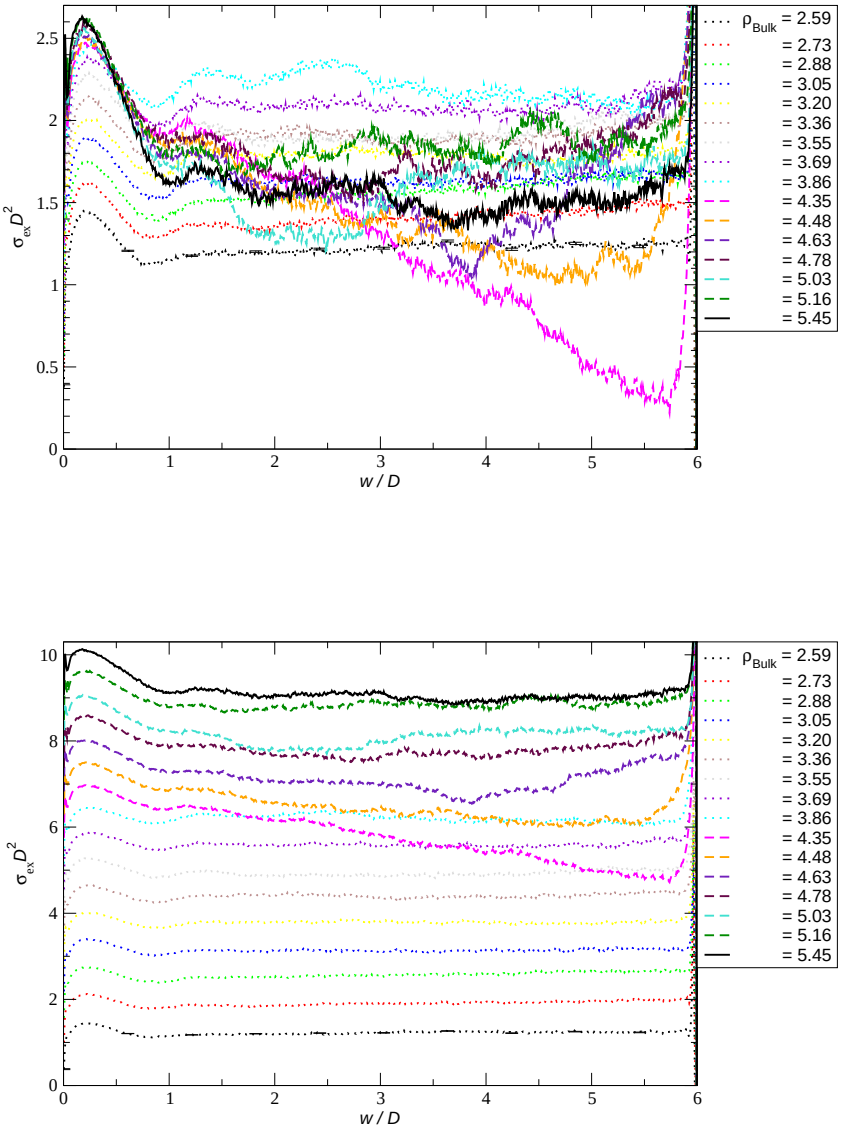

Figure 5.29: Profiles of the number of adsorbed particles per unit area, σ_{ex}, between parallel walls of separation w for each state point in the $\boldsymbol{n}_{\mathrm{c}} = \hat{\boldsymbol{z}}$ wedge. Both plots contain the same data, with the sets in the lower graph each separated by an additional 0.5 units in the vertical direction. Typical error bars are plotted for the lowest density curve.

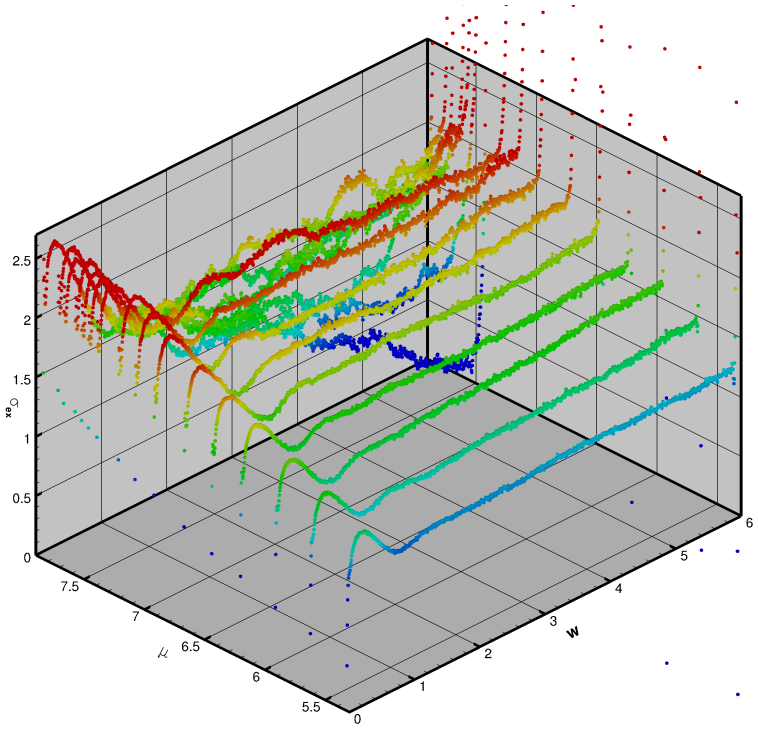

Figure 5.30: The number of adsorbed particles between the walls, σ_{ex}, per unit area as a function of wall separation, w, and chemical potential, μ, for $\boldsymbol{n}_{\text{c}} = \hat{\boldsymbol{z}}$. The plot is colour coded according to adsorption, with $\sigma_{\text{ex}}D^2 = 1$ blue, 2.2 red, and the colours cyan, green and yellow present at uniform intervals in between.

phase close to the side walls. The λ^{γ} also show the rest of the wedge to be in the planar phase. The individual elements of the order tensor show $\boldsymbol{v}^{+,0,-} \approx \hat{\boldsymbol{z}}, \hat{\boldsymbol{y}}, \hat{\boldsymbol{x}}$ to give a reasonable description of the eigenvectors, with noticable but small protrusion of the director into the yz-plane. The eigenvectors show that, near the end wall, directors are strongly preferred along the z-direction, and any directors within the xy-plane are roughly equally undesirable. They show the rest of the system to strongly favour directors in the yz-plane, with shorter-range fluctuation in the planar region that in the nematic, as would be expected.

Figure 5.22 shows the qualitative features of the density profiles to be extremely similar to those for the $\boldsymbol{n}_{\mathrm{c}} = \hat{\boldsymbol{y}}$ geometry. The exception is close to the end wall, where the homeotropic anchoring gives rise to a single, broader yet smaller peak in density near the wall.

Due to the dominance of the large side walls favouring planar anchoring, the measurements of the depletion interactions and wall adsorption are extremely similar to those for the $\boldsymbol{n}_{\mathrm{c}} = \hat{\boldsymbol{y}}$ systems, despite the slightly different phase behaviour present. Hence the same conclusions must be drawn from the data, refer to section 5.3.2 for details. The differences in the profiles are noticably greater for σ_{ex}, suggesting that adsorption is more sensitive to phase behaviour than depletion forces.

Chapter 6

Discussion

We have calculated the elastic constants of several molecular models by MC simulation. The calculation was first performed for spherocylinders by Molecular Dynamics simulation in the work of Allen and Frenkel [1988], for a system of 576 particles at three different densities in the nematic phase. This seemed like an appropriate model to check our method against, and presented an opportunity to apply modern computational power to obtain results at a wider range of densities, and at considerably larger system sizes, hence reducing finite size effects. The elastic constants obtained are in fair agreement with the literature, taking into account the computational limitations of the original work at the time of publication. The experimental determination of the elastic constants of certain disc-like particles [van der Beek et al., 2008] prompted interest in predictions from theory and simulation, so began our investigation into platelets and cut-spheres. Our results for platelets are in reasonable quantitative agreement with the experiments, as well as from those from a virial expansion truncated at sixth order [O'Brien et al., 2008]. The elastic constants of cut-spheres were then calculated, and the results for increasing thickness of the discs brought the values closer to those from the experiments, and also agree well with later experimental work [Verhoeff et al., 2009]. The behaviour of the elastic constants for the discs as thickness increases is promising; the spread of the K_α decreasing as the shape anisotropy is reduced, the datasets are fairly disparate and a continuum of behaviour looks possible.

Let us examine results of the experiments [van der Beek et al., 2008; Verhoeff et al., 2009]. The range of values for the elastic constants obtained is $K_1 = 9.0 - -26.0 \times 10^{--14}$N and $K_3 = 6.0 - -8.0 \times 10^{--14}$N for an order parameter in the range

$S \approx 0.80 - -0.85$. If one inserts estimates for $D \approx 237$nm and $k_{\mathrm{B}}T \approx 4 \times 10^{--21}$J, these correspond to reduced values of $\beta K_1 D \approx 5 - -15$ and $\beta K_1 D \approx 3.5 - -5$. The corresponding simulation results give a splay constant of $\beta K_1 D \approx 10$ for platelets, decreasing by about 10% as the thickness increases to use a cut-sphere with $L/D = 1/10$. For the bend constant, the corresponding values are $\beta K_3 D \approx 1.3$ for platelets, increasing to ≈ 2.4 for the thickest cut-sphere. For comparison, the estimated thickness of the gibbsite particles is $L \approx 18$nm, making $L/D = 0.076 \approx 1/13$. Hence the main effects of increasing the platelet thickness are to bring the value of K_3 closer to the experimentally measured range, and improve the agreement of the ratio K_1/K_3 with experiment.

This reasonable agreement in the other elastic constants allows one to make a reasonable guess as to the value of the twist elastic constant of gibbsite platelets, by assuming that the ratio $K2/K_{1,3}$ is the same as for our simulation values. Another useful guess that could be made using our results is for the range of validity of the elastic theory for each type of director distortion. If one examines figure 4.37 and decides that $\mathcal{W}_{\alpha 3}$ is roughly linear in k_3^2 for only $k_3/\gamma k_0 = 0 - -5$, then we conclude that bend distortions are elastic if the distortion takes place over lengths greater than $L_z/5$, which is less than $3D$ for that particular system. This means that the elastic theory will describe a bend distortion accurately as long as any significant change in the director takes place over lengths greater than $3D$.

There are a number of probable reasons for having only reasonable agreement with the experiments, mostly concerning the particle model. Hard interaction potentials may not be the best model for the gibbsite platelets, nor may be rigidity in the particle shape. The gibbsite platelets investigated were roughly hexagonal in shape and exhibited some noticable polydispersity, which is not accounted for in this study. Adding thickness to our model of platelets improved the agreement, but even increasing the thickness beyond that of the experimental particle does not increase the bend constant to the real value. It is unlikely that the size or shape of the systems affected the elastic constants enough to explain the discrepancy, as the fluctuation spectra exhibited a region linear in k_1^2 and k_3^2 that contained a sufficiently large number of points for a reasonable extrapolation. In the experiments, there are also gravitational and magnetic fields, and the platelets form into nematic droplets (termed "tactoids") interdispersed between isotropic regions. This inhomegenous system may not always be well described by a single bulk particle model, and perhaps a brute force way to measure this would be to simulate the actual experimental

environment, with the Frederiks transition taking place at some critical magnetic field strength, from which depends on the value of the elastic constant via an expression from a simple theoretical model. Such a study may at least test the validity of the assumptions of the theoretical model employed.

A cuboidal box with two equal long lengths may be more appropriate to calculate the director fluctuation spectra for discs, with the short box length along the induced director. This is because the more gentle structure along the k_3-direction allows one to utilise a larger cutoff, including significantly more data points along the 3-direction than along the 1-direction. This could not account for the discrepancy in the measured value of K_3, however, as this would lead to less data points being available for the fit along the 3-direction, actually *reducing* the accuracy of the bend elastic constant.

The aligning field applied to the bulk systems should not influence the values of the K_α obtained, with the elastic theory prediction of eqn (3.16) including the contribution to the energy density from the field. There was more concern over the implicit effect of the value of the field strength perturbing the orientational distribution, modifying the order parameter and elastic constants. However, some simple testing removed these concerns, noticing that $\mathcal{W}_{\alpha 3} - 2\rho SU$ remained unchanged (within statistical error) when measuring for two different field strengths at the same state point. Using Monte Carlo simulation with the aligning field will have no signifant difference to director-constrained Molecular Dynamics in determination of the elastic constants.

There are a number of theories for calculating elastic constants, based upon the work of Saupe [1960], which find that each of the elastic constants is proportional to S^2 for the case of low order parameter. This relationship was retained when the theory was generalised to include any molecular interaction by Priest [1973]. It is not entirely surprising that our elastic constants for the disc-like molecules do not obey this relationship, firstly as we have used a full nematic range, up to high values of S. These theories also employ other assumptions that are not necessarily valid for our models, such as assuming the isotropy of the pair distribution function, which is considered implausible for real nematics. Pre-transitional effects are ignored, in contradiction to the divergence of some of the elastic constants as smectic and columnar phases are entered. They utilise the mean field approximation, which neglects short-ranged correlations [Faber, 1981]. The Frank constants are parameters that, with the correct values, allow the elastic theory to be accurate over long

ranges, and the precise values will, of course, be determined by the short-ranged molecular interactions.

Though the phase behaviour of hard spherocylinders has been well categorised [Bolhuis and Frenkel, 1997], it is important to note that the interaction model in our MC simulations includes a small orienting field to restrict the director to a particular axis. This means that it was essential to check the phase behaviour of the system, to ensure that the small perturbation of the field did not alter the phase present [Martín del Río and de Miguel, 2006]. Most studies for cut-spheres have been performed on particles with $L/D \geq 1/10$, with those examining molecules with smaller values for L/D focusing on the isotropic-nematic transition [Fartaria and Sweatman, 2009]. This meant that it was essential to monitor the phase behaviour of the cut-sphere systems as well, with some of the results for the molecular models studied showing positional ordering to a considerable degree.

For cut spheres with $L/D = 1/10$, the structure factor spectrum calculated showed that the state points with densities in the range $\rho D^3 = 4$–5.2 were in the nematic phase, where the phase boundaries from the literature placed the lowest density in the isotropic phase, as well as three other state points in the coexistence regions between phases. Considering that our configurations were produced by expanding a perfectly aligned cubic lattice, it is possible that some of our lower-density systems may be in the isotropic-nematic coexistence region, however any system at a density in the nematic-columnar coexistence region would exhibit columnar ordering.

One of the more interesting features that we came across in our attempts to categorise the positionally ordered phases was the presence of order on different lattices describing distinct regions of the systems. Figure 4.5 shows a smectic phase with molecules ordered into layers that are reasonably distinct from one another. For some of the other state points, smectic phases were found with layers that were significantly interpenetrated, but with layers stacked such that the molecules would still have roughly the same correlation length between the loosely-defined layers, thus contributing to the same first order peak in the structure factor, $\tilde{g}(k_z)$. It seems likely that this corresponds to a frustrated system, where the dimensions of the simulation box are not sufficiently close to an integer number of lattice spacings preferred by the smectic phase, causing distortion of each layer in order for the phase to fit into a periodic pattern with lattice spacings close to those preferred values. This is consistent with the observations of Dominguez et al. [2002]. A

similar phenomenon is observed for the cut-spheres, with state points at densities in the columnar phase containing more than one distinct set of lattice vectors defining the intercolumnar order as one inspects along the z-direction. Again, this may be due to finite-size effects. A curious observation is the tendency of $L/D = 1/10$ cut-spheres, upon increasing density, to contain an increasing number of different sets of intercolumnar vectors in distinct regions. This suggests that the distortion free energy of the interface between regions containing different lattice vectors becomes small compared to the lattice free energy associated with having an optimal lattice separation and inclination. It is also possible that the orienting field distorts the positionally-ordered phases, as the optimal column or interlayer vector may not be along the z-axis, hence phases are forced into some other lattice that accommodates $\boldsymbol{n} \approx \hat{\boldsymbol{z}}$.

We have calculated a number of density and order profiles for systems of hard platelets in three different wedge geometries, determined the phases present within each system and calculated the depletion forces and adsorption between the side walls. It is interesting to see the dramatically different effects that different boundary conditions can have on the results for systems of platelets.

For the order profiles, considerable structure was observed, particularly for side walls that favoured planar anchoring. With so many features present in the profiles, it was necessary to be certain of good equilibration in the wedge systems, and chemical potential profiles were all observed to be roughly flat. It would be interesting to see whether any change in these profiles of μ could be seen if varying MC move sizes to ensure a move acceptance ratio close to 35% within each individual bin.

One interesting observation about the director profiles is that, in regions for which the nematic and planar phases are present (for $\boldsymbol{n}_{\mathrm{c}} = \hat{\boldsymbol{y}}, \hat{\boldsymbol{z}}$), $\phi_{\boldsymbol{n}}$ tends to be roughly constant within layers of constant r. There is then, for the nematic, rotation of the director over distances of many platelet diameters in the r-direction, and the planar phase shows shorter-range fluctuation due to the director being poorly-defined. Considering a layer of nematic between the walls, with the director near each wall roughly contained in the plane of the wall, the variation of $\boldsymbol{n}$ along the wall normal should depend on the value of the twist elastic constant, K_2. Variation in the direction of $\boldsymbol{n}$ will depend on the bend elastic constant, K_3, and the in-plane variation normal to $\boldsymbol{n}$ will depend on the splay elastic constant, K_1. The relative size of these constants, as we have calculated, is such that the expected director

variation normal to the walls will be over long length scales due to a high K_2, with the in-plane variation less energetically expensive, depending on the lower K_1 and substantially lower K_3. This expected behaviour seems to agree with the layering in our observations. It is interesting how this arguement predicts that the characteristic range of director correlation along the r-direction will depend on the orientation of the director at that value of r, with a shorter correlation length in the vicinity of $\boldsymbol{n} \approx \hat{\boldsymbol{z}}$ (depending on the bend constant) and a longer range near $\boldsymbol{n} \approx \hat{\boldsymbol{y}}$ (related to the splay constant). This prediction is difficult to confirm from our observed profiles of $\phi_{\boldsymbol{n}}$, with the range of this variation inconsistent for the director oriented toward either of the coordinate axes.

For the systems with planar-inducing side walls, the director variation along r is also influenced by the end wall. In fact, for the homeotropic-inducing end wall, the profiles of $\phi_{\boldsymbol{n}}$ seem to show no region within the nematic where the system aligns toward the y-axis, whereas the system containing a planer-inducing end wall exhibits more substantial variation between preferring directors along $\hat{\boldsymbol{y}}$ or $\hat{\boldsymbol{z}}$. Hence one could argue that the influence of the homeotropic wall is longer-ranged, but this may be more due to the wall preferring the director $\boldsymbol{n} \approx \hat{\boldsymbol{z}}$ rather than any other properties of the wall, such as its anchoring coefficient or the orientational distribution that it prefers. Another underlying reason for more regions of nematic to be present with director close to $\hat{\boldsymbol{z}}$ could be to minimise the contribution to the free energy from the gradients in the director profile, with more distortions closer to bend than those closer to splay due to the low value of K_3.

Another general observation for the $\boldsymbol{n}_{\mathrm{c}} = \hat{\boldsymbol{y}}, \hat{\boldsymbol{z}}$ geometries is that, where there is local coexistence between nematic and planar phase, directors aligned toward the z-axis seem to be preferred. Two such examples are for the $\boldsymbol{n}_{\mathrm{c}} = \hat{\boldsymbol{y}}$ at densities of $\rho_{\mathrm{bulk}} D^3 = 4.48$ and 4.66, in which the chemical potential has become sufficient for a small nematic region to form that is situated at a considerable distance from the end wall, and $\phi_{\boldsymbol{n}}$ shows $\boldsymbol{n}$ to be close to $\hat{\boldsymbol{z}}$ within these regions, along with even the surrounding planar phase. This observed behavior may be another consequence of the fluid trying to minimise the distortion potential due to director fluctuation, with large gradients being present near the planar-nematic interface. This also suggests that the surface tension of the interface is strongly dependent on the director profile nearby.

Considering these arguements for director variation in the r-direction for the other wedges, it is not surprising that the director profile for $\boldsymbol{n}_{\mathrm{c}} = \hat{\boldsymbol{x}}$ in the nematic

phase rarely strays from $\boldsymbol{n} \approx \hat{\boldsymbol{z}}$ as we inspect different points near each wall, as variation in the plane of the walls will be related to the relatively large K_1 and K_2. This, however, is an effect that has a significant contribution from the strong anchoring present near the hard, flat side walls. The side wall interaction with the fluid is so extreme that we do not see significant variation in the director along the s-direction through the nematic regions, despite the profile depending on the smaller K_3.

The depletion force and potential profiles against wall separation, as discussed in sections 5.3.1-5.3.3, all exhibit behaviours that are not predicted by the first order virial expansion, highlighting the importance of the many-body interactions. It is interesting that the plots for the different state points are not abruptly different once scaled by $1/\rho_{\text{bulk}}$, meaning that the higher order virial coefficients are relatively simple functions of the bulk density. Another worthy point of note is that the depletion interactions did not seem sensitive to the phase changes taking place within the wedge systems. However, as depletion is such a short-ranged interaction, the separation of the walls at which the forces are significant are those that are small enough to contain a fairly consistent phase, i.e. the wall-stabilised nematic for homeotropic anchoring and the planar surface phase for planar anchoring.

For homeotropic anchoring between the walls, the depletion interaction per particle is observed to decrease with bulk density, due to molecules being excluded to a lesser extent on account of their orientations being more sharply peaked around the wall normal. For planar anchoring near the walls, an increase in the density causes more molecules to accumulate near the walls, where part of each molecule can protrude out of the system and is hence less likely to restrict one of its neighbours. This behaviour generally causes the peaks in depletion force and potential at low w profiles to increase and the minima to become more negative, this minimum in potential possibly marking the separation at which the directors at each wall align with one another.

The phase behaviour within the wedge systems did however have a significant effect on the profiles of the adsorption, and in particular the elimination of the isotropic phase from the system (just above the bulk isotropic-nematic transition density) caused sudden drops in the adsorption, as the bulk system undergoes a phase transition into the nematic with the usual accompanying jump in density. It would be interesting to see the higher virial coefficients calculated for the wedge geometry, to see what insite, if any, they could provide into the planar phase and

general phase behaviour,, as well as the effect that the different virials have on the depletion interactions.

The combination of the oriented wetting layers near each wall as the wall separation decreases, which removes the isotropic phase from the central region between the walls that would otherwise be present in the bulk is known as capillary nematisation, and have been estimates for discs using theory [Reich and Schmidt, 2007] and Gibbs ensemble MC simulation [Piñeiro et al., 2007]. These studies estimated the coexistence densities at which, for a given separation, the central region (assumed to be representative of the bulk) transitions from an isotropic to nematic phase, and it is clear how the presence of the walls perturbs the transition. For a fixed density, increasing the wall separation reduces the proportional constitution of the wall-adsorbed layers, allowing the central region to more closely resemble the bulk, and hence for fixed density, there will exist a critical separation that will cause the central region to transition from isotropic to nematic upon decreasing separation. Below this critical separation, no isotropic phase can form, with the capillary nematisation complete.

Such a wall separation can be extracted from our data, by inspecting order parameter profiles $Si = \lambda^+(s, r)$ against s as one decreases r along the wedge, and once the central region is observed to transition into the nematic phase, note the wall separation $w(r)$. For homeotropic anchoring, we observe coexistence for the lowest density state points at separations smaller than $2D$. The isotropic-nematic transition is very weak for platelets, with a coexistence value for S equal to $0.45 - -0.55$. The smallest wall separation that gives the central region values of S within this range will be the critical separation for a nematic at density ρ_{bulk}, specifying the state point present in the wedge. Upon further decrease in the separation, the central region will exhibit coexistence, and the presence of capillary waves will lead to an average order tensor that corresponds to distributions in between those of the isotropic and nematic at phase coexistence, leading to smaller values for S. One must then decide on a tolerence, with S below which being considered to correspond to the isotropic phase, and then this separation will give the critical separation for an isotropic phase with coexistence density ρ_{bulk}.

For the case of planar anchoring, at the lower densities we observe the planar phase wetting the wall along with the isotropic central regions, or capillary planarisation, to wall separations of around $1.5D$, indicating coexistence at $w \approx 1.5D$. For the higher densities, there are interfaces between planar phase and nematic filling

the central region, but the fact that the nematic does not replace the planar phase monotonically with decreasing separation means that there is a very complicated interaction between the wall layers, which is more difficult to describe than for capillary nematisation. It is unclear whether coexistence is achieved between nematic and planar phases.

These values compare to a critical separation of $\approx 4D$ for isotropic-nematic coexistence for cut-spheres ($L/D = 1/10$) exhibiting homeotropic anchoring [Piñeiro et al., 2007], with FMT giving a value of $5.8D$ [Reich and Schmidt, 2007], for state points leading up to and including coexistence. Piñeiro et al. [2007] also studied planar anchoring at the walls, for a similar range of densities, but the phases and layers found were different to those present for our platelets. They found that a planar surface phase was present in only a narrow layer near each wall (with the position vectors lying in a layer $\approx D/2$ in thickness), and these layers acted as rough hard walls for the particles in the central region, inducing a nematic wetting layer close the the planar layer (exhibiting homeotropic anchoring), as well as an isotropic phase away from the walls. The central region was found to undergo an isotropic-nematic transition upon increasing density and reducing wall separation, with a critical separation of $3D$. The surface layer remained in a planar phase.

For homeotropic anchoring, Reich and Schmidt [2007] give a FMT calculation for the adsorption at a single wall, $\sigma_e x$, that is in qualitative agreement with our adsorption for increasing density. The prediction begins at 0, has an initial negative minimum at $\rho_{\text{bulk}} D^3 = 0.2$, then becomes positive and diverges as density is increased to the FMT prediction of the coexistence density. It then becomes finite and decreases monotonically in the nematic phase. Piñeiro et al. [2007] calculated adsorption profiles for a separation of $13.55D$, which showed the similar qualitative behaviour; $\sigma_e x D^2$ increasing from $\approx 0.8 - -1.5$ upon increasing $\rho_{\text{bulk}} D^3$ from $\approx 3.6 - -4.0$ for the isotropic phase; $\sigma_e x D^2$ decreasing roughly monotonically from $\approx 0.3 - -0.1$ upon increasing $\rho_{\text{bulk}} D^3$ from $\approx 3.6 - -4.0$ for the nematic. Our profiles for $\sigma_e x D^2$ exhibit considerable noise, but the values at the larger separations (without being large enough to be measuring the adsorption near the end wall) begin close to zero, then generally increase with increasing density until the isotropic nematic coexistence densities, then generally decrease, giving qualitative agreement, and the actual numerical values for the adsorption are of the same order.

The density and order profiles near a hard wall are consistent with MC simulations and FMT from the work of Reich et al. [2007], with a "correlation hole"

within half a platelet diameter of the wall for the isotropic phase, followed by a "cusp" at a distance of $D/2$, both of which dying away as nematic order, being replaced by a dense wetting layer as nematic order develops. However, separations in excess of $6D$ were utilised, with the density and order profiles for the more dense nematic state points (with $\rho_{\text{bulk}}D^3 > 5.2$) showing signs of not having decayed to the bulk values after one examines a distance $3D$ away from the wall. The adsorption between walls in our wedge will only give accurate values for twice the adsorption of a single wall if the effect of the walls on the platelets becomes neglegible at the centre of the system for our larger separations (up to $3D$ from each side wall). Reich and Schmidt [2007] shows density and order profiles at coexistence for wall separations of $6D - -11D$, and for the isotropic phase the central region for $w = 6D$ shows the same density and order parameter as that for the larger separations. However, for the nematic coexistence density, the central region for $w = 6D$ is significantly different to that of the widest system, with $\big(rho(w = 6D) - rho(w = 11D)\big)D^3 \approx 0.1$ and $\big(S(w = 11D) - S(w = 6D)\big)D^3 \approx 0.25$ near the centre of each system.

There are few results for the depletion forces between macromolecules due to disc-like depletants. Harnau and Dietrich [2002] calculated some properties of hard platelets with homeotropic anchoring near a hard wall for very low density ($\rho_{\text{bulk}}D^3 < 0.2$). The authors extended the theory and utilised the Derjaguin approximation to calculate the depletion potential between two spheres due to platelets, as well as for flat parallel plates, again at very low density [Harnau and Dietrich, 2004]. Their results for parallel plates show an attractive minimum at $w = 0$, showing only slight modification to our first order virial expression. A small positive (repulsive) maximum is present, and grows upon increasing density from $\rho_{\text{bulk}}D^3 = 0.05 - -0.2$.

We have estimated the critical wall separation for isotropic-nematic coexistence of platelets for homeotropic anchoring, which is smaller than a calculation performed by Gibbs ensemble MC simulation of cut-spheres with $L/D = 1/10$ [Piñeiro et al., 2007]. This can likely be attributed to the thickness of the cut-spheres, which becomes particularly important as the orientational distribution becomes highly aligned. It is also possible that capillary wave fluctuations are significantly different between platelets and cut-spheres. This is indeed the case near the walls in each system, and the thin platelets will accordingly have a considerably smaller orientationally averaged excluded volume. The result for critical separation from FMT [Reich and Schmidt, 2007] may be unreliable, with the density and order profiles

providing an improved description over Onsager theory, but the profiles do not agree perfectly with the simulation values. FMT only predicts the coexistence densities and order parameter at the isotropic-nematic roughly, illustrating the limitations of the theory.

The qualitative agreement in adsorption against density is pleasing, with the differences again attributed to the modified phase behaviour of the thicker discs and the limitations of the theory. However, there is evidence as discussed that a maximum separation of $6D$ is not sufficiently wide to yield a central region that exibits bulk behaviour, thus we cannot consider our results at the thick end of the wedge to correspond to two independent walls, and apply that to quantities such as the adsorption. The adsorption between two walls should still give reasonable qualitative behaviour of a single wall, but the values will not be quantitatively representative of such a system. This should not influence the depletion force, however, as the system represents the bulk pressure accurately for our largest separations, and any wider separations would also exert a pressure on the walls equal to the bulk pressure, and as such will not contribute to the depletion potential.

There are numerous directions for future work to follow. It would be intersting to see values for elastic constants for some other molecular models, and see whether this improves on our agreement with experiment. There are disc-like particles that include finite interaction potentials, such as clay platelets (hard platelet possessing a point quadrapole), oblate Gay-Berne particles, spheroplatelets and soft platelets or cut-spheres. One could attempt some constant-$\{NPT\}$ ensemble MC with independently varying box lengths, without a constrained director, to investigate the columnar phase, and the bend elastic constant and the compression moduli could be calculated, as well as properties of the nematic-columnar phase transition. One could attempt to quantify the quality of the elastic description depending on how high-k the distortions are, in order to get reasonable elastic limits.

For the confined systems, the order profiles obtained could be probed to find the critical wall separations for each state point, yielding a plot of system size against density as plotted by Piñeiro et al. [2007] and [Reich and Schmidt, 2007]. The depletion force and potentials could be applied to estimate the depletion forces present in systems of experimental interest, such as mixtures of spheres and hard platelets [Piech and Walz, 2000].

Some simulations of platelets between flat parallel walls could be parformed for some large separations to check the range of the wall-fluid interaction, in an

attempt to observe a region with consistent absorption. There is very little in the literature about the planar phase for discs, and the richness of wall-induced behaviour warrants further study. It is possible that the planar-nematic transition is continuous, and simulaitons of between parallel walls could also probe this behaviour.

For cut-spheres, it would be interesting to see whether the planar surface phase observed by Piñeiro et al. [2007] could transition into a nematic with director somewhere in the plane of the wall at sufficiently high density, as is observed for our platelets. Such a nematic would be in competition with the lower-density homeotropically-aligned nematic, and the system could exhibit a distortion, or the director could vary continuously, depending on the elastic constants and surface anchoring. It would also be interesting to examine cut-spheres with $L/D = 1/5$, which form isotropic, cubatic and columnar phases in bulk [Duncan et al., 2009]. Homeotropic could induce a nematic, and planar anchoring could induce a planar phase and a biaxial phase in the surface layer, with the biaxial phase preferring orientations along two of the three orthoganal axes usually observed in the cubatic phase. This biaxial surface phase could act as a rough, hard wall, inducing similar phase behaviour in the central region as for $L/D = 1/10$, or it could support a cubatic phase. A fourth-rank order tensor would be needed to distinguish between the isotropic and cubatic phases, as well as between the planar and biaxial surface phases.

The simulations in bulk with periodic boundaries were performed in order to obtain the elastic constants, for some molecular models in which there had been considerable interest. The wedge was devised as a system in which a local approximation could be used to obtain profiles of surface quantities as a function of wall separation, as an alternative to performing an infeasibly large number of runs between flat parallel walls, each for a different separation. The phases present in each of these systems, however, were discovered to be interesting in their own right, with categorisation of positionally ordered phases for the bulk, and the analysis of numerous parameters derived from the order tensor to make sense of the orientational order in the wedge, with a surface-induced planar phase present in addition to the nematic and isotropic. The results obtained in the analysis of these phases exhibit enough interesting behaviour to warrant further investigation.

Bibliography

M. Abramowitz and I. A. Stegun, editors. *Handbook of Mathematical Functions*. Dover, New York, 1965.

Michael P. Allen. Molecular dynamics for hard particles. In K. Binder and G. Ciccotti, editors, *Monte Carlo and molecular dynamics of condensed matter systems*, volume 49, chapter 3, pages 89–105. Italian Physical Society, Bologna, 1996. ISBN 88-7794-078-6. Proceedings of the Euroconference on 'Computer simulation in condensed matter physics and chemistry', Como, Italy, July 3-28, 1995.

Michael P. Allen. Introduction to simulations and statistical mechanics. In C. Zannoni and P. Pasini, editors, *Advances in the Computer Simulations of Liquid Crystals*, volume 545 of NATO ASI *Series C*, pages 1–16. Kluwer Academic Publishers, Dordrecht, 2000a. ISBN 0-7923-6099-0. Proceedings of the NATO Advanced Study Institute 'Advances in the Computer Simulations of Liquid Crystals', Erice, Italy, June 11-21, 1998.

Michael P. Allen. Molecular simulation and theory of the isotropic-nematic interface. *J. Chem. Phys.*, 112:5447–5453, 2000b. doi: doi:10.1063/1.481112.

Michael P. Allen and Daan Frenkel. Calculation of liquid crystal Frank constants by computer simulation. *Phys. Rev. A*, 37:1813–1816, 1988. doi: doi:10.1103/PhysRevA.37.1813.

Michael P. Allen and Daan Frenkel. Calculation of liquid crystal Frank constants by computer simulation. *Phys. Rev. A*, 42:3641, 1990. doi: doi:10.1103/PhysRevA.42.3641. Erratum.

Michael P. Allen and Dominic J. Tildesley. *Computer simulation of liquids*. Clarendon Press, Oxford, hardback edition, 1987. ISBN 0-19-855375-7.

Michael P. Allen, Glenn T. Evans, Daan Frenkel, and Bela Mulder. Hard convex body fluids. *Adv. Chem. Phys.*, 86:1–166, 1993.

Michael P. Allen, Mark A. Warren, Mark R. Wilson, Alain Sauron, and William Smith. Molecular dynamics calculation of elastic constants in Gay-Berne nematic liquid crystals. *J. Chem. Phys.*, 105:2850–2858, 1996. doi: doi:10.1063/1.472147.

S. Asakura and F. Oosawa. On interaction between two bodies immersed in a solution of macromolecules. *J. Chem. Phys.*, 22:1255, 1954.

H. Azzouz, J. M. Caillol, D. Levesque, and J. J. Weis. Phase behavior of parallel cut spheres. monte carlo and integral equation results. *J. Chem. Phys.*, 96:4551–4558, 1992.

M. A. Bates. Influence of particle shape on the nematic-isotropic transition of colloidal platelet systems. *J. Chem. Phys.*, 111:1732–1736, 1999.

M. A. Bates and D. Frenkel. Nematic-isotropic transition in polydisperse systems of infinitely thin hard platelets. *J. Chem. Phys.*, 110:6553–6559, 1999.

L. Bellier-Castella, D. Caprion, and J.-P. Ryckaert. Phase diagrams of polydisperse van der Waals fluids. *J. Chem. Phys.*, 121:4874–4883, 2004.

T. Biben, J. P. Hansen, and J. L. Barrat. Density profiles of concentrated colloidal suspensions in sedimentation equilibrium. *J. Chem. Phys.*, 98:7330–7344, 1993.

T. Biben, P. Bladon, and D. Frenkel. Depletion effects in binary hard-sphere fluids. *J. Phys. Cond. Mat.*, 8:10799–10821, 1996.

K. Binder. *Monte Carlo methods in statistical physics*. Springer, Berlin, New York, 1979.

K. Binder, editor. *Monte Carlo Methods in Statistical Physics*, volume 7 of *Topics in Current Physics*. Springer, Berlin, second edition, 1986.

P. Biscari, G. Napoli, and S. Turzi. Bulk and surface biaxiality in nematic liquid crystals. *Int. J. Nonlinear Mech.*, 74:031708/1–7, 2006.

D. Boda and K-.Y. Chan. Structure and pressure of a hard sphere fluid in a wedge-shaped cell or meniscus. *Langmuir*, 15:4311–4313, 1999.

P. G. Bolhuis and D. Frenkel. Tracing the phase boundaries of hard spherocylinders. *J. Chem. Phys.*, 106:666–687, 1997.

V. Botan, F. Pesth, T. Schilling, and M. Oettel. Hard-sphere fluids in annular wedges: Density distributions and depletion potentials. *Phys. Rev. E*, 79: 061402/1–18, 2009.

Philip J. Camp and Michael P. Allen. Hard ellipsoid rod-plate mixtures: Onsager theory and computer simulations. *Physica A*, 229:410–427, 1996. doi: doi:10.1016/0378-4371(96)00050-7.

Philip J. Camp, Carl P. Mason, Michael P. Allen, Anjali A. Khare, and David A. Kofke. The isotropic-nematic transition in uniaxial hard ellipsoid fluids: coexistence data and the approach to the Onsager limit. *J. Chem. Phys.*, 105:2837–2849, 1996. doi: doi:10.1063/1.472146.

S. Chandrasekhar. *Liquid Crystals*. Cambridge University Press, Cambridge, second edition, 1992.

Z. Y. Chen and J. Noolandi. Numerical-solution of the onsager problem for an isotropic-nematic interface. *Phys. Rev. A*, 45:2389–2392, 1992.

D. L. Cheung and M. P. Allen. Structure of a liquid crystalline fluid around a macroparticle: Density functional theory. *Phys. Rev. E*, 74:021701/1–8, 2006. doi: doi:10.1103/PhysRevE.74.021701.

D. L. Cheung and F. Schmid. Monte carlo simulations of liquid crystals near rough walls. *J. Chem. Phys.*, 122(7):074902/1–7, 2005.

D. L. Cheung, L. Anton, M. P. Allen, and A. J. Masters. Computer simulation of liquids and liquid crystals. *Comput. Phys. Commun.*, 179:61–65, 2008. doi: doi:10.1016/j.cpc.2008.01.029.

S. J. Clark, C. J. Adam, D. J. Cleaver, and J. Crain. Conformational energy landscapes of liquid crystal molecules. *Liq. Cryst.*, 22:477–482, 1997.

Douglas J. Cleaver and Michael P. Allen. Computer simulations of the elastic properties of liquid crystals. *Phys. Rev. A*, 43:1918–1931, 1991. doi: doi:10.1103/PhysRevA.43.1918.

Peter J. Collings. *Liquid Crystals: Nature's Delicate Phase of Matter*. Adam Hilger, Bristol, 2nd edition, 2002.

Peter J. Collings and Michael Hird. *Introduction to Liquid Crystals: Chemistry and Physics*. Taylor and Francis, London, 1997.

P. G. de Gennes and J. Prost. *The Physics of Liquid Crystals*. Clarendon Press, Oxford, second, paperback edition, 1995.

P. Deuflhard, J. Hermans, B. Leimkuhler, A. E. Mark, S. Reich, and R. D. Skeel, editors. *Computational Molecular Dynamics: Challenges, Methods, Ideas*, volume 4 of *Lect. Notes Comp. Sci. Eng.* Springer, Berlin, 1998.

H. Dominguez, E. Velasco, and J. A. Alejandre. Stress anisotropy in liquid crystalline phases. *Molec. Phys.*, 100:2739–2744, 2002. doi: doi:10.1080/00268970210132513.

P. D. Duncan, M. Dennison, A. J. Masters, and M. R. Wilson. Theory and computer simulation for the cubatic phase of cut spheres. *Phys. Rev. E*, 79:031702/1–11, 2009.

R. Eppenga and D. Frenkel. Monte Carlo study of the isotropic and nematic phases of infinitely thin hard platelets. *Molec. Phys.*, 52:1303–1334, 1984.

G. T. Evans and E. B. Smith. 2nd virial coefficients for nonspherical molecules - a convex peg in a round hole potential. *Molec. Phys.*, 74:79–84, 1991.

T.E. Faber. A continuum theory of disorder in nematic liquid crystals. v. anisotropy and order-dependence of the frank constants. *Proc. Roy. Soc. Lond. A*, 375:579–597, 1981.

R. P. S. Fartaria and M. B. Sweatman. Density minimum in the isotropic-nematic transition of hard cut-spheres. *Chem. Phys. Lett.*, 478:150–154, 2009.

W. Feller. *An introduction to probability theory and its applications*, volume 1. Wiley, New York, second edition, 1957.

D. Forster. *Hydrodynamic Fluctuations, Broken Symmetry and Correlation Functions*, volume 47 of *Frontiers in Physics*. Benjamin, Reading, 1975.

S. Fraden. Phase transitions in colloidal suspensions of virus particles. In M. Baus, L. F. Rull, and J.-P. Ryckaert, editors, *Observation, prediction and simulation*

of phase transitions in complex fluids, volume 460 of NATO ASI *Series C*, pages 113–164, Dordrecht, 1995. Kluwer Academic Publishers. Proceedings of the NATO Advanced Study Institute on 'Observation, prediction and simulation of phase transitions in complex fluids', Varenna, Italy, July 25–August 5, 1994.

F. C. Frank. On the theory of liquid crystals. *Discuss. Faraday Soc.*, 25:19–28, 1958.

D. Frenkel. Onsager's spherocylinders revisited. *J. Phys. Chem.*, 91:4912–4916, 1987.

D. Frenkel. Erratum structure of hard-core models for liquid crystals. *J. Phys. Chem.*, 92:5314, 1988.

D. Frenkel. Columnar ordering as an excluded-volume effect. *Liq. Cryst.*, 5:929–940, 1989.

D. Frenkel and R. Eppenga. Monte-Carlo study of the isotropic-nematic transition in a fluid of thin hard disks. *Phys. Rev. Lett.*, 49:1089–1092, 1982.

D. Frenkel and B. M. Mulder. The hard ellipsoid-of-revolution fluid I. Monte Carlo simulations. *Molec. Phys.*, 55:1171–1192, 1985.

D. Frenkel and B. Smit. *Understanding molecular simulation : from algorithms to applications*. Academic Press, San Diego, 1996. ISBN 0–12–267370–0.

D. Frenkel, B. M. Mulder, and J. P. McTague. Phase diagram of a system of hard ellipsoids. *Phys. Rev. Lett.*, 52:287–290, 1984.

A. T. Gabriel, T. Meyer, and G. Germano. Molecular graphics of convex body fluids. *J. Chem. Theor. Comput.*, 4:468–476, 2008. URL `http://qmga.sourceforge.net/`.

B. Gotzelmann, R. Evans, and S. Dietrich. Depletion forces in fluids. *Phys. Rev. E*, 57:6785–6800, 1998.

Ian W. Hamley. *Introduction to soft matter : polymers, colloids amphiphiles, and liquid crystals*. Wiley, New York, 2000.

J. M. Hammersley and D. C. Handscomb. *Monte Carlo methods*. Wiley, New York, 1964.

L. Harnau and S. Dietrich. Fluids of platelike particles near a hard wall. *Phys. Rev. E*, 65:021505/1–5, 2002.

L. Harnau and S. Dietrich. Depletion potential in colloidal mixtures of hard spheres and platelets. *Phys. Rev. E*, 69:051501/1–7, 2004.

W. K. Hastings. Monte Carlo sampling methods using Markov chains, and their applications. *Biometrika*, 57:97–109, 1970.

J. R. Henderson. Depletion interactions in colloidal fluids: statistical mechanics of derjaguin's analysis. *Physica A*, 313(3-4):321–335, 2002a.

J. R. Henderson. Solvation of a wedge. *Physica A*, 305:381–386, 2002b.

J. R. Henderson. Interfacial statistical geometry: Fluids adsorbed in wedges and at edges. *J. Chem. Phys.*, 120:1535–1541, 2004.

M. Kroger and P. Ilg. Derivation of Frank-Ericksen elastic coefficients for polydomain nematics from mean-field molecular theory for anisotropic particles. *J. Chem. Phys.*, 127:034903/1–17, 2007.

Mingqing Lu, Michael A. Bevan, and David M. Ford. Interfacial colloidal sedimentation equilibrium. ii. closure-based density functional theory. *J. Chem. Phys.*, 127:164709/1–7, 2007.

T. C. Lubensky. Molecular description of nematic liquid crystals. *Phys. Rev. A*, 2: 2497–2514, 1970.

G. R. Luckhurst and S. Romano. Computer simulation studies of anisotropic systems .26. liquid crystal dimers: A generic model. *J. Chem. Phys.*, 107:2557–2572, 1997.

Y. Mao, M. E. Cates, and H. N. W. Lekkerkerker. Depletion stabilization by semidilute rods. *Phys. Rev. Lett.*, 75:4548–4551, 1995.

Elvira Martín del Río and Enrique de Miguel. Computer simulation study of the free surfaces of a liquid crystal model. *Phys. Rev. E*, 71:051710/1–11, 2005.

Elvira Martín del Río and Enrique de Miguel. Molecular simulation of model liquid crystals in a strong aligning field. *Molec. Phys.*, 104:2919–2927, 2006.

N. Metropolis, A. W. Rosenbluth, M. N. Rosenbluth, A. H. Teller, and E. Teller. Equation of state calculations by fast computing machines. *J. Chem. Phys.*, 21: 1087–1092, 1953.

P. A. O'Brien, Michael P. Allen, D. L. Cheung, M. Dennison, and A. J. Masters. Elastic constants of hard thin platelets by Monte Carlo simulation and virial expansion. *Phys. Rev. E*, 78:051705/1–7, 2008. doi: doi:10.1103/PhysRevE.78.051705.

L. Onsager. The effects of shape on the interaction of colloidal particles. *Ann. N. Y. Acad. Sci.*, 51:627, 1949.

C. Oseen. Theory of liquid crystals. *Trans. Faraday Soc.*, 29:883–899, 1933.

M. A. Osipov and S. Hess. Density functional approach to the theory of interfacial properties of nematic liquid crystals. *J. Chem. Phys.*, 99:4181–4190, 1993.

Patrick Oswald and Pawel Pieranski. Concepts and physical properties illustrated by experiments. In *Smectic and Columnar Liquid Crystals*, chapter C. CRC Press, 2006.

S.M. Oversteegen and H.N.W. Lekkerkerker. Testing the derjaguin approximation for colloidal mixtures of spheres and disks. *Phys. Rev. E*, 68:021404/1–6, 2003.

J. W. Perram, M. S. Wertheim, J. L. Lebowitz, and G. O. Williams. Monte Carlo simulation of hard spheroids. *Chem. Phys. Lett.*, 105:277–280, 1984.

Manuel M. Piñeiro, Amparo Galindo, and Andrew O. Parry. Surface ordering and capillary phenomena of confined hard cut-sphere particles. *Soft Matter*, 3:768–778, 2007. doi: doi:10.1039/b701463e.

M. Piech and J.Y. Walz. Depletion interactions produced by nonadsorbing charged and uncharged spheroids. *J. Coll. Int. Sci.*, 232:86–101, 2000.

P. Pieranski, L. Strzelecki, and B. Pansu. Thin colloidal crystals. *Phys. Rev. Lett.*, 50:900–904, 1983.

R. G. Priest. Theory of the Frank elastic constants of nematic liquid crystals. *Phys. Rev. A*, 7:720–729, 1973.

H. Reich and M. Schmidt. Capillary nematization of hard colloidal platelets confined between two parallel hard walls. *J. Phys. Cond. Mat.*, 19(32):326103/1–12, 2007.

H. Reich and M. Schmidt. Sedimentation equilibrium of colloidal platelets in an aligning magnetic field. *J. Phys. Cond. Mat.*, 132:144509/1–9, 2010.

H. Reich, M. Dijkstra, R. van Roij, and M. Schmidt. Entropic wetting and the free isotropic-nematic interface of hard colloidal platelets. *J. Phys. Chem. B*, 111: 7825–7835, 2007.

R. Roth, Gotzelmann B., and S. Dietrich. Depletion forces near curved surfaces. *Phys. Rev. Lett.*, 83:448–451, 1999.

Samuel. A. Safran. *Statistical Thermodynamics of Surfaces, Interfaces, and Membranes*. Addison Wesley, Reading, Massachusetts, 1994.

A. Saupe. *Z. Naturf. A*, 15:815, 1960.

S. V. Savenko and M. Dijkstra. Sedimentation and multiphase equilibria in suspensions of colloidal hard rods. *Phys. Rev. E*, 70:051401, 2004.

B. Smit. *Computer simulation of phase coexistence: from atoms to surfactants*. PhD thesis, Rijksuniversiteit Utrecht, The Netherlands, 1990.

J. Stelzer, M. A. Bates, L. Longa, and G. R. Luckhurst. Computer simulation studies of anisotropic systems. 27. The direct pair correlation function of the Gay-Berne discotic nematic and estimates of its elastic constants. *J. Chem. Phys.*, 107: 7483–7492, 1997.

J. Swift and B.S. Andereck. Statics and dynamics near the nematic-columnar phase-transition in liquid-crystals. *J. de Physique Lett.*, 43:L437–L440, 1982.

B. Tjipto-Margo and G. T. Evans. The Onsager theory of the isotropic-nematic liquid crystal transition: incorporation of the higher virial coefficients. *J. Chem. Phys.*, 93:4254–4265, 1990.

Broto Tjipto-Margo, Glenn T. Evans, Michael P. Allen, and Daan Frenkel. Elastic constants of hard and soft nematic liquid crystals. *J. Phys. Chem.*, 96:3942–3948, 1992. doi: doi:10.1021/j100189a007.

J. P. Valleau and S. G. Whittington. Monte Carlo in statistical mechanics: choosing between alternative transition matrices. *J. Comput. Phys.*, 24:150–157, 1977.

D. van der Beek, A. V. Petukhov, P. Davidson, J. Ferré, J. P. Jamet, H. H. Wensink, G. J. Vroege, W. Bras, and H. N. W Lekkerkerker. Magnetic-field-induced orientational order in the isotropic phase of hard colloidal platelets. *Phys. Rev. E*, 73: 041402/1–10, 2006a.

D. van der Beek, H. Reich, P. van der Schoot, M. Dijkstra, T. Schilling, R. Vink, M. Schmidt, R. van Roij, and H. N. W Lekkerkerker. Isotropic-nematic interface and wetting in suspensions of colloidal platelets. *Phys. Rev. Lett.*, 97:087801/1–4, 2006b.

D. van der Beek, P. Davidson, H. H. Wensink, G. J. Vroege, and H. N. W Lekkerkerker. Influence of a magnetic field on the nematic phase of hard colloidal platelets. *Phys. Rev. E*, 77:031708/1–8, 2008.

F. M. van der Kooij, D. van der Beek, and H. N. W. Lekkerkerker. Isotropic-Nematic phase separation in suspensions of polydisperse colloidal platelets. *J. Phys. Chem. B*, 105:1696–1700, 2001.

J. A. C. Veerman and D. Frenkel. Relative stability of columnar and crystalline phases in a system of parallel hard spherocylinders. *Phys. Rev. A*, 43:4334–4343, 1991.

J. A. C. Veerman and D. Frenkel. Phase behavior of disk-like hard-core mesogens. *Phys. Rev. A*, 45:5632–5648, 1992.

A. A. Verhoeff, R. H. J. Otten, P. van der Schoot, and H. N. W. Lekkerkerker. Shape and director field deformation of tactoids of plate-like colloids in a magnetic field. *J. Phys. Chem. B*, 113:3704–3708, 2009.

L. Vicari. *Optical Applications of Liquid Crystals*. Institute of Physics, Bristol, 2003.

G. D. Wall and D. J. Cleaver. Computer simulation studies of confined liquid crystal films. *Phys. Rev. E*, 56:4306–4316, 1997.

T. M. Wu, W. J. Ma, and S. F. Tsay. Potential effects on instantaneous normal modes of liquids. *Physica A*, 254:257–271, 1998.

J. Yao, R. A. Greenkorn, and K. C. Chao. Monte Carlo simulation of the grand canonical ensemble. *Molec. Phys.*, 46:587–594, 1982.

C. Zannoni. Distribution functions and order parameters. In G. R. Luckhurst and G. W. Gray, editors, *The Molecular Physics of Liquid Crystals*, chapter 3, pages 51–83. Academic Press, New York, 1979.